Czech Technical University in Prague
Faculty of Civil Engineering
Department of Concrete and Masonry Structures

Influence of Neutron and Gamma Irradiation on Concrete Properties and Structural Performance

by

Yuliia Khmurovska

A dissertation submitted to
the Faculty of Civil Engineering, Czech Technical University in Prague,
in partial fulfilment of the requirements for the degree of Doctor.

Doctoral degree study programme: Civil Engineering
Specialization: Structural and Transportation Engineering

Prague, September 2019

Title of the thesis:

Influence of Neutron and Gamma Irradiation on Concrete Properties and Structural Performance

Ph.D. student:

Mgr. Yuliia Khmurovska
Email: yuliia.khmurovska@fsv.cvut.cz

Supervisor:

prof. Ing. Petr Štemberk, Ph.D., D.Eng.
Email: stemberk@fsv.cvut.cz

Supervisor Specialist:

Ing. Martin Petřík, Ph.D.
Email: martin.petrik@fsv.cvut.cz

Address:

Department of Concrete and Masonry Structures
Faculty of Civil Engineering
Czech Technical University in Prague
Thákurova 7
166 29 Prague 6
Czech Republic

Declaration

Author
Yuliia Khmurovska

Thesis
Influence of Neutron and Gamma Irradiation on Concrete Properties and Structural Performance

I hereby affirm that this doctoral thesis has been written by myself, under the supervision of prof. Ing. Petr Štemberk, Ph.D., D.Eng. and Ing. Martin Petřík, Ph.D.

All sources of information that have been used in the dissertation are acknowledged in the text and listed in the Bibliography, in accordance with the requirements given by the CTU Guideline.

.....
Yuliia Khmurovska
Prague, September 2019

Abstract

This study presents numerical and experimental investigation of the effect of irradiation on concrete properties and structural performance. The neutron irradiation causes radiation-induced volumetric expansion of aggregates which together with cement mortar shrinkage leads to nonuniform strain distribution in concrete and consequently to the local stress concentration. Occurrence of cracks in concrete starts when the stresses reach the strength value. It results in significant reduction of concrete properties (strength, elastic modulus, etc.) which affects the structural performance of concrete. Due to this fact, the coupled damage-creep finite element analysis of the concrete biological shield of VVER 440/213 which combines the newest theoretical and experimental data was performed. The results show that shielding properties of the biological shield may be reduced due to the occurrence of the radial cracks, however, the concrete wall, which is situated right behind the biological shield, will backup the necessary shielding. Additionally, the gamma-ray irradiation causes radiation-induced water radiolysis, which can affect concrete creep, as it, besides others, depends on the amount and the state of water in the cement paste, however, the presented experimental investigation shows an insignificant effect of gamma-ray irradiation on cement mortar creep. Therefore, the creep of gamma-irradiated concrete structures as well as the first estimation of creep of neutron-irradiated structures can be predicted by the existing numerical models. The effect of gamma-ray irradiation on concrete starting from early-age was investigated in order to estimate possibilities of the alternative design in the field of radioactive waste disposal. The results show the reduction of strength after 356 days of irradiation, however, the effect of curing conditions (presence or absence of insulation) has a much larger effect than the gamma-radiation on the measured properties of mortar. Therefore, it can be recommended to provide high humidity and normal ambient temperature during casting and curing for reduction of the potentially negative effects of gamma radiation, such as the irradiation-induced drying. Additionally, examples of application of various approaches (Rigid Body Spring Model, hydration model, microstructure model, image processing) to the related tasks are presented in the Appendix.

Keywords: cement mortar, concrete, creep, damage, early-age, experiment, finite element method, gamma-ray irradiation, neutron irradiation, radiation-induced volumetric expansion, structural performance.

Abstrakt

Tato práce se zabývá numerickým a experimentálním zkoumáním vlivu ozařování na vlastnosti betonu a jeho mechanickou odezvu. Ozařování neutrony způsobuje radiačně indukovanou volumetrickou expanzi kameniva, která spolu se smrštěním cementové malty vede k nerovnoměrnému rozložení napětí v betonové konstrukci a následně k lokální koncentraci napětí. Trhliny v betonu vznikají, když hodnoty napětí dosahují meze pevnosti. Výsledkem je výrazné zhoršení vlastností betonu (pevnost, modul pružnosti atd.), které ovlivňují jeho mechanickou odezvu. Z tohoto důvodu byla provedena numerická analýza (sdružená úloha poškození-dotvarování) betonového biologického stínění reaktoru VVER 440/213 pomocí metody konečných prvků, která kombinuje nejnovější teoretická a experimentální data. Výsledky ukazují, že stínící vlastnosti betonového biologického stínění mohou být sníženy důsledkem vzniku radiálních trhlin, nicméně železobetonová nosná stěna, která se nachází přímo za biologickým stíněním, může dodatečně zajistit potřebné stínění. Ozařování gama zářením rovněž způsobuje radiačně indukovanou radiolýzu vody, která může ovlivnit dotvarování betonové konstrukce, jelikož dotvarování, mimo jiné, závisí na množství a stavu vody v cementové pastě. Předložený experimentální výzkum však ukazuje nevýznamný účinek gama-záření na dotvarování betonu. Existující modely se tedy dají použít pro výpočet dotvarování betonu ozářeného gama zářením a současně jako první odhad pro beton ozářený neutrony. Dále byl zkoumán vliv gama záření na beton raného stáří s cílem prozkoumat možnosti alternativního návrhu betonových prvků, které se používají ve spojitosti s ukládáním radioaktivních odpadů. Výsledky ukazují snížení pevnosti vzorku po 356 dnech ozařovaní, avšak způsob ošetřování (přítomnost nebo nepřítomnost izolace) má mnohem větší účinek než gama-záření na měřené vlastnosti cementové malty. Doporučuje se tedy zajistit vysokou vlhkost a normální okolní teplotu během betonáže a ošetřování těchto betonových prvků pro snížení potenciálně negativních účinků gama-záření, jako je vysychání vyvolané ozářením. Dodatečné příklady tvorby a použití různých kódů a modelů (Rigid Body Spring Model, model hydratace, model mikrostruktury, obrazová analýza) pro související úlohy jsou uvedené v příloze.

Klíčová slova: cementová malta, beton, dotvarování, poškození, rané stáří, experiment, metoda konečných prvků, ozařování gama zářením, ozařování neutrony, radiačně indukovaná objemová expanze, mechanická odezva.

Acknowledgements

First of all, I would like to express my gratitude to my academic supervisor prof. Ing. Petr Štemberk, Ph.D., D.Eng. for valuable comments, consultations, help and support.

I would like to express thanks to my supervisor specialist Ing. Martin Petřík, Ph.D. and my colleagues from the Department of Concrete and Masonry Structures, namely, Ing. Jakub Žak and Ing. Vojtěch Zacharda, for their help in experimental equipment production, as well as colleagues from the Department of Mechanics and the Department of Materials Engineering and Chemistry, namely, Ing. Jiří Němeček and Ing. Magdaléna Doleželová, for their help in experimental investigation.

Colleagues from MTA Centre for Energy Research (Hungary), Fortum Power and Heat Oy (Finland), Institute of Fundamental Technological Research, Polish Academy of Sciences (Poland), The Joint Institute for Power and Nuclear Research - Sosny of the National Academy of Sciences of Belarus (Belarus) are gratefully acknowledged for cooperation.

I am grateful for the the financial support provided by the following organizations:

- Czech Technical University in Prague

  Grant No. SGS15/035/OHK1/1T/11,

  Grant No. SGS16/043/OHK1/1T/11,

  Grant No. SGS17/048/OHK1/1T/11,

  Grant No. SGS18/041/OHK1/1T/11,

  Grant No. SGS19/038/OHK1/1T/11,

- Czech Science Foundation

  Grant No. GA16-20008S,

  Grant No. GA15-11753S,

- Ministry of Education, Youth and Sports of Czech Republic

  Grant No. 8F17002.

Contents

List of Figures

List of Tables

Abbreviations

ACI	**A**merican **C**oncrete **I**nstitute
CBS	**C**oncrete **B**iological **S**hield
CEB	**C**omité **E**uro-international du **B**éton
COD	**C**rystallography **O**pen **D**atabase
C-S-H	**C**alcium **S**ilicate **H**ydrate
EDX	**E**nergy-**D**ispersive **X**-ray spectroscopy
FEM	**F**inite **E**lement **M**ethod
fib	**f**édération **i**nternationale du **b**éton
FIP	**F**édération **I**nternationale de la **P**récontrainte
HD C-S-H	**H**igh **D**ensity **C**alcium **S**ilicate **H**ydrate
LD C-S-H	**L**ow **D**ensity **C**alcium **S**ilicate **H**ydrate
MIP	**M**ercury **I**ntrusion **P**orosimetry
NPP	**N**uclear **P**ower **P**lant
OPT	**OPT**ical microscope
PWR	**P**ressurized **W**ater **R**eactor
RBSM	**R**igid **B**ody **S**pring **M**odel
RIVE	**R**adiation-**I**nduced **V**olumetric **E**xpansion
ROI	**R**egion **O**f **I**nterest of image processing
SEM	**S**canning **E**lectron **M**icroscope
VVER	**V**odo(Water)-**V**odyanoi(Water) **E**nergetic **R**eactor
XRD	**X**-**R**ay **D**iffraction

Symbols

A_c	"μ damage model" constant
A_t	"μ damage model" constant
a_{cr}	aggregate content in concrete mixture using for creep calculation
a_{irr}	material constant for modeling of irradiation-induced properties reduction
B	penetration coefficient
B_0	correction term for early-stage penetration coefficient
B_c	"μ damage model" constant
B_i	porosity distribution parameter
b_{irr}	material constant for modeling of irradiation-induced properties reduction
B_t	"μ damage model" constant
C	parameter describing the growing effect of multi-directional water flow
c	cohesion
c_{cr}	cement content in concrete mixture using for creep calculation
D	total isotropic damage
D_{irr}	damage due to effect of irradiation
D^{mech}	mechanical damage
D_{temp}	damage due to effect of temperature
$D(t)$	indentation creep compliance at time t
d	depth under the irradiated surface in cm
d_c	distance from center in m
$d_{concrete}$	thickness of concrete sample
d_{dry}	thickness of dry material in sample

$d(t)$	depth of water penetration at time t
d_{water}	thickness of water
d_{wet}	thickness of wet material in sample
E	elastic modulus affected by irradiation, temperature and mechanical damage
E^0	initial elastic modulus
$E^{\wedge}$	elastic modulus after irradiation at operation temperature
E_{NI}	elastic modulus obtained using nanoindentation technique
E^{irr}	elastic modulus affected by irradiation only
E^{temp}	elastic modulus affected by temperature only
F	sample surface area exposed to water
f_c^0	initial compressive strength
$f_c^{\wedge}$	compressive strength after irradiation at operation temperature
f_c^{irr}	compressive strength affected by irradiation only
f_c^{temp}	compressive strength affected by temperature only
f_t^0	initial tensile strength
$f_t^{\wedge}$	tensile strength after irradiation at operation temperature
f_t^{irr}	tensile strength affected by irradiation only
f_t^{temp}	tensile strength affected by temperature only
$f(d)$	neutron flux at given depth under irradiated surface
$f(d, d_c)$	neutron flux at given depth under irradiated surface and given distance from center
f_{surf}	neutron flux on irradiated surface
G	shear modulus
g_f	tensile fracture energy
H_{NI}	hardness obtained using nanoindentation technique
$h(t)$	indentation depth at time t
h	distance between nuclei of Voronoi diagrams
$I'(i,j)$	intensity of normalized image in i-j location
$I_0(i,j)$	intensity of incident beam in i-j location
$I_{DarkCurrent}(i,j)$	intensity of dark current image in i-j location

$I_{dry}(i,j)$	intensity of beam transmitted through dry sample in i-j location
$I_{OpenBeam}(i,j)$	intensity of open beam image in i-j location
$I_{Raw}(i,j)$	intensity of raw images in i-j location
$I_{wet}(i,j)$	intensity of beam transmitted through wet sample in i-j location
J_{cr}	creep compliance
K	shear softening coefficient
k	material parameter for RIVE modeling
k_1	flux reduction factors due to attenuation
k_2	flux reduction factors due to source geometry
$NORM$	factor to bring resulting value into valid range of image-processing tools
P_0	indentation load
p_i	mass ratio of chemical component i of cement
$\overline{Q}_i$	accumulated heat generation of chemical component i
$\overline{Q}_{i,\infty}$	maximum theoretical specific heat of component i
R_E^{irr}	elastic modulus reduction factor due to effect of irradiation
$R_{f_c}^{irr}$	compressive strength reduction factor due to effect of irradiation
$R_{f_t}^{irr}$	tensile strength reduction factor due to effect of irradiation
R_E^{mech}	elastic modulus reduction factor due to mechanical damage
R_E^{temp}	elastic modulus reduction factor due to effect of temperature
$R_{f_c}^{temp}$	compressive strength reduction factor due to effect of temperature
$R_{f_t}^{temp}$	tensile strength reduction factor due to effect of temperature
r	pore radius
S	early-stage sorptivity coefficient
S_0	correction term for early-stage sorptivity coefficient
S_0'	correction term for secondary sorptivity coefficient
S_2	secondary sorptivity coefficient
T	temperature
T^0	initial temperature
t	concrete current age
t	time (in Equation 4.2 and Appendix)

t'	concrete age at loading
V_{aggr}	volume fraction of aggregate in concrete mixture
V_{cem}	volume fraction of cement in concrete mixture
V_{cl}	volume of anhydrous clinker
V_s	volume of hydrated products
V_i	normalized pore volume
W_p	weight of powder materials per unit paste volume
$W(t)$	volume of absorbed water at time t
w_{cr}	water content in concrete mixture using for creep calculation
α	angle between surface and edge of indentation tip
α_0	coefficient of thermal expansion of α-quartz after phase transformation
α_1	material parameter for coefficient of thermal expansion modeling
α_{aggr}	coefficient of thermal expansion of α-quartz aggregates
α_{cem}	coefficient of thermal expansion of cement paste
$\alpha_{concrete}$	coefficient of thermal expansion of concrete
α_{cr}	parameter for creep estimation
α_{hyd}	averaged degree of hydration
β	material parameter for creep and damage coupling
β_{cr}	shear deterioration coefficient
γ_f	shear strain which corresponds to shear strength
δ	material parameter for RIVE modeling
ΔT	temperature change
ε_C	material parameter for coefficient of thermal expansion modeling
ε_{cr}	creep strain
ε_{irr}	linear strain due to RIVE
ε_L	material parameter for coefficient of thermal expansion modeling
ε_{max}	maximum RIVE strain
ε^{RIVE}	RIVE strain
ε_{temp}	thermal strain
ε_{tot}	total strain
ν	Poisson's ratio

ρ_p	density of powder materials
ρ_{water}	water content in g per cm^3 of concrete
Σ_{dry}	effective linear attenuation coefficients of dry sample
Σ_R	Portland concrete neutron removal cross section
Σ_{water}	effective linear attenuation coefficients of water
Σ_{wet}	effective linear attenuation coefficients of wet sample
σ	stress
σ_t	maximum tensile stress
σ_b	compressive limit stress for RBSM
τ_f	shear strength
Φ	neutron fluence
ϕ_c	capillary porosity
ϕ_g	gel porosity
ϕ_l	interlayer porosity
φ	angle of internal friction
ψ	water capacity

Chapter 1

Introduction

This chapter presents a general problem description and motivation as well as information about the structure of this doctoral thesis. The main goals of the doctoral thesis are also formulated in this chapter.

1.1 Problem description

The presented doctoral thesis deals with following problems:

- ***Modeling of concrete structure under exposure to irradiation environment***

  According to The World Nuclear Industry Status Report (Schneider et al., 2017), the unit-weighted average age of the world operating nuclear reactors is rising continuously, and by mid-2017 stood at 29.3 years, up from 29.0 a year ago and 28.8 two years ago (Schneider et al., 2016). Despite the fact that the initial design operating period of nuclear power plants (NPPs) is 30 to 40 years, over a half of the total 234 units have operated for 31 years and more, including 64 that have run for 41 years and more. This means that the NPPs which are nearing the end of their licensed operating period need to be either shut down or their operation time licenses have to be prolonged. It should be noted that the license renewal is preferable before the reactor shutdown because of the long NPP decommissioning process which is also associated with significant costs. For example, 84 of the 99 operating U.S. units had received a license extension

with a further nine applications under review as of 1 July 2017.

There are two significant factors which lead to development of this study. Firstly, there is no precedent of such a long-term radiation exposure to concrete which would be well documented and with the neutron flux similar to that in operating NPPs. Secondly, there is no possibility to investigate the real-scale structural elements under long-term irradiation conditions, mainly due to safety restrictions and cost. Therefore, the only possible way to predict the behavior of CBS is to use the available data from accelerated tests on small-scale concrete specimens obtained in test reactors and to extrapolate these data to the real scale by numerical simulation.

- ***Investigation of the effect of gamma-ray irradiation on cement mortar creep***

  The creep of concrete is one of the basic and fundamental concrete properties. Creep not only redistributes stresses in the structure and consequently alters the damage pattern (Bažant and Gettu, 1992) and delays the damage onset (Giorla et al., 2017) but it may also cause a significant displacement and deviations from the design position of the structure (Rusch, 1960). These statements are extremely important for the Pressurized Water Reactors (PWR) since the low creep level may restrict stress relaxation and may result in damage of CBS, while a higher creep level may cause the biological shield movement and thus may lead to deviation in the pressure vessel position, which may damage the cooling system or complicate the normal NPP operation in any other way. Therefore, experimental investigation of the effect of gamma-ray irradiation on concrete creep has to be performed.

- ***Investigation of the effect of early-age gamma-ray irradiation on cement mortar***

  The new design concept in radioactive waste deposition like Belgium's supercontainer, where concrete is in contact with radioactive waste immediately after casting (Craeye et al., 2009, 2011), demands a thorough study of the effect of gamma-ray irradiation on cement mortar right after it is mixed and cast. The

understanding of this process can build the platform for the alternative design possibilities in the field of radioactive waste disposal. Therefore, experimental investigation of the effect of early-age gamma-ray irradiation on concrete has to be performed.

1.2 Goals of doctoral thesis

The goals of this thesis are as follows:

- to investigate the mechanism of radiation-induced deterioration of concrete based on the literature review;
- to develop a numerical approach which takes into account irradiation-induced deterioration of concrete based on the relevant experimental and measured data;
- to analyze a real NPP structural element;
- to perform experimental investigation of the effect of gamma-ray irradiation on cement mortar creep;
- to perform experimental investigation of the effect of early-age gamma-ray irradiation on cement mortar.

1.3 Structure of doctoral thesis

This thesis is organized into six chapters as follows:

Chapter 1: *Introduction*

provides the general overview of investigated problems and describes the goals and the structure of the doctoral thesis.

Chapter 2: *General state of the art*

introduces the necessary theoretical background and describes the mechanisms behind radiation-induced deterioration of concrete based on a review of relevant research.

Chapter 3: *Numerical analysis of VVER-440/213 concrete biological shield*

describes a numerical approach to non-linear FEM concrete biological shield (CBS) modeling which takes into account the effects of irradiation, creep and temperature on CBS structural response. The results are also provided and discussed in detail.

Chapter 4: *Experimental investigation of effect of gamma-ray irradiation on cement mortar creep*

presents detailed description of the experimental investigation of the effect of long-term (369 days) gamma-ray irradiation on cement mortar creep at two different levels, i.e. the mesoscale level (direct measurements of sample strain) and the nanoscale level (nanoindentation).

Chapter 5: *Experimental investigation of effect of early-age gamma-ray irradiation on cement mortar*

describes in detail the experimental investigation of effect of long-term (188 days and 356 days) early-age gamma-ray irradiation on cement mortar.

Chapter 6: *Conclusions*

summarizes the main contributions of the doctoral thesis and suggests possible topics for further research.

Appendix *Application of MATLAB codes*

shows the examples of application of various codes and models (Rigid Body Spring Model, hydration model, microstructure model, image processing) to the related tasks.

Chapter 2

State of the art

This chapter describes the mechanism of radiation-induced deterioration of concrete and its components based on the literature review. The deterioration mechanism in different levels starting from the interaction between neutron and nucleus through the mineral metamictization and cement paste shrinkage up to the reduction of mechanical properties of concrete is explained in detail. All basic dependencies and trends of volumetric change of minerals, aggregates, cement paste and finally concrete are also described. Finally, the reduction of concrete mechanical properties is in correlation with its volumetric expansion. The radiation-induced volumetric expansion (RIVE) of concrete is affected by irradiation conditions (neutron fluence, neutron spectrum and temperature) and concrete composition (amount, proportion, type and structure of the minerals in the aggregate composition and amount, composition, age and structure of the cement paste).

2.1 Deterioration mechanism

2.1.1 Neutron irradiation

Interaction of neutrons with matters occurs through inelastic scattering, elastic scattering and absorption depending on the neutron energy. The fast neutrons are scattered inelastically. When a high-energy fast neutron collides with a nucleus, it is absorbed and the compound nucleus is created. The compound nucleus decays into a lower-energy neutron and an excited nucleus. The nucleus gives up excitation

energy by emitting one or more gamma rays (so-called secondary gamma-ray). The traveling direction of both, the neutron and the nucleus, are changed after collision. This process may repeat until the fast neutron becomes an intermediate neutron. It should be noted that inelastic scattering is typical for neutron collision with heavier atomic nuclei. The intermediate neutrons are scattered elastically. After intermediate neutron collision with the nucleus, its energy is transferred to the recoiling nucleus and both, the neutron and the nucleus, change their traveling direction, but the intermediate neutron does not have enough energy to cause the nucleus excitation and the subsequent gamma-ray release. The elastic collisions may repeat until the intermediate neutron becomes a thermal neutron. When the thermal neutron collides with the nucleus, its energy is too low to cause further scattering and its energy is absorbed in the collision.

Concrete is a composite material which consists of cement paste, aggregates (fine and coarse) and water, while in turn the aggregates are composed of minerals. The high energy neutrons cause defects in the lattice structure of the minerals by the elastic scattering and the inelastic scattering. According to Denisov et al. (2012), the threshold energy of the neutrons to cause the defects in the lattice structure of the minerals is equal to 10 keV. A vacancy at the original site and an interstitial defect at the new location (Frenkel pair) are created due to the neutron ballistic effect. These point defects and their cascades can be accumulated and result in mineral metamictization (amorphization in some literature) which leads to the significant change in the properties of minerals (volume, density, etc.) and consequently changes the properties of concrete (volume, strength, elastic modulus, etc.). It is believed that the effect of the neutron irradiation on cement paste is much smaller in comparison with the effect on minerals and aggregates and rather results in cement paste shrinkage, because the Calcium Silicate Hydrate (C-S-H) gel, the main component of cement paste, is amorphous and has very porous structure. The pore volume represents about 20 % of C-S-H volume (Kontani et al., 2013), therefore, the probability of collision is much smaller and the threshold energy of neutrons to cause the damage of cement paste is much higher and equal to 0.8 MeV. However, Denisov et al. (2012) discusses Portlandite metamictization due to the neutron irradiation and its subsequent reaction with

the carbon dioxide present in air. This leads to $CaCO_3$ formation (carbonation reaction), which can affect the properties of cement paste. It should be noted that the high-energy neutrons may also excite water and thus provoke the radiation-induced water decomposition (radiolysis) with the consequent drying due to the gas release, which may mainly vary the properties of cement paste, while aggregates have a much lower amount of water in their composition.

According to Denisov et al. (2012), contraction of the lattice structure of minerals due to creation of vacancies is lower than the lattice structure expansion due to the interstitial defects, see Figure 2.1, therefore, the mineral metamictization due to the accumulation of the defects causes the RIVE. An uneven expansion of different minerals in the aggregate composition causes concentration of stresses. When the stresses exceed the strength of the materials, the cracks start to develop. Moreover, cement paste may shrink under the exposure to neutron irradiation due to the radiation-induced water evaporation which in combination with the aggregate expansion causes development of cracks in cement paste. The propagation of cracks in aggregates and cement paste leads to the reduction of the elastic modulus, the compressive and the tensile strength of concrete. Thus, the volume change of aggregates and cement paste can be considered as a primary factor of the radiation-induced damage of concrete.

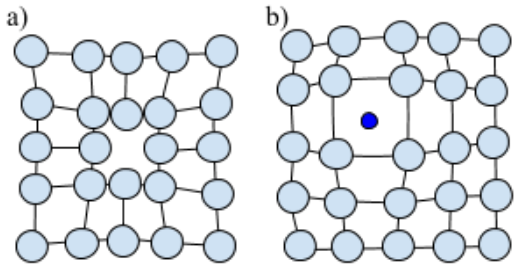

Figure 2.1: Lattice defects: a) vacancy, b) interstitial.

The effect of neutron irradiation on creep of concrete is not yet understood. In the study presented by Gray (1971), the influence of neutron irradiation on concrete creep was studied and it appeared to be insignificant, nevertheless, the final conclusion is difficult to draw from this experiment. According to Denisov et al. (2012), the creep of the irradiated samples is approximately seven times higher in comparison

with the control samples, however an increase in the creep is explained by the high temperature (240 °C) which accompanied irradiation in the research reactor. The research presented by Dubrovskii et al. (2010) also concludes that the increase in creep is caused by the elevated temperature only.

2.1.2 Gamma-ray irradiation

The gamma-rays cause the electron excitation and subsequently remove electrons from the atoms by the electron-positron pair production, the Compton scattering and the photoelectric effect that may also cause the water radiolysis, which leads to drying due to the gas release (Bouniol and Aspart, 1998). The radiolysis is accompanied by the free radicals and hydrogen peroxide formation(Le Caër, 2011; Bouniol and Bjergbakke, 2008), which may react with cement hydration products and may alter the cement paste properties and even provoke the carbonation reaction (Vodák et al., 2011; Maruyama et al., 2017, 2018). Finally, the gamma-rays are absorbed by the material as the thermal atom vibration, which causes the so-called gamma heating which can also affect cement paste properties. It should be noted that the neutron radiation is always accompanied by the gamma-rays and thus also with an increase in temperature.

Both the neutrons and the gamma-rays may affect water, however, the effect of the neutron irradiation and the gamma irradiation on water can differ due to the difference in the energy transmitted to water during the interaction, (Kontani et al., 2013).

It is believed that the gamma-rays affect only slightly the aggregate properties and that majority of the changes appear in the cement paste. According to Hilsdorf et al. (1978), a significant reduction of the cement paste properties appears beyond the threshold of 200 MGy of the absorbed gamma-ray dose. Also, in Lowinska-Kluge and Piszora (2008) the hydrates decomposition within the absorbed gamma-ray dose range of 130 to 836 MGy can be found. On the other hand, the reduction in compressive strength at much lower absorbed gamma-ray dose (15 % reduction with the absorbed dose of 22 MGy and 10 % reduction with the absorbed dose of 0.3-0.5 MGy, respectively) was observed by Soo and Milian (2001) and Vodák et al.

(2005). However, the mechanism of this strength reduction is still unclear. According to Maruyama et al. (2017), the strength of cement paste reduces due to its drying and heating under the gamma rays while the radiation-induced vaterite-carbonation increases the strength of cement paste, (Maruyama et al., 2018).

According to the only one available research of the effect of gamma-ray irradiation on the creep of the cement paste presented in McDowall (1971), the gamma-ray reduces the creep and increases the autogenous shrinkage. However, the mechanism of this process is also not fully understood and requires additional experimental investigation.

All the above mentioned studies investigate the effect of gamma-ray irradiation on already hardened cement-based samples. The early-age mortar has a large amount of free water which can be subjected to radiolysis and affect the cement hydration process therefore the final properties of the mortar may be changed. The very limited amount of publications regarding the effect of gamma-ray irradiation on the early-age cement-based materials are available and this effect is not well understood yet. According to the current research (Ochbelagh et al., 2010, 2011; Burnham et al., 2016, 2017), the early-age mortar when exposed to the low-level dose rate of gamma-ray irradiation during 7 days (irradiation starts in the range of 5-hours age to 24-hours age) ensures an increase in strength (in the range from 22 % to 88 %) and shielding properties of the mortar. After the irradiation of early-age mortar for 28 days the strength remains unchanged (Burnham et al., 2017). However, no microstructure investigation (except scanning electron microscopy) were presented in all the mentioned studies.

On the other hand, the investigation of three different self-compacting mortars under exposure to different (low, medium and high) gamma-ray irradiation dose rates, which is available in Craeye et al. (2015), shows the reduction of compressive strength of more than 5 % as well as the reduction of mortar density (in the range from 0.2 to 2.9 %) and an increase in porosity (irradiation starts at the mortar age of 0.5 hour). It should be noted that a relatively high water-to-cement ratio, from 0.48 to 0.75, and a large amount superplasticizer is characteristic for self-compacting mortar in order to provide sufficient mixture workability.

According to Mobasher et al. (2015) research, where the blast furnace slag and

Portland cement matrix under the exposure to a high gamma radiation dose rate was investigated (irradiation starts at the age of 8 days), the compressive strength of samples increased by an average of 19 % despite the occurrence of microcracks due to the decrease in physically bounded water content. The heating of the samples up to 50 °C shows 7 % increase in compressive strength only. No effect of irradiation on crystalline phases is observed and the carbonation reaction is not detected.

2.2 Main trends in radiation-induced volumetric changes

2.2.1 Minerals

The RIVE of the minerals, first of all, depends on the neutron fluence which is the accumulated number of the neutrons travelling through the unit area and also can be defined as the neutron flux integrated over the time period. The threshold fluence to cause the RIVE of minerals is in the order of 10^{19} n/cm^2. However, the neutron fluence by itself can not characterize the RIVE, since the same amount of the neutrons can cause different damage, because the high-energy neutrons can create more than one Frenkel pairs and cause the cascade of the lattice defects. Therefore, the RIVE depends not only on neutron fluence but also on the energy spectrum of neutrons. With the same fluence the hard neutron spectrum (the spectrum with a higher amount of high energy neutrons) causes more lattice defects and consequently higher RIVE then the soft neutron spectrum (the spectrum with a lower amount of high energy neutrons), see Figure 2.2. The number of point lattice defects can be predicted by, for example, Kinchin-Pease model, (Kinchin and Pease, 1955).

The number of lattice defects also depends on the temperature during irradiation. With higher temperature, the probability of the lattice defects recombination is higher, so some lattice defects can be annihilated. Therefore, the higher temperature results in lower RIVE, see Figure 2.3. However, the normal operation temperature of NPPs is about 60 °C, which corresponds to relatively high RIVE. Silicate minerals are the most sensitive to elevated temperature, see Figure 2.3 b), while the effect of elevated temperature on RIVE of carbonates is insignificant in the temperature range of 30-270 °C, (Denisov et al., 2012).

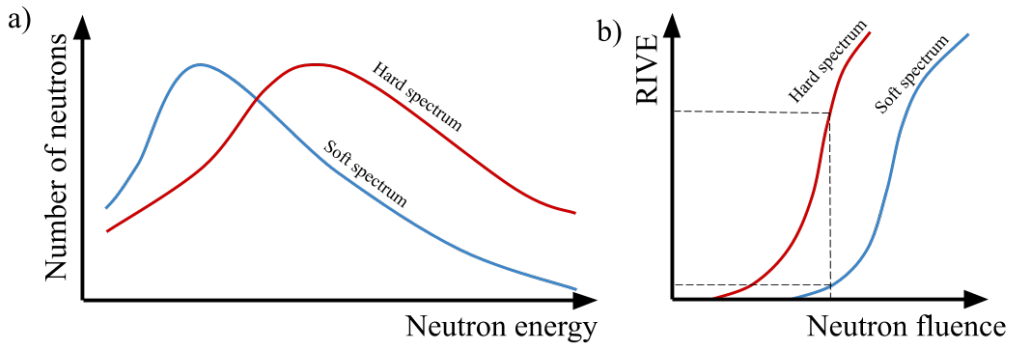

Figure 2.2: Comparison of RIVE due to hard neutron spectrum and soft neutron spectrum: a) neutron irradiation spectrum, b) RIVE, (Dubrovskii et al., 2010).

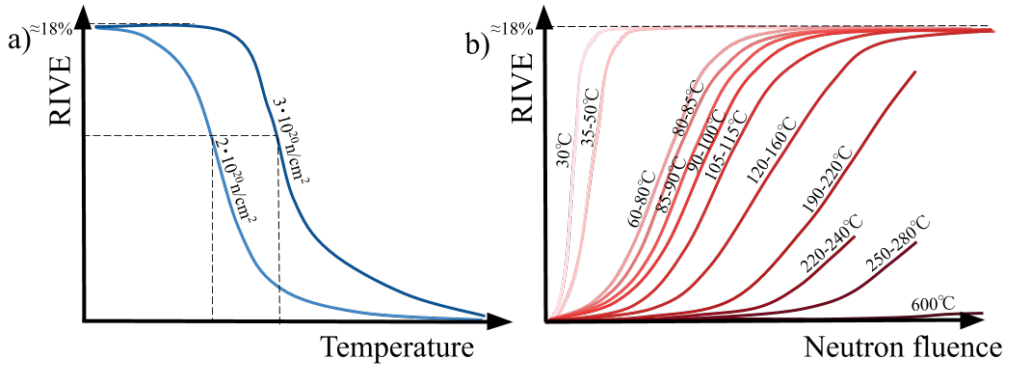

Figure 2.3: Influence of temperature on RIVE of α-quartz: a) RIVE versus temperature at different fluence (Denisov et al., 2012), b) RIVE versus neutron fluence at different temperature (Dubrovskii et al., 2010).

The RIVE also depends on the type and the structure of minerals. The highest RIVE is typical for the framework silicates (Tectosilicates) with the highest amount of silica and is equal to 17.9 % for quartz, (Denisov et al., 2012). The RIVE reduces with the decrease in the silica content up to 8 % for alkali-feldspar, (Denisov et al., 2012). Also the RIVE reduces with the decrease in the silicate degree of polymerization from the framework silicates to the sheet silicates (Phylosilicates), the RIVE is up to 5 % for mica, (Denisov et al., 2012), and further to the chain silicates (Inosilicates), the RIVE of double-chain silicates is about 2.8 % and the RIVE of single-chain silicates is about 1.5 %, (Denisov et al., 2012), and finally for the island silicates (Nesosilicates), the RIVE of olivine is about 0.9 %, (Denisov et al., 2012), see Figure 2.4.

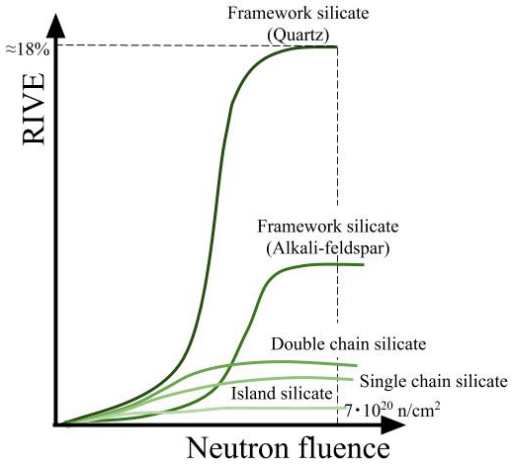

Figure 2.4: Influence of mineral structure on RIVE of silicates, (Dubrovskii et al., 2010).

The RIVE of the carbonates is typically much lower in comparison with the silicates and varies in the range of 0.5-4 %. The higher RIVE occurs in carbonates with complex composition and lower structure symmetry, (Denisov et al., 2012).

Moreover, according to Denisov et al. (2012), the RIVE depends on the heat of fusion of minerals, which characterizes the energy required by the mineral for phase transformation, while according to Le Pape et al. (2018), the RIVE depends on the bond-dissociation energy of minerals, which characterizes the energy needed for chemical bond dissociation. Basically, these two parameters describe how strong and stable a lattice structure is, however, they affect the RIVE in the opposite way, i.e. with lower heat of fusion and/or with higher bond-dissociation energy, the RIVE becomes higher.

From the above, the following trends can be highlighted:
The RIVE of mineral is higher with

- higher neutron fluence,
- harder neutron spectrum,
- lower temperature,
- higher silicate degree of polymerization (for silicates),

- higher silica content (for silicates),
- more complex composition (for carbonates),
- lower structural symmetry (for carbonates),
- lower heat of fusion and/or higher bond-dissociation energy.

2.2.2 Aggregates

The RIVE of aggregates is defined by the minerals presented in their composition and depends on the amount of minerals with the highest RIVE, see Figure 2.5. The complex stress state due to the different level of RIVE of the minerals results in development of cracks, therefore, the RIVE of aggregates is higher (up to 20-23 %) than the RIVE of the minerals due to the additional volume of cracks. Also, the RIVE of coarse-grain aggregates is usually higher that the RIVE of fine-grain aggregates, (Dubrovskii et al., 2010; Denisov et al., 2012).

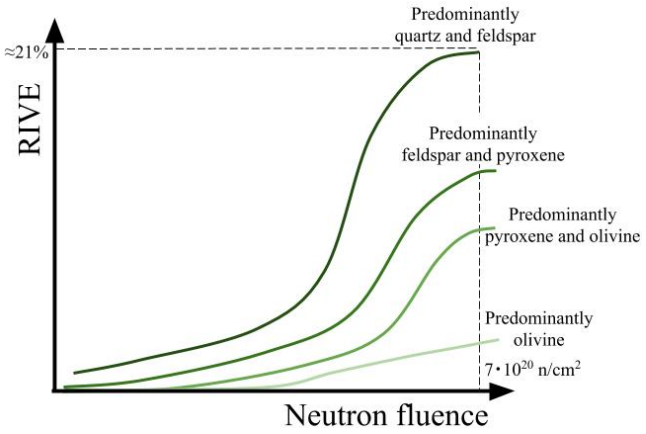

Figure 2.5: Influence of mineral composition on aggregate RIVE, (Dubrovskii et al., 2010).

The amount of the amorphous material also affects the RIVE of the aggregates since the amorphous materials, such as glass, contract under exposure to irradiation, (Dubrovskii et al., 2010; Denisov et al., 2012), and can reduce the total aggregate RIVE.

Therefore, the RIVE of aggregates depends on

- mineral composition of the aggregates,
- RIVE of the minerals,
- grain size of the aggregates,
- amount of amorphous material.

The reduction of the aggregates mechanical properties (strength, elastic modulus, etc.) correlates with their RIVE and the volume of cracks.

2.2.3 Cement paste

The Portland cement is the most commonly used type of cement and, therefore, the available experimental data are predominantly focused on the Portland cement. The amorphous C-S-H gel is the main component of cement paste, thus, instead of expansion which is typical for crystalline materials, contraction of the cement paste (up to 9.5 % by volume at 400 °C, (Denisov et al., 2012)) under irradiation is observed. The reason of the cement paste contraction is in the hydrate decomposition and the water radiolysis which leads to the loss of water and is accompanied by release of a significant amount of gas. The correlation between the cement paste shrinkage and the loss of water can be observed. According to Denisov et al. (2012), the cement paste can lose up to 64 % of water (including chemically bound and adsorbed water).

Similarly to the minerals, the effect of radiation on the cement paste increases with the increase in the neutron fluence and with the harder neutron spectrum. However, temperature has an opposite effect than in the case of minerals, i.e. the radiation-induced shrinkage of the cement paste is higher with higher temperature due to the water evaporation, see Figure 2.6 a).

The radiation-induced shrinkage of the cement paste reduces with an increase in the water-to-cement ratio due to the increase in carbonation. The carbonates fill in the pores and restrict the cement paste contraction. However, the early-age cement paste shrinks more than the hardened cement paste under exposure to neutron irradiation and its shrinkage increases with the increase in the water-to-cement ratio, (Denisov et al., 2012).

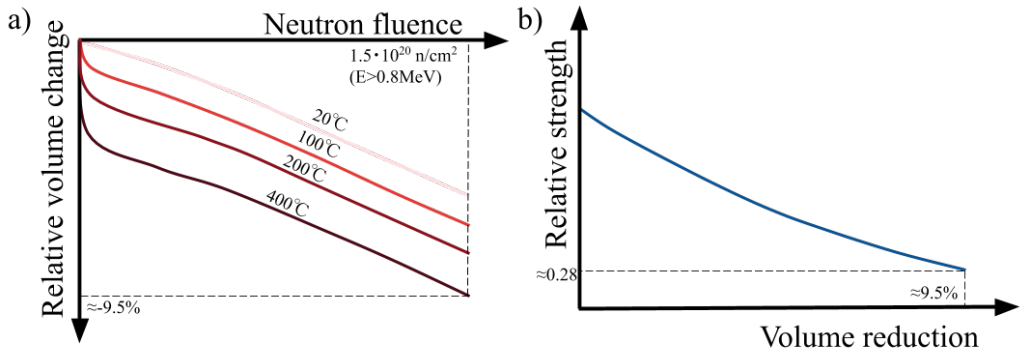

Figure 2.6: Radiation-induced changes in hardened cement paste: a) volume change, b) strength change, (Denisov et al., 2012).

Also, it is believed that admixture and additives can vary the cement paste response to the neutron irradiation.

From the above, we can conclude that the radiation-induced shrinkage of cement paste depends on

- neutron fluence,
- neutron spectrum,
- temperature,
- water-to-cement ratio,
- age of cement paste,
- presence of admixtures or additives.

According to Dubrovskii et al. (2010), the strength of the cement paste reduces up to 40 % and according to Denisov et al. (2012) the strength reduction can reach 72 %, see Figure 2.6 b). The strength of the early-age cement paste may increase up to 45 % at the beginning of irradiation and then reduces up to 37 %.

2.2.4 Concrete

The volumetric change of concrete depends on the volumetric change of cement paste and aggregates and its proportion in the concrete. The parameters which the volumetric change of concrete depends on can be divided into two groups:

- irradiation conditions (neutron fluence, neutron spectrum and temperature),
- concrete composition (amount, proportion, type and structure of minerals in the aggregates and amount, composition, age and structure of the cement paste).

The volumetric expansion of concrete due to the neutron irradiation leads to the reduction of strength and elastic modulus due to the crack formation and the aggregate and the cement paste strength reduction, see Figure 2.7. The volumetric expansion of concrete is in correlation with the reduction of its mechanical properties.

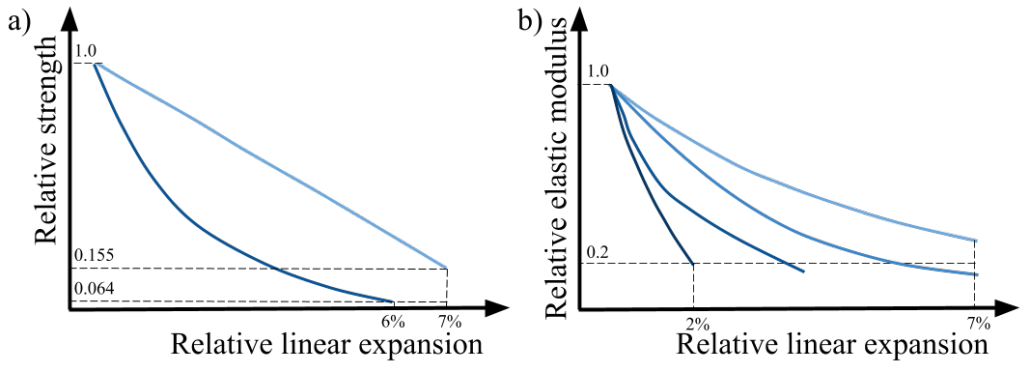

Figure 2.7: Reduction of mechanical properties of concrete with different composition: a) strength, b) elastic modulus, (Denisov et al., 2012).

2.3 Conclusions

The mechanism of the radiation-induced deterioration of concrete and its components is described in detail based on the literature review.

All the basic dependencies and trends of the volumetric change of minerals, aggregates, cement paste and concrete are also described.

The RIVE of minerals is affected by neutron fluence, neutron spectrum, temperature, silicate degree of polymerization (for silicates), silica content (for silicates), complexity of composition (for carbonates), structural symmetry (for carbonates) and heat of fusion and/or bond-dissociation energy.

The RIVE of aggregates is affected by mineral composition of the aggregates, the RIVE of the minerals, grain size of the aggregates and the amount of amorphous material.

The radiation-induced shrinkage of the cement paste is affected by neutron fluence, neutron spectrum, temperature, water-to-cement ratio, age of the cement paste and presence of admixtures and additives.

Finally, the RIVE of concrete is affected by irradiation conditions (neutron fluence, neutron spectrum and temperature) and concrete composition (amount, proportion, type and structure of minerals in the aggregate composition and amount, composition, age and structure of the cement paste).

The reduction of the concrete mechanical properties is in correlation with its volumetric expansion.

Neutron irradiation plays a major role in radiation-induced deterioration of concrete, however gamma-ray irradiation may also alter concrete properties.

Chapter 3

Numerical analysis of VVER-440/213 concrete biological shield

The numerical approach of the coupled damage-creep modeling of CBS, which combines the current and the past knowledge regarding the effects of irradiation and temperature on concrete with the real measured and calculated neutron fluence and temperature distribution for VVER-440/213 reactors, is described in detail in this chapter. The proposed approach takes into account the real structural geometry as well as the real neutron fluence and temperature distribution and the latest knowledge about the effect of irradiation and temperature on concrete strength and stiffness. The RIVE and the thermal expansion of concrete are modeled. According to the results of the numerical simulation, the analyzed structure reaches critical damage within the time interval from 10.00 to 35.25 years of normal operation. The damage of the concrete biological shield (CBS) of the VVER reactor will not affect the load-bearing function of the containment building since the biological shield is self-bearing. The shielding properties of the CBS may be reduced due to the occurrence of the radial cracks, however, the concrete wall, which is situated right behind the biological shield, will provide the additional shielding.

3.1 Motivation

This chapter focuses on the numerical analysis of the structural response of a real NPP biological shield which takes into account the real irradiation and temperature conditions. Three examples of NPPs, besides others of the same reactor type, can be mentioned which may benefit from this study.

Dukovany NPP is situated in the Czech Republic and consists of four units of VVER-440/213 reactors. The operation of the oldest Unit 1 started in 1985. The design operation life of this type of reactors is thirty years and expired in 2015. Recently, (in 2016–2017), the operation license of all four units was extended for an indefinite period with the next planned inspection in 2025. The situation in Hungarian Paks NPP is similar. It also consists of four units of VVER-440/213 reactors. The Unit 1 is under the operation since 1982. During 2012 and 2017, all the units were granted a license extension for additional 20 years of operation. Consequently, their total permitted operation time is 50 years. Loviisa NPP in Finland consists of two units of VVER 440/213 reactors. The Unit 1 is under operation since 1977 and similarly to the above described Dukovany and Paks NPPs it has an operation license till 2027, which corresponds to 50 operational years. The Unit 2 of the Loviisa NPP also has an operation license for 50 years, i.e. to the end of year 2030. As a difference from the Dukovany and Paks NPPs, at Loviisa NPP 36 outermost fuel assemblies are replaced with “shield elements” therefore the neutron flux and operation temperature are lower.

This chapter presents a numerical approach to predict the VVER-440/213 CBS behavior under long-term irradiation, which also considers the temperature and creep effects. The presented numerical approach utilizes the latest research results related to concrete degradation under irradiation and operation temperature as well as the real experimental measurements and numerical estimations of the neutron flux and temperatures generated by VVER-440/213 reactors during their normal operation. The ultimate goal of the study presented in this chapter is to assess the possible mechanical response and the state of the CBS under normal power plant operational condition.

3.2 Formulation of problem

3.2.1 Geometry

CBS of VVER-440/213 reactor is a self-bearing cylindrical wall with the inner radius of 2.37 m, the outer radius of 3.07 m and the height of 2.8 m. The upper 0.6 m of the cylindrical wall is truncated from the outer side upward at an angle of 45° as shown in Figure 3.1.

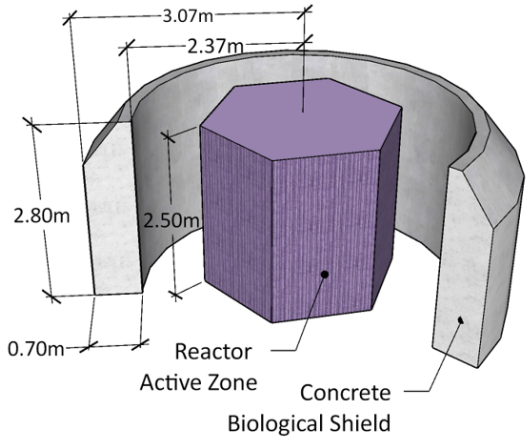

Figure 3.1: Geometry of CBS of VVER-440/213 reactor.

3.2.2 Neutron flux

In order to obtain the neutron flux distribution on the inner surface of the CBS, detailed 3D neutron transport calculations were performed for the volume residing between the outer boundary layer of the active core and the inner boundary layer of the CBS, using the MCNP4C code with the appropriate Evaluated Nuclear Data File cross-section libraries. The neutron flux distributions on the core-volume interface were generated by detailed 3D reactor-physics calculations for the core. The Monte Carlo N-Particle neutron transport calculations for the given volume take into account the real 3D structure of the core baffle, the downcomer, the reactor pressure vessel wall and the cavity, so the neutron flux and neutron fluence results for the inner boundary layer of the CBS are adequate. The obtained neutron flux with the maximum value

of $4.95{\cdot}10^{10}$ n/cm^2/s for the fast neutrons (> 0.1 MeV) corresponds to the direct flux measurements.

The 60-degree symmetry of the azimuthal flux distribution was assumed due to the hexagonal shape of VVER reactor active core, (Košťál et al., 2016; Toth et al., 2006). The height and the azimuthal neutron flux distribution are shown schematically in Figure 3.2 a) and b), respectively. The accumulated neutron fluence at different time intervals was calculated as the sum of the flux, with the realistic assumption of 300 operational days per year. The total neutron fluence on the inner surface of the biological shield is shown in Figure 3.3 (data provided by MTA Centre for Energy Research, Budapest).

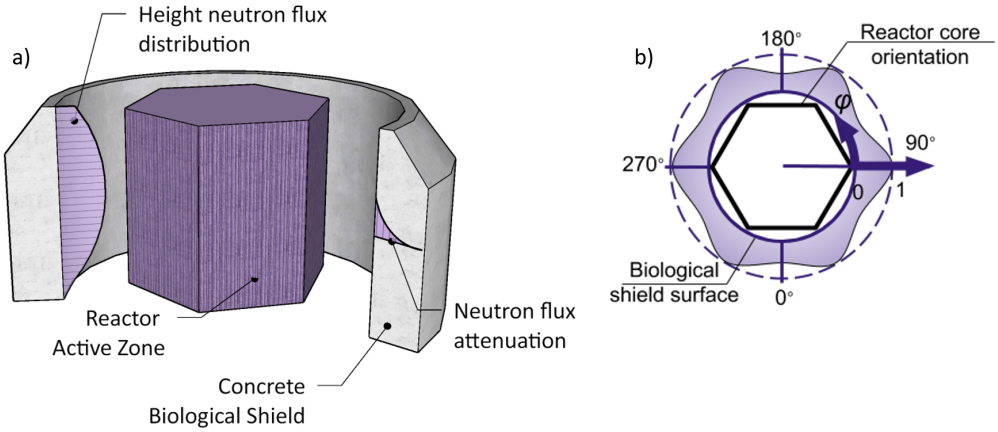

Figure 3.2: Neutron flux distribution: a) height neutron flux distribution and neutron flux attenuation, b) azimuthal neutron flux distribution.

The neutron flux over the thickness of concrete decreases due to the attenuation which, as the first and crude estimation, is defined by the exponential neutron attenuation law

$$f(d) = f_{surf} \cdot e^{-\Sigma_R d}, \tag{3.1}$$

where $f(d)$ is the neutron flux at a given depth under the inner surface of the biological shield, f_{surf} is the neutron flux on the inner surface of the biological shield, $\Sigma_R = 0.191$ 1/cm is the neutron removal cross section which corresponds to Portland concrete and is in accordance with (Esselman and Bruck, 2013) and d is the depth under the inner surface of the biological shield given in cm, (Khmurovska and Štemberk,

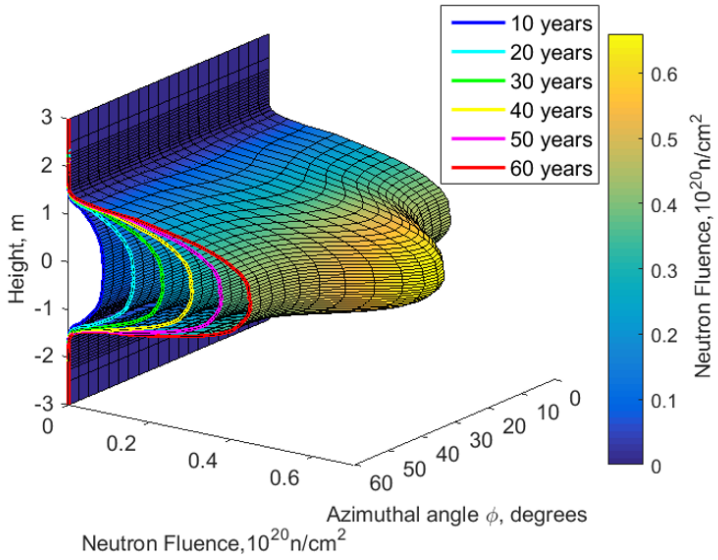

Figure 3.3: Neutron fluence distribution on inner surface of CBS over time (data provided by MTA Centre for Energy Research, Budapest).

2018; William et al., 2013). The neutron flux attenuation effect is schematically shown in Figure 3.2 a).

In this way, the neutron flux and, subsequently, the neutron fluence can be defined at any point on the inner surface as well as under the inner surface of the biological shield at any given time instant.

3.2.3 Temperature

The temperature distribution was obtained from a 1D numerical analysis of Loviisa NPP biological shield and represents the "full" core, thus corresponds to the temperature at the Dukovany and Paks NPPs and slightly overestimates that at the Loviisa NPP. The 1D temperature field is used with the assumption of insignificant temperature gradient in azimuthal and vertical directions. The calculated temperature field is in accordance with the measured reference values at Dukovany and Paks NPPs and is shown in Figure 3.4 (data provided by Fortum Power and Heat Oy, Espoo). It should be noted that the highest temperature is located inside the CBS and not on the surface due to the consideration of gamma radiation heating.

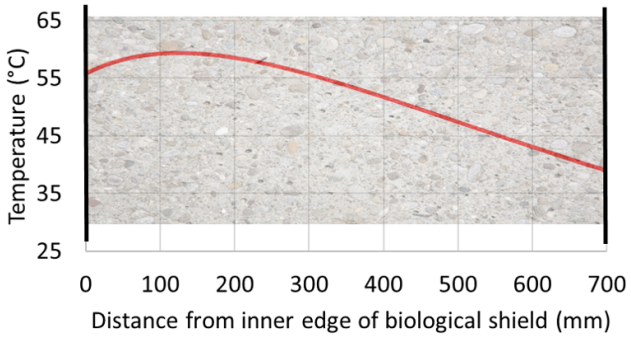

Figure 3.4: Temperature distribution in CBS in operation (data provided by Fortum Power and Heat Oy, Espoo).

3.2.4 Concrete degradation caused by irradiation

The RIVE of aggregates is considered to be a primary factor which causes irradiation-induced concrete degradation. Since the aggregate type varies from study to study, the degradation of concrete properties are expressed as a normalized value at a given neutron fluence, (Field et al., 2015), see Figure 3.5, Figure 3.6 and Figure 3.7, where the gray area denotes 90 % confidence interval of the experimental measurements, the black dashed curve indicates an average trend and the blue, green and red lines denotes maximum neutron fluence on the surface of the VVER-440/213 biological shield after 10, 30 and 60 years of operation, respectively. The best fitting of the average trends can be expressed analytically as follows (Le Pape, 2015)

$$\begin{aligned} R_E^{irr} &= E^{irr}/E^0 = \exp[-(b_{irr}\cdot\Phi)^{a_{irr}}], \\ a_{irr} &= 4.025\cdot 10^{-1}, \\ b_{irr} &= 4.073\cdot 10^{-22}\ \mathrm{cm}^2/\mathrm{n}, \end{aligned} \tag{3.2}$$

$$\begin{aligned} R_{f_c}^{irr} &= f_c^{irr}/f_c^0 = \exp[-(b_{irr}\cdot\Phi)^{a_{irr}}], \\ a_{irr} &= 1.582, \\ b_{irr} &= 7.253\cdot 10^{-21}\ \mathrm{cm}^2/\mathrm{n}, \end{aligned} \tag{3.3}$$

$$
\begin{aligned}
R_{f_t}^{irr} &= f_t^{irr}/f_t^0 = \exp[-(b_{irr}\cdot\Phi)^{a_{irr}}], \\
a_{irr} &= 4.364\cdot 10^{-1}, \\
b_{irr} &= 8.649\cdot 10^{-21}\ \mathrm{cm}^2/\mathrm{n},
\end{aligned}
\tag{3.4}
$$

where R is the reduction factor, E, f_c, f_t are the elastic modulus, the compressive and the tensile strength, respectively, the superscript 0 indicates the initial value and the superscript irr denotes the value after irradiation at a given fluence, Φ is the neutron fluence, a_{irr} and b_{irr} are fitted material constants according to Le Pape (2015).

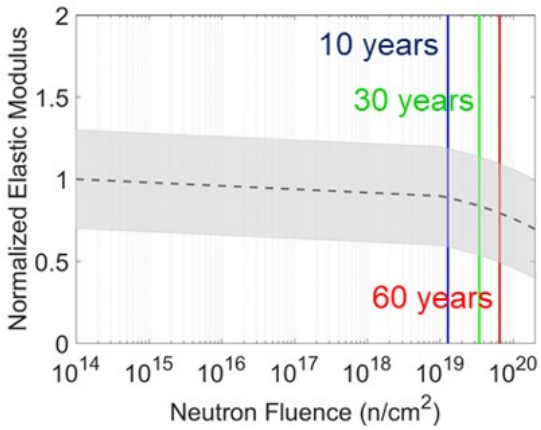

Figure 3.5: Concrete elastic modulus degradation caused by irradiation.

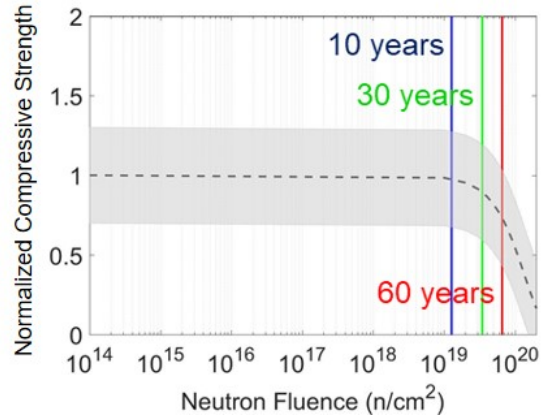

Figure 3.6: Concrete compressive strength degradation caused by irradiation.

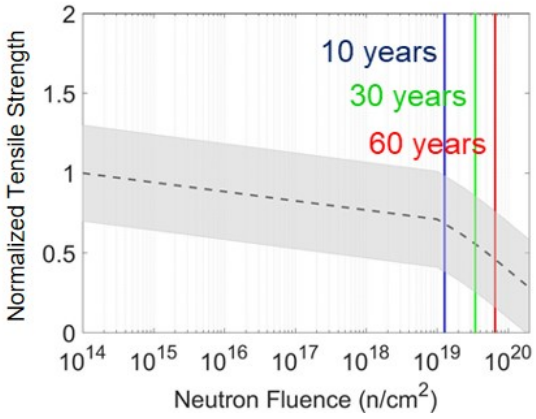

Figure 3.7: Concrete tensile strength degradation caused by irradiation.

The radiation induced elastic modulus degradation is shown in Figure 3.5 and the average trend, which is used in the modeling, is expressed by Equation 3.2. Similarly, the radiation induced compression and tension strength degradation is shown in Figure 3.6 and Figure 3.7 and is expressed by Equation 3.3 and Equation 3.4, respectively.

3.2.5 Concrete degradation caused by operation temperature

The temperature at which the shielding concrete works during normal operation of the NPP unit along with the gamma radiation heating can cause non-uniform thermal expansion of aggregates and cement paste and the subsequent degradation of concrete. Heating up to 120 °C affects concrete properties slightly, (Lee et al., 2009). Elevated temperature induced elastic modulus degradation under stressed condition shows a linear trend and can be expressed as, (William et al., 2009; Nielsen et al., 2004),

$$\begin{aligned} R_E^{temp} &= E^{temp}/E^0 = 1 - 0.1\theta, \\ \theta &= (T - T^0)/100, \\ 0 &\leq \theta \leq 10, \end{aligned} \tag{3.5}$$

where T is the specimen temperature in °C and the superscript $temp$ denotes the value of specimens under thermal load at given temperature, while the superscript 0

indicates the initial value.

The change of the concrete compressive strength under elevated temperature shows a parabolic reduction and can be expressed as follows, (William et al., 2009; Nielsen et al., 2004),

$$\begin{aligned} &R_{f_c}^{temp} = f_c^{temp}/f_c^0 = 1 - 0.016\theta^2, \\ &0 \leq \theta \leq 7.9. \end{aligned} \tag{3.6}$$

The concrete tensile strength degradation is expressed by a piecewise linear function, (Phan, 1996; William et al., 2009),

$$\begin{cases} R_{f_t}^{temp} = f_t^{temp}/f_t^0 = 1, & 20°C < T < 50°C, \\ R_{f_t}^{temp} = f_t^{temp}/f_t^0 = 1 - 0.1356\theta, & 0 \leq \theta \leq 6.4, \\ R_{f_t}^{temp} = f_t^{temp}/f_t^0 = 0.2, & 640°C < T < 800°C. \end{cases} \tag{3.7}$$

3.2.6 RIVE

Due to the fact that the CBS is a self-bearing structure, i.e. it supports only itself, the RIVE of aggregates becomes the primary acting load. The RIVE depends on aggregate composition, as was mentioned above. All existing data regarding the RIVE are collected in Hilsdorf et al. (1978); Field et al. (2015); Kontani et al. (2010) and Maruyama et al. (2017). Since the data regarding serpentinite and barite, either of which were used as the coarse aggregate in the concrete in Dukovany, Paks and Loviisa NPPs, are limited, the data available in Le Pape (2015) for structural concrete were used in the presented modeling and were expressed by the so-called Zubov function, (Zubov and Ivanov, 1966),

$$\varepsilon^{RIVE} = k\varepsilon_{max}\frac{e^{\delta\Phi} - 1}{\varepsilon_{max} + ke^{\delta\Phi}}, \tag{3.8}$$

where ε^{RIVE} is the RIVE strain, $\varepsilon_{max} = 0.936$ % is the maximum RIVE strain, $k = 0.968$ % and $\delta = 3.092 \cdot 10^{-20}$ cm^2/n are material parameters according to Le Pape (2015).

Equation 3.8 is visualized in Figure 3.8 with the black full line, while the black dashed lines denote the minimum and the maximum RIVE which cover the 90 % confidence interval of the existing experiments, which are explained in detail in Le Pape (2015). The blue, green and red lines in Figure 3.8 denote the maximum fluence on the inner surface of the biological shield after 10, 30 and 60 years of operation, respectively.

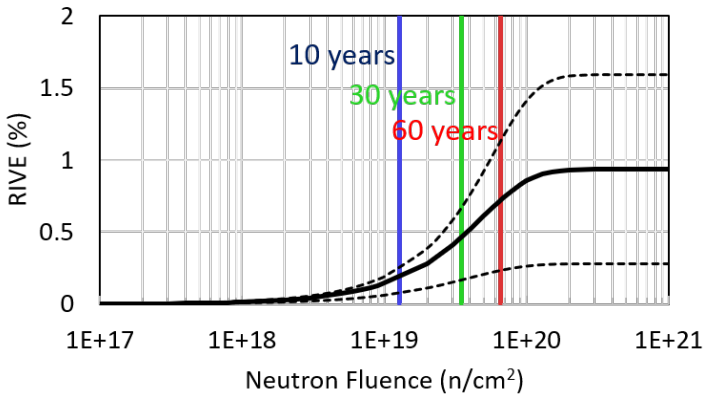

Figure 3.8: RIVE of structural concrete.

3.2.7 Thermal expansion

Another significant load which affects the CBS is the thermal expansion. The experimental data regarding the effect of irradiation on the coefficient of thermal expansion is limited. The data for α-quartz aggregates (Le Pape et al., 2016) are used in the presented numerical approach as the most comprehensive of the available data and are expressed by

$$\alpha_{aggr} = \alpha_0 + \alpha_1 \left(1 - \frac{1 - e^{-\varepsilon^{RIVE}/\varepsilon_C}}{1 + e^{(\varepsilon^{RIVE} - \varepsilon_L)/\varepsilon_C}} \right), \tag{3.9}$$

where α_{aggr} is the coefficient of thermal expansion of α-quartz aggregates, $\alpha_0 = -0.52 \cdot 10^{-6}$ 1/°C is the coefficient of thermal expansion of α-quartz after phase transformation due to elevated temperature, $\alpha_1 = 8.63 \cdot 10^{-6}$ 1/°C, $\varepsilon_C = 0.85$ % and $\varepsilon_L = 4.27$ % are fitted material parameters according to Le Pape et al. (2016).

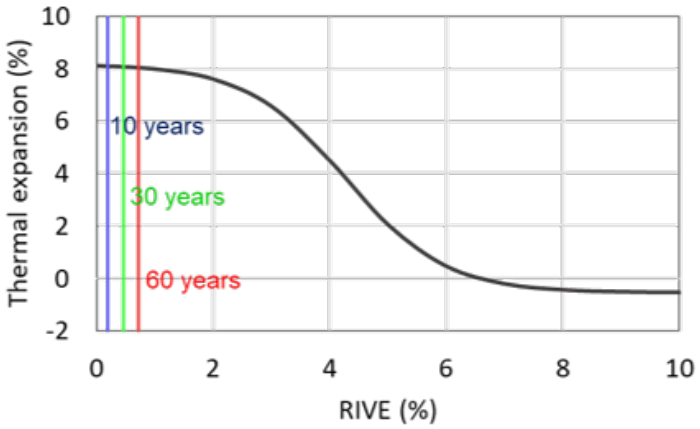

Figure 3.9: Coefficient of thermal expansion of irradiated α-quartz.

Figure 3.9 shows the change of the coefficient of thermal expansion of α-quartz as a function of RIVE with indication of the maximum RIVE on the surface of the biological shield after 10, 30 and 60 years in blue, green and red, respectively.

The total coefficient of thermal expansion of concrete, which considered its dependence on RIVE, was calculated as

$$\alpha_{concrete} = V_{aggr}\alpha_{aggr} + V_{cem}\alpha_{cem}, \tag{3.10}$$

where α_{cem} is the coefficient of thermal expansion of cement paste independent of irradiation, V_{aggr} and V_{cem} are the volume fractions of aggregate and cement paste in concrete mixture, respectively.

It should be noted that the empirical curve defined by Equation 3.10 is valid for quartz only, however, the change is insignificant (see Figure 3.9) and rather it shows the possibilities of the numerical code.

3.3 Numerical approach and validation

In order to carry out the numerical simulation of the biological shield, the nonlinear finite element method (FEM) code was written in MATLAB (the possibility of Rigid-Body-Spring model (RBSM) analysis was also considered, see section A.1). The basic parameters which are used in the analysis are summarized in Table 3.1, where ν is Poisson's ratio, A_c, B_c, A_t, B_t are the damage model constants which define the shape

of the stress-strain diagram, w_{cr}, c_{cr} and a_{cr} are water, cement and aggregate (fine and coarse) content in kg per 1 m^3 of concrete, respectively, t' is the age of concrete at the beginning of loading in years.

The biological shield was modeled in 3D using the 12-degrees of freedom linear tetrahedrons. The problem was considered as quasistatic.

When the degradation of the concrete properties due to irradiation and operation temperature was determined, it was possible to define the concrete properties at any point of biological shield at any time by

$$E^{\wedge} = R_E^{irr} \cdot R_E^{temp} \cdot E^0, \tag{3.11}$$

$$f_c^{\wedge} = R_{f_c}^{irr} \cdot R_{f_c}^{temp} \cdot f_c^0, \tag{3.12}$$

$$f_t^{\wedge} = R_{f_t}^{irr} \cdot R_{f_t}^{temp} \cdot f_t^0, \tag{3.13}$$

where the superscript $\wedge$ denotes the value after irradiation at operation temperature.

Mazars' "μ damage model", which is based on Mazars' damage model (Mazars and Pijaudier-Cabot, 1989; Mazars et al., 2015), was used in the presented numerical approach. The Mazars damage model can be used for radiation induced damage analysis and shows acceptable results according to (Le Pape, 2015). The isotropic mechanical damage D^{mech} is calculated using the "μ damage model" as

$$R_E^{mech} = 1 - D^{mech}, \tag{3.14}$$

$$E = R_E^{irr} \cdot R_E^{temp} \cdot R_E^{mech} \cdot E^0, \tag{3.15}$$

where R_E^{mech} is the reduction factor due to mechanical damage. The damage surface then can be defined after specification of the reduced elastic modulus, the compressive and tensile strength. Equation 3.15 is mathematically equal to

$$\begin{aligned} E &= (1 - D) \cdot E^0, \\ D &= 1 - (1 - D^{irr})(1 - D^{temp})(1 - D^{mech}), \end{aligned} \tag{3.16}$$

presented in (William et al., 2013; Nechnech et al., 2002), where $(1–D_{irr}) = R_E^{irr}$ and $(1–D_{temp}) = R_E^{temp}$ represent the isotropic damage due to irradiation and the operation temperature effect, respectively. The following approach assumes irradiation-

Table 3.1: Material properties used in modeling.

Parameter	Value	Reference
	Elastic properties	
E^0, [GPa]	30.0	Vaitová et al. (2018)
ν	0.2	Vaitová et al. (2018)
f_c^0, [MPa]	20.0	Vaitová et al. (2018)
f_t^0, [MPa]	2.5	Vaitová et al. (2018)
	Neutron Fluence	
Φ, [n/cm^2]	Equation 3.1,Figure 3.3	*,Esselman and Bruck (2013)
	Temperature	
T, [°C]	Figure 3.4	*
	Properties reduction	
R_E^{irr}	Equation 3.2, Figure 3.5	Le Pape (2015)
$R_{f_c}^{irr}$	Equation 3.3, Figure 3.6	Le Pape (2015)
$R_{f_t}^{irr}$	Equation 3.4, Figure 3.7	Le Pape (2015)
R_E^{temp}	Equation 3.5	William et al. (2009)
$R_{f_c}^{temp}$	Equation 3.6	William et al. (2009)
$R_{f_t}^{temp}$	Equation 3.7	William et al. (2009)
	"μ damage model" parameters	
A_c	1.82	Mazars et al. (2015)
B_c	1023	Mazars et al. (2015)
A_t	1.0	Mazars et al. (2015)
B_t	10000	Mazars et al. (2015)
	B3 model parameters	
w_{cr}, [kg/m^3]	190	**
c_{cr}, [kg/m^3]	499	**
a_{cr}, [kg/m^3]	1676	**
t', [years]	3	***
	Load parameters	
ε^{RIVE}, [%]	Equation 3.8,Figure 3.8	Le Pape (2015)
α_{aggr},[1/°C]	Equation 3.9,Figure 3.9	Le Pape et al. (2016)
α_{cem},[1/°C]	$10 \cdot 10^{-6}$	Le Pape et al. (2016)
$\alpha_{concrete}$,[1/°C]	Equation 3.10	***
T^0, [°C]	25	***

* measured and calculated environmental conditions during the normal operation of NPP.
** real structural concrete mixture composition for Dukovany NPP.
*** estimated parameters.

induced damage and mechanical damage independent, however, it may be overly conservative.

According to the current research (Gray, 1971; Denisov et al., 2012; Dubrovskii et al., 2010) and experimental investigation of effect of gamma-rays on cement mortar creep presented in Chapter 4, the influence of irradiation on concrete creep appears to be insignificant. Therefore, the effect of irradiation on concrete creep may be neglected and the commonly accepted B3 model (Bažant and Jirásek, 2018) can be used. Since the steel liner, which covers CBS, prevents concrete drying, only the basic creep was taken into account with the assumption of constant relative humidity in the concrete body. Then, according to the B3 model, the basic creep of concrete depends on the concrete composition, the concrete stiffness, the stress level, the load duration and the age of concrete structure.

The interaction between the damage model and the creep model was carried out by coupling the models using the staggered algorithm with the following constitutive equation

$$\sigma = E \cdot (\varepsilon_{tot} - \varepsilon_{irr} - \varepsilon_{temp} - \varepsilon_{cr}), \tag{3.17}$$

where σ is the stresses, E is the elastic modulus defined by Equation 3.15, ε_{tot} is the total strain, ε_{irr} is the linear strain due to the RIVE, ε_{temp} is the thermal strain and ε_{cr} is the creep strain defined as follows

$$\begin{aligned} \varepsilon_{irr} &= \tfrac{\varepsilon^{RIVE}}{3}, \\ \varepsilon_{temp} &= \alpha_{concrete} \cdot \Delta T, \\ \varepsilon_{cr} &= J_{cr} \cdot \sigma, \end{aligned} \tag{3.18}$$

where $\alpha_{concrete}$ is the coefficient of thermal expansion defined by Equation 3.10, ΔT is the temperature change, ε^{RIVE} is the RIVE strain defined by Equation 3.8, J_{cr} is the creep compliance defined by B3 model (Bažant and Jirásek, 2018).

Since the mechanical damage may grow even under constant stresses, the strain, which drives the evolution of mechanical damage, is calculated as follows

$$\varepsilon_{tot} = \varepsilon_{tot} - \varepsilon_{irr} - \varepsilon_{temp} - (1 - \beta) \cdot \varepsilon_{cr}, \tag{3.19}$$

where β is a material parameter, which, as the crude estimation, is equal to 0.2 according to Mazzotti and Savoia (2003).

The system of nonlinear equations was solved using the force-controlled modified Newton-Raphson method in each time step with the time increment equal to a quarter of a year. The system of nonlinear equations converges when the sum of squares of the residual divided by the sum of squares of the applied force is less than $1{\cdot}10^{-6}$. The iteration process was then stopped when the convergence was achieved. Then, the solver proceeded to the next time step. The concise flowchart of the analysis is shown in Figure 3.10.

The 60-degree segment of the biological shield was analyzed with the assumption of the flux symmetry due to the 60-degree symmetry geometry of the reactor active zone (see Figure 3.2). The regular finite element mesh with the maximum element size of 7 cm, which was used in the analysis, and the applied boundary conditions are shown in Figure 3.11.

The developed FEM code was validated with available related experimental data. The validation was performed according to the experiment presented in Kommendant et al. (1976) where the concrete for NPPs was studied. The concrete cylinders with the radius of 76.2 mm and the height of 406.4 mm made of concrete with the compressive strength of 45 MPa were insulated and subjected to a sustained load of 14.48 MPa, which does not cause damage to the samples, and 29.3 MPa, which causes damage of the samples. The loading started at the sample age of 28 days. The concrete mixture was composed of 449 kg/m^3 of cement, 170 kg/m^3 of water and 1810 kg/m^3 of aggregates (fine and coarse). The strain calculated using the developed code shows good correlation with the experimental data, see Figure 3.12 for both undamaged and damaged concrete.

3.4 Results and discussion

According to the numerical simulation, the CBS is already severely damaged after the simulated 12.75 years of normal operation, when the solver was not able to find an equilibrium of the analyzed structure since the force-controlled Newton-Raphson

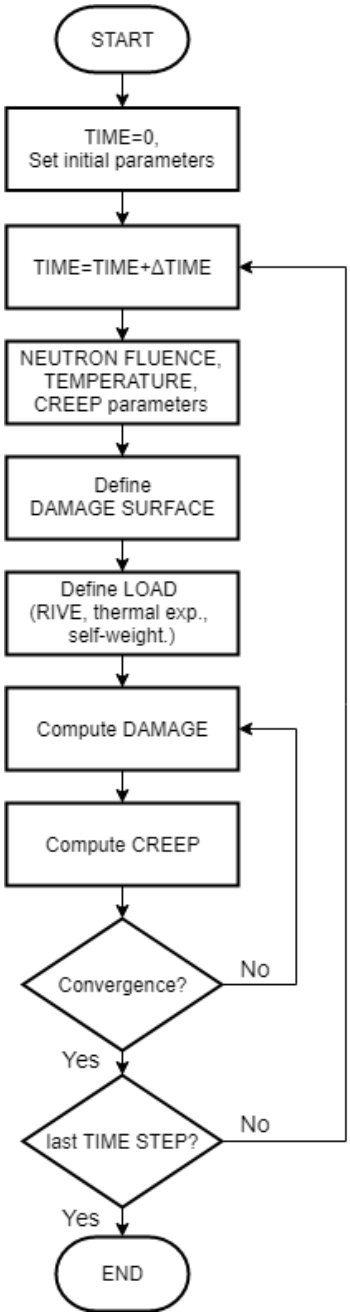

Figure 3.10: Concise flowchart of analysis.

method was used in the developed code. Then, the 12.75 years indicate the end of the theoretical structural integrity time of the analyzed biological shield in this study.

The corresponding displacements, the principal tensile stresses and the damage of the biological shield in the case which takes into account creep and temperature effect

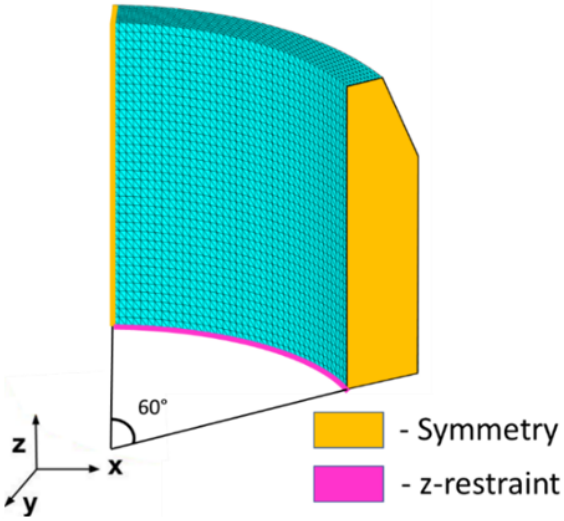

Figure 3.11: Finite element mesh with applied boundary conditions.

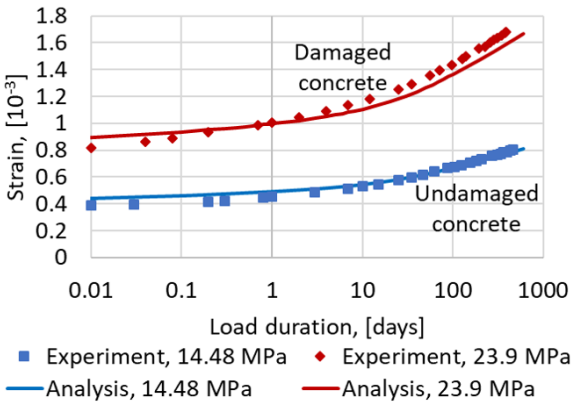

Figure 3.12: Validation example.

are shown in Figure 3.13 a), Figure 3.14 a) and Figure 3.15 a), while the displacements, the principal tensile stresses and the damage which were calculated without creep and temperature effect are shown in Figure 3.13 b), Figure 3.14 b) and Figure 3.15 b). The structural integrity time for these two cases remained unchanged and equal to 12.75 years due to the negative effect of temperature change (increase of stresses) and positive effect of creep (stresses redistribution). However, the displacements, principal stresses distribution and the damage varied, see Figure 3.13, Figure 3.14 and Figure 3.15.

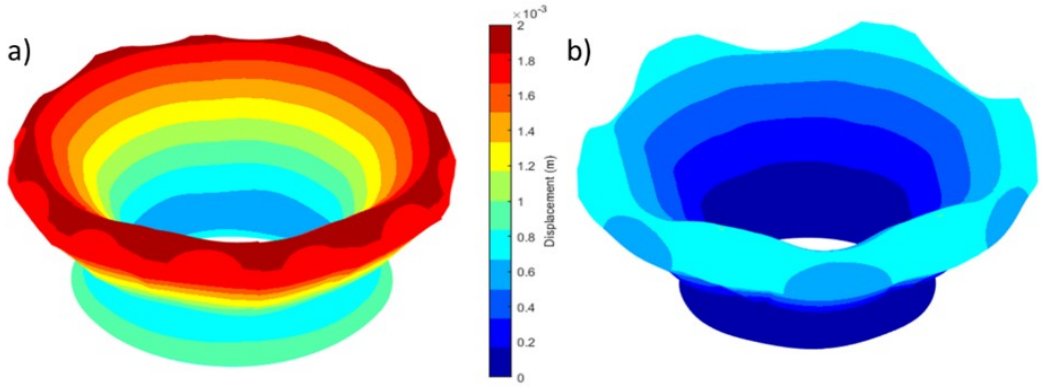

Figure 3.13: Displacement of biological shield after 12.75 years of normal operation (Magnification=5000): a) with creep and temperature, b) without creep and temperature.

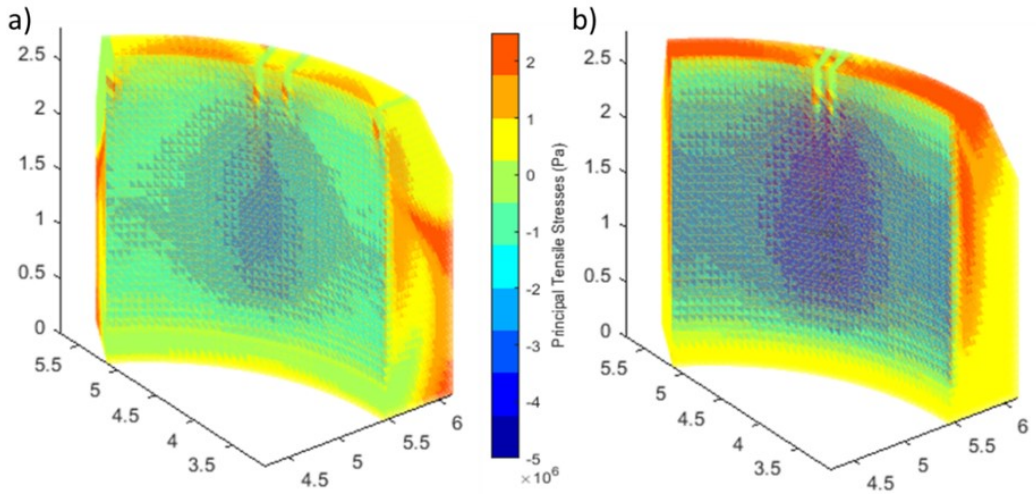

Figure 3.14: Principal tensile stresses in biological shield after 12.75 years of normal operation: a) with creep and temperature, b) without creep and temperature.

The compressive stresses in Figure 3.14, which are much lower than the compressive strength, appear in the zone which is affected by the neutrons, but the upper part and the outer surface of the analyzed structure is under significant tension due to the structural response. It can be seen that the principal tensile stresses achieve their limit, which implies the occurrence of cracks and, as shown in Figure 3.15, the deep radial cracks develop from the upper part of outer surface of the analyzed structure and propagate inward.

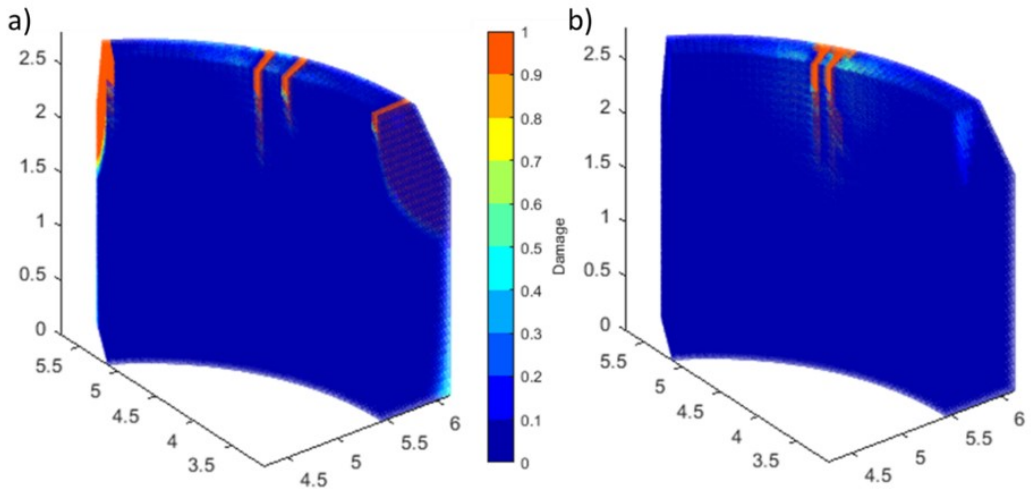

Figure 3.15: Damage in biological shield after 12.75 years of normal operation: a) with creep and temperature, b) without creep and temperature.

The effect of creep on the CBS plays an extremely important role in its structural performance. According to the presented numerical simulation, the theoretical structural integrity time of the analyzed structure decreases to 2.00 years from initial 12.75 years in the analysis without creep but with temperature because of the concentration of the huge thermal stresses near the supports due to the rapid heating. This is in accordance with Giorla et al. (2017), which also shows the damage delay due to the creep. It should be noted that when the creep is not considered, the damage is localized in the support area, which will not result in reduction of the load-bearing capacity or the shielding properties of the analyzed self-bearing structure, but rather it indicates changes in the damage pattern. Therefore, since the creep not only slows down the damage evolution but also changes the damage pattern, it is recommended to perform the coupled creep-damage analysis of the CBS in 3D due to the highly non-uniform load distribution. The above also emphasizes the serious need to conduct an experimental investigation on the effect of radiation on the concrete creep in order to clarify the radiation induced creep mechanism. In the following analysis, the case with the creep and temperature effect which is shown in Figure 3.13 a), Figure 3.14 a) and Figure 3.15 a) is taken in consideration.

In order to estimate the creep sensitivity, these parameters were selected: concrete

composition, the age of concrete at loading and the β parameter (Mazzotti and Savoia, 2003). Firstly, the mixture with the composition presented in Kommendant et al. (1976) was used in the analysis. The strength and the elastic modulus remained unchanged and as a result the structural integrity time reduced to 12.00 years from 12.75 years. Secondly, the age of concrete at loading was changed to one year from the realistic three years and as a result the structural integrity time increased to 15.50 years for concrete mixture presented in Table 3.1 and to 15.00 years for concrete mixture presented in Kommendant et al. (1976). Thirdly, the β parameter varied from 0 to 0.35 and as a result the structural integrity time varied within the limit of ± 5 %. Therefore, the reasonable alteration of the creep parameters affects the rate of damage development insignificantly.

The important aspect in these results is that with consideration of the RIVE lower limit (see Figure 3.8), the calculated structural integrity time of the CBS increases to 35.25 years from the initially obtained 12.75 years, which corresponds to the maximum fluence of $4.02 \cdot 10^{19}$ n/cm^2. Similarly, with consideration of the RIVE upper limit, the structural integrity time decreases to 10.00 years, which corresponds to the maximum fluence of $1.28 \cdot 10^{19}$ n/cm^2. The obtained neutron fluence value is in accordance with the limit value for the fast neutrons proposed by United States Nuclear Regulatory Committee, (US NRC, 2016), and the new reference value proposed in Japan for the fast neutron fluence, (Maruyama et al., 2017), which is equal to $1 \cdot 10^{19}$ n/cm^2. Here it should be noted that the biological shield of some PWR reactors which are used in the USA and Japan is not only a shielding structure but also a load-bearing structure, (Rosseel et al., 2016). Therefore, its damage or displacement may result in serious consequences. On the other hand, the biological shield of the VVER reactors is a shielding structure only, and thus, its damage or displacement will not affect the containment structural performance or the designed reactor position.

It should be also noted that the neutron attenuation due to the steel sheet liner of the thickness of 1.2 cm, which covers the CBS, was not taken into account in the presented simulation, which is a conservative assumption. According to the past and current research, the neutron removal cross section of different steel varies from 0.1586 to 0.2103, (Kassab et al., 2015; El-Khameesy et al., 2015). Then, even with more

undervalued estimation when the neutron removal cross section of steel is equal to that of iron, 0.1576 1/cm (Snyder and Neufeld, 1957; Lamarsh and Baratta, 2001), the maximum flux reduces to $2.48 \cdot 10^{10}$ n/cm^2/s from the originally considered maximum value of $4.95 \cdot 10^{10}$ n/cm^2/s and the critical damage of the biological shield is reached after 15.25 years of operation instead of the calculated 12.75 years, when the mean RIVE curve is used.

It should be also noted that the analysis uses theoretical values of the concrete stiffness and the strengths in tension and compression. However, the real values can by much higher. For example, Altynbaev et al. (2016) provides the mean value of concrete compressive strength during the construction of Unit 1 of Balakovo Nuclear Power Plant in 1980 of 40 MPa and the minimum value of 30 MPa with the design value of 20 MPa. If the real minimum value of the initial compressive strength of 30 MPa with the corresponding initial tensile strength of 2.9 MPa and the modulus of elasticity of 32 GPa are used in the analysis, the critical damage of the CBS occurs after 18.00 years of operation instead of 15.25 years. Moreover, if the real mean value of the initial compressive strength of 40 MPa with the corresponding initial tensile strength of 3.5 MPa and the modulus of elasticity of 35 GPa are used, the critical damage occurs after 18.75 years of the normal operation. According to this parametric study, with consideration of the mean RIVE curve, the biological shield will be damaged critically during the design operational time anyway. However, it should be stated at this point that the damage to the analyzed biological shield does not affect the normal NPP operation. As can be seen in Figure 3.16, the truncated top of the biological shield is supplemented with an antisymmetric concrete wedge, which is also covered in a steel liner and which can attenuate the penetrating neutrons. The calculated result can be seen in Figure 3.16 a) when it is expected that the neutron will be fully attenuated by the biological shield and the supplementary concrete wedge. Nevertheless, hypothetically, when the crack pattern lets the neutrons go through the supplementary concrete wedge, the load-bearing concrete wall may be affected, however, the affected area will be very small, or even negligibly small when the thickness of the load-bearing concrete wall is considered, see Figure 3.16 b).

The temperature, at which the accelerated irradiation tests are carried out, varies

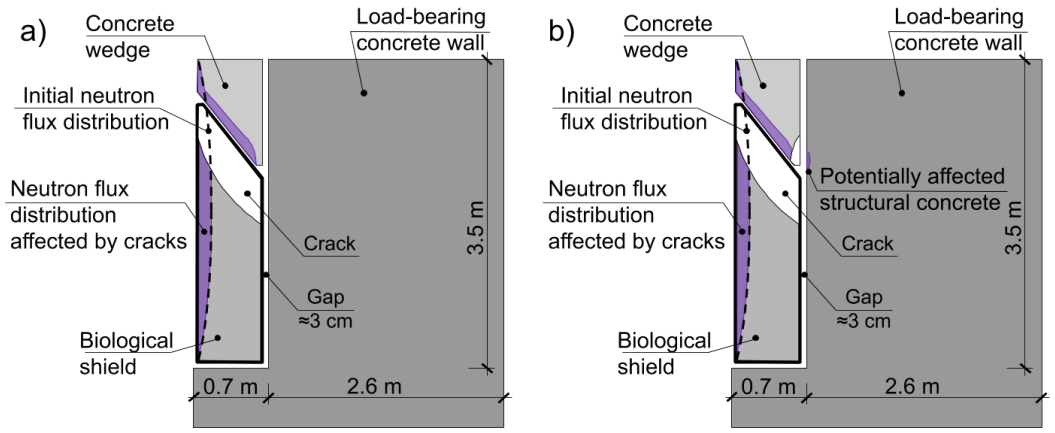

Figure 3.16: Redistribution of neutron flux and analysis of potential consequences: a) crack in CBS, b) crack in concrete wedge.

from 10 to 550 °C, according to Field et al. (2015) and William et al. (2013). The low temperature can speed up the RIVE significantly, while the high temperature results in the RIVE delay due to the thermal healing, (Bykov et al., 1981; Le Pape et al., 2016). That means that either the RIVE has to be a function of temperature as proposed in Maruyama et al. (2017) for α-quartz or only the data which were obtained under the temperature prevalent in the CBS (about 40 to 60 °C for VVER-440/213, see Figure 3.4) should be used in numerical simulations. The reason for this limitation is that the high temperature, under which some of the accelerated irradiation tests were carried out, leads to additional inaccuracy, when the concrete samples can be damaged by the irradiation as well as the elevated temperature during the accelerated irradiation tests.

3.5 Conclusions

The numerical approach to the coupled damage-creep analysis of VVER-440/213 CBS, which combines existing hypotheses and experimental data on irradiation and temperature effects on concrete with the real flux and temperature measurements and calculations was described in detail.

According to the result of the presented numerical simulation, the RIVE of aggregates is the primary factor that affects the structural performance of CBS. Never-

theless, it is emphasized that the effect of RIVE should be considered together with the temperature and creep effects in order to obtain realistic results.

The obtained results indicate that the CBS of VVER-440/213 reactor may be damaged critically as early as after 10 years of the NPP normal operation, when its shielding property is partially compromised. However, this fact does not affect the containment building or the reactor pressure vessel design performance as the biological shield is self-bearing statically-isolated structure. The partial reduction of shielding properties of the biological shield is compensated by the supplementing antisymmetric concrete wedge, which attenuates the permeating neutrons. Only hypothetically, as the material parameters were underestimated in the presented study, the neutrons may affect the load-bearing concrete wall, but the effect would be negligible with respect to the thickness of the load-bearing concrete wall, which supports the reactor pressure vessel. However, this result evidences the necessity of being able to predict the behavior of the biological shield of those PWR reactors which combine both the load-bearing and shielding function.

Chapter 4

Experimental investigation of effect of gamma-ray irradiation on cement mortar creep

The effect of gamma-ray irradiation on cement mortar creep is investigated at two different levels, mesoscale level (direct measurements of strain) and nanoscale level (nanoindentation). The creep investigation is accompanied by shrinkage measurements as well as XRD analysis, MIP and compressive strength test. The measured creep and shrinkage strain is compared with values calculated according to existing building standard models which showed that creep and shrinkage of both irradiated and control samples lie within the interval predicted by the building standard models. However, creep of irradiated samples is slightly higher due to increase in porosity. Nanoindentation creep compliance and nanoindentation elastic modulus of irradiated and control samples do not show any significant difference. The mineral composition obtained using XRD analysis of irradiated and control samples is also similar. The physics behind porosity increase is still unclear, but it leads to significant decrease in compressive strength (20 % on average).

4.1 Motivation

Since the change in creep may affect the performance of NPP CBS the effect of gamma-ray irradiation on the cement mortar creep is investigated in this chapter at two different levels, specifically, the mesoscale level (direct measurements of sample strain) and the nanoscale level (nanoindentation). In order to evaluate the pure creep, shrinkage was also measured on separate samples and subtracted from the total long-term deformation. In order to confirm the nanoscale changes, the indentation modulus of elasticity was measured. In order to determine the presence/absence of carbonation or any other change in the cement mortar mineral composition, the XRD analysis was carried out. The porosity of the cement mortar samples was measured because its change may have altered the cement mortar creep as well as the compressive strength, which was also measured.

4.2 Experiment

The mortar which consists of CEM I 42.5R cement paste with the water-cement ratio of 0.38, siliceous aggregates with the fraction of 0-4 mm and a polycarboxylate-based superplasticizer was used to produce small-scale 10x10x40 mm samples. The small-scale samples were selected in order to allow for the gamma-induced heat dissipation and uniform distribution of gamma-rays. The mortar and the cement compositions are given in Table 4.1 and Table 4.2, respectively. According to The Certification of Natural Aggregate Quarries of the Czech Republic (for Račice – Předonín 1 and 2 and Dobříň-jih 1-Předonín), the aggregates consist predominantly of quartz with small fragments of feldspar and mica. The mixture composition corresponds to the structural concrete mixture without coarse aggregate.

All samples were cured in water during 10 days and 62 more days in a sealed condition till the beginning of experiment. The insulation was provided by a polyethylene foil. The samples were loaded and irradiated just after insulation removal.

Six loading frames were designed and constructed (see Figure 4.1) in order to provide the sustained loading for the creep measurement. The load was controlled by the loading spring compression so that 1 cm of spring contraction is equal to

Table 4.1: Composition of mortar.

Component	Weight
Cement (CEM I 42.5R), [g]	2625
Water, [g]	1000
Siliceous aggregates with fraction of 0-4 mm, [g]	4200
Superplasticizer (Glenium ACE 442), [g]	25

Table 4.2: Chemical composition of CEM I 42.5R (Mokrá, Czech Republic) in % according to X-ray fluorescence elemental analysis*

CaO	SiO_2	Al_2O_3	Fe_2O_3	MgO	SiO_3	S	Cl	K_2O	Na_2O	Ig. loss	Insol. res.
65.00	19.00	4.00	3.00	1.00	3.00	0.04	0.05	0.75	0.15	3.10	0.70

* Data provided by Českomoravský cement, a.s.

the load of 0.5 kN. Two load levels of 1.0 kN and 1.5 kN (10 MPa and 15 MPa, respectively) were considered, which is approximately equal to 13.5 % and 20 % of sample strength. In order to separate shrinkage from the creep, not loaded samples were also investigated. Three load frames with three samples in each (9 samples it total, 4 samples of which were under the sustained load of 1.0 kN and 5 samples were under the sustained load of 1.5 kN) and 5 not loaded samples were irradiated. An identical set of control samples was placed in the same laboratory conditions (with the average temperature of 16.2 °C and the average relative humidity of 50 %) but away from gamma radiation, so as the presence/absence of gamma-ray irradiation is the only influencing parameter. The experimental setup is shown in Figure 4.2.

^{60}Co Irradiation Facility UGU-420 of The Joint Institute for Power and Nuclear Research - Sosny of the National Academy of Sciences of Belarus, Minsk with the following irradiator characteristics (the height of the active part is 50 cm; the generating dose rate is 0.1-10 Gy/s and the total number of sources is 768 with the total activity of $4.4 \cdot 10^{15}$ Bq (120 kCi)) was used in order to carry out the presented experimental investigation. The radiation dose rate was in the range from 3.90 kGy/h to 4.71 kGy/h. The average irradiation period was 8.6 hours per day (the irradiation facility

was operated during the day period only). The total absorbed dose after 369 days of irradiation varies from 12.0 MGy to 15.0 MGy for different samples. The length of samples was measured during the irradiation period using the high accuracy digital calipers in four different points of a sample and then averaged.

4.3 Post-irradiation examination

After the irradiation, one sample of each set (not loaded, 1.0 and 1.5 kN loaded irradiated samples and not loaded, 1.0 and 1.5 kN loaded control samples) were cut into 5 sections by a precision cut-off machine Brillant 210 with a diamond blade. The sample section from the sample ends was not used in further analyses. The adjacent

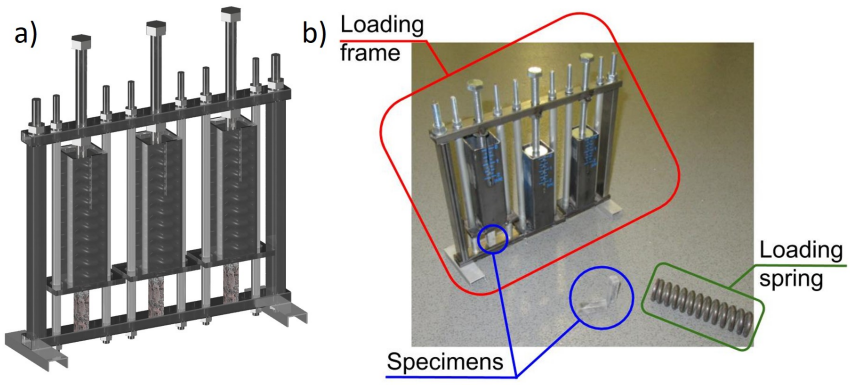

Figure 4.1: Loading frames: a) visualization, b) ready to use.

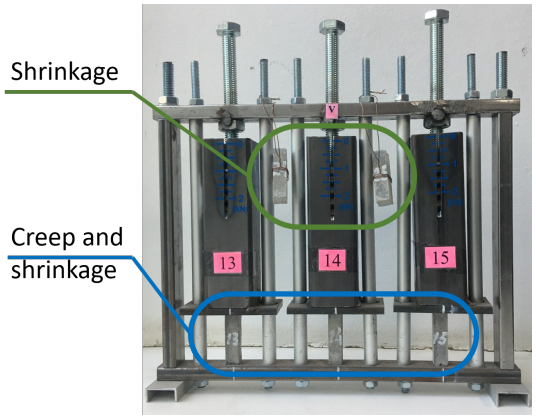

Figure 4.2: Experimental setup.

sections were used for the nanoindentation, powder X-ray diffraction (XRD) analysis and mercury intrusion porosimetry (MIP) test.

The surface of the sample sections, which were used for nanoindentation, was polished with silica carbide paper to achieve a smooth surface. The nanoindentation of the polished sample sections was carried out with a Hysitron Tribolab Ti-700 with the Berkovich diamond tip. Six grids of 8 x 8 indents with the spacing of 6 µm were predetermined on the surface of each sample while avoiding aggregates. The nanoindentation was performed using the load control test with the trapezoidal loading diagram. The sample surface was loaded by the diamond tip linearly during one second till the maximum force of 3 mN was reached with a following 40 seconds holding period and 1 second of unloading in order to evaluate the indentation creep compliance and the indentation elastic modulus. The nanoindentation was performed in the laboratory with the average environmental temperature of 22 °C and the average relative humidity of 50 %.

The sample sections, which were used for the XRD analysis were powdered and sieved through a 0.045 mm sieve. The randomly oriented powder mount technique was applied. The Bruker D8 DISCOVER diffractometer (at Institute of Fundamental Technological Research of Polish Academy of Science IPPT PAN) was used with a voltage ratio of 40 kV and 40 mA lamp current. The copper lamp was used as an X-ray source (radiation CuKα with a wavelength 0.1542 nm). The measurements were carried out in the reflection mode, using the Bragg-Brentano geometry with a 1-mm gap and two 2.5° solers on the primary and the secondary side. The angular ranging of 2θ measurements ranged from 5° to 65°, with a 0.02° step and a counting time of 1 s per step.

The sample sections which were used for the porosity evaluation were dried in oven at 50 °C for three days and were broken into pieces. The center piece without significant large aggregates were selected for further porosity investigation by the mercury porosimeter PASCAL 140 a 440.

The compressive strength test was performed on a standard laboratory compressive test machine on the 6 irradiated and 6 control samples. The obtained compressive strengths cannot be used for design purposes, however, since all the compressive

strengths were obtained in an identical manner they can be used for comparative assessment.

4.4 Results and discussion

4.4.1 Mesoscale level

The measured sample strains are shown in Figure 4.3, Figure 4.4 and Figure 4.5. It should be noted that the measurements of strain of the loaded samples were taken without significant difficulties due to the relatively high strain, while the shrinkage strain of the not loaded samples are on the threshold of measurability of the prescribed above method which complicated the processing of results.

In order to evaluate the average strain of the samples, the following logarithmic function was fitted to the measured data

$$\varepsilon_{tot}(t, t') = \alpha_{cr} \ln(t - t_0), \tag{4.1}$$

where $\varepsilon_{tot}(t, t')$ is the sample strain, t is the age of the sample in days, t' is the age of sample at loading/drying and α_{cr} is the fitted parameter. The fitted average curve as well as the 95 % confidence interval are also shown in Figure 4.3, Figure 4.4 and Figure 4.5. It can be seen that the shrinkage strain of the not loaded control samples

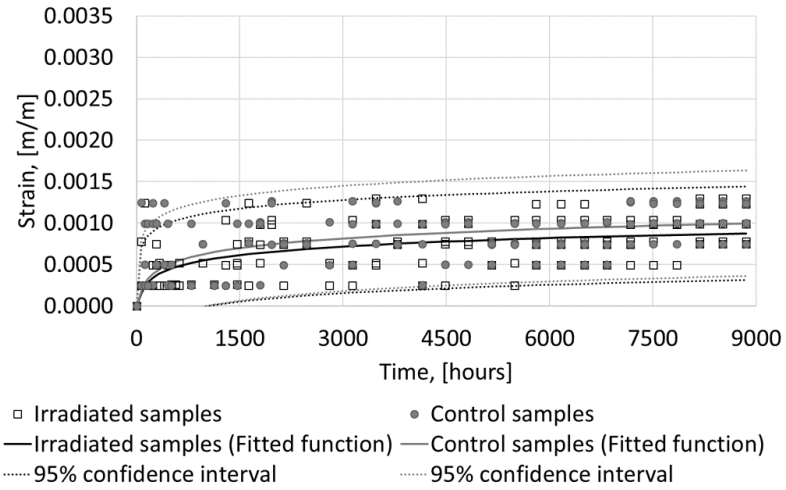

Figure 4.3: Shrinkage strain of not loaded samples.

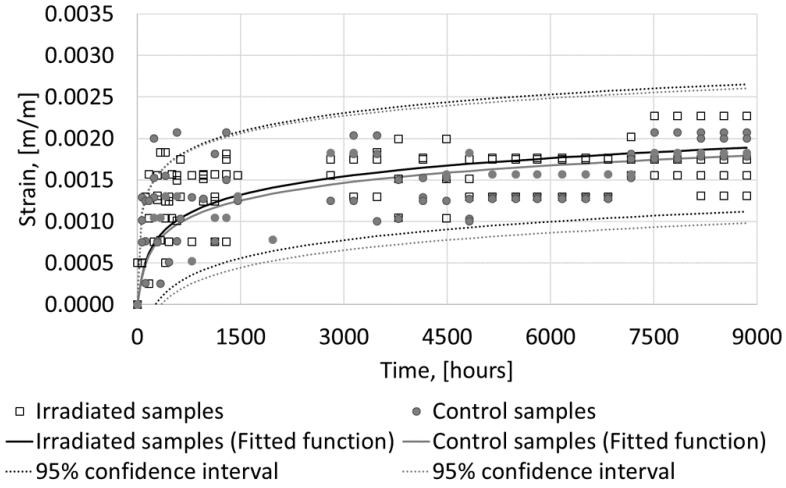

Figure 4.4: Strain of 1.0 kN loaded samples.

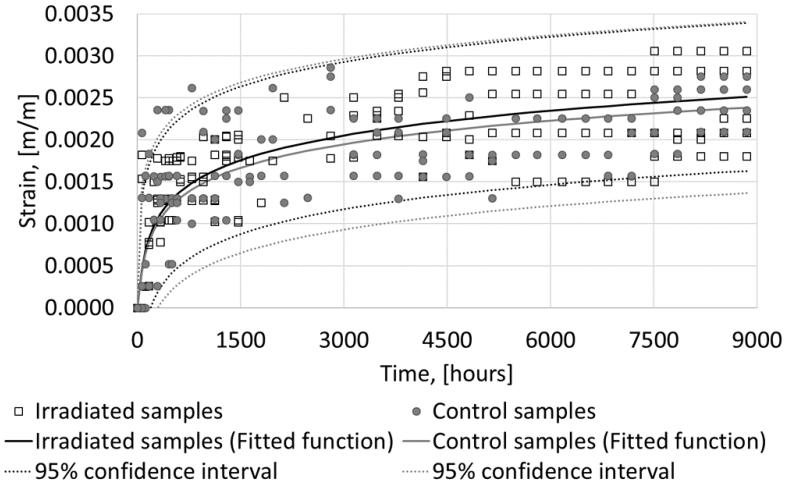

Figure 4.5: Strain of 1.5 kN loaded samples.

is insignificantly higher while the strain of the loaded control samples (the sum of the creep and the shrinkage) is slightly lower in comparison with the irradiated samples, but the difference is negligibly small and located within the 95 % confidence interval. Moreover, the 95 % confidence intervals of the control and the irradiated samples are very similar despite the large scatter of data.

The shrinkage and the creep strain were also calculated using the common standard models, namely B3 model (Bažant and Jirásek, 2018), CEB model according

to "CEB-FIP model code 1990." (Comité Euro-International du Béton, 1991), FIB model according to "fib model code for concrete structures 2010." (Fédération internationale du béton, 2013), ACI model according to "ACI Guide 209.2R-08" (ACI Committee 209, 2008) and GL2000 model as presented in "ACI Guide 209.2R-08" (ACI Committee 209, 2008; Gardner and Lockman, 2001). The comparison of the measured strain of the not loaded samples and the shrinkage strain calculated according to the standards is shown in Figure 4.6. While the comparison of measured strain of the loaded samples (1.0 kN and 1.5 kN) and the sum of the calculated creep and shrinkage strains is shown in Figure 4.7 and Figure 4.8.

It can be seen that the shrinkage strain of the not loaded samples and the sum of creep and shrinkage strain of the loaded samples are close to the upper limit of the calculated values for both the irradiated and the control samples due to the high shrinkage because of the small size of the samples.

The comparison of the calculated and the measured compliance (instantaneous and creep) is shown in Figure 4.9 and it can be seen that compliance of the irradiated and the control samples is within the calculated limits. Compliance of the irradiated samples is slightly higher in comparison with the corresponding control samples.

From the above, we can conclude that the difference in the shrinkage of the

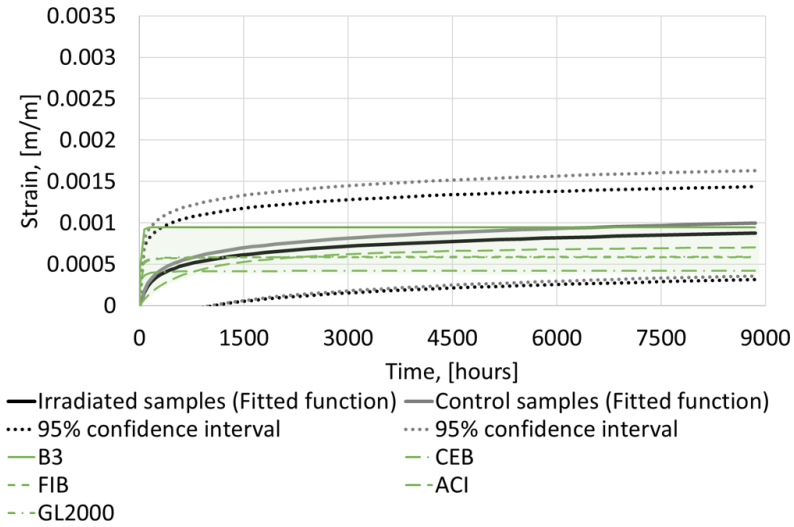

Figure 4.6: Comparison of measured and calculated shrinkage strain of not loaded samples.

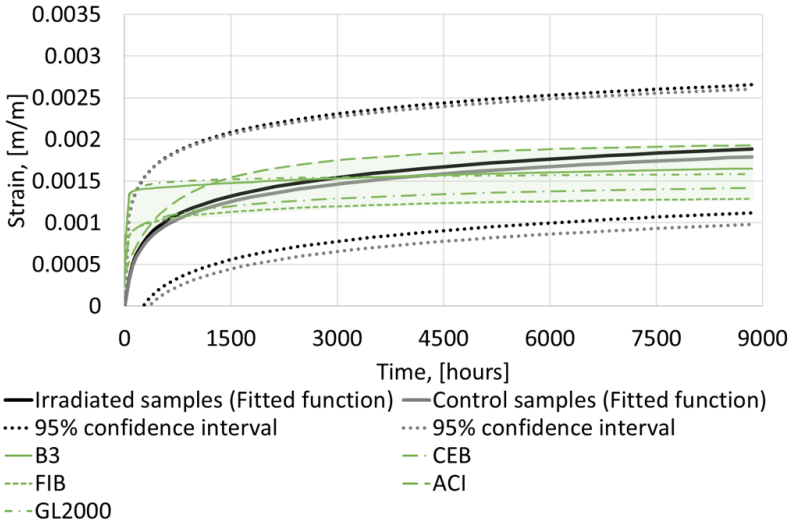

Figure 4.7: Comparison of measured and calculated strain of 1.0 kN loaded samples.

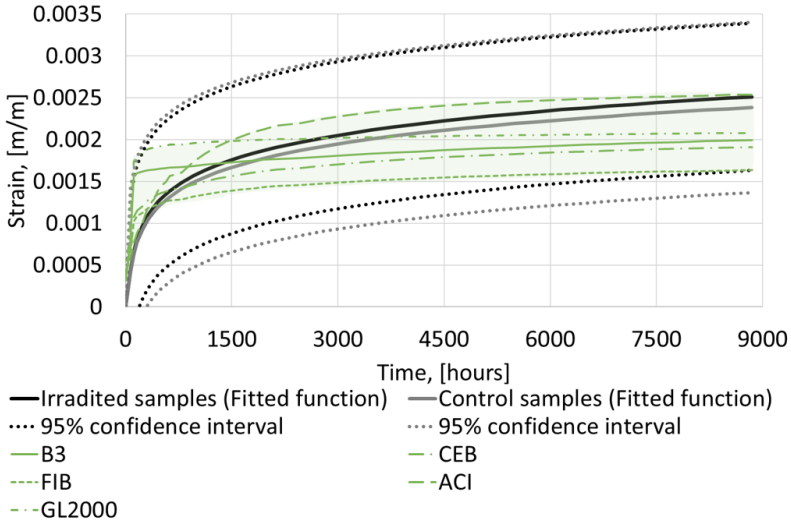

Figure 4.8: Comparison of measured and calculated strain of 1.5 kN loaded samples.

irradiated and the control samples is insignificant, but a slight effect of irradiation on the creep is observed, nevertheless, the creep is still within the interval predicted by the standards for both the irradiated and the control samples. This corresponds with the results regarding the effect of neutron irradiation on concrete creep presented by Denisov et al. (2012) and Dubrovskii et al. (2010).

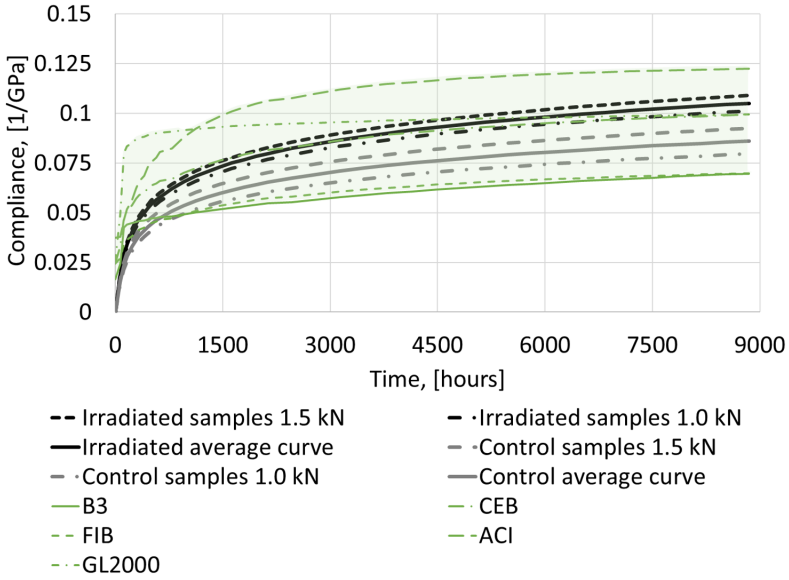

Figure 4.9: Comparison of measured and calculated compliance (instantaneous and creep) of loaded samples.

4.4.2 Nano level

The results of the nanoindentation of C-S-H gel only are shown below since this phase is responsible for the creep.

The indentation creep compliance was calculated according the following formula with the assumption of the instant loading

$$D(t) = \frac{2h^2(t)}{\pi(1-\nu^2)P_0 \tan\alpha}, \tag{4.2}$$

where $D(t)$ is the creep compliance at time t, $h(t)$ is the indentation depth at time t, P_0 is the constant load, ν is the Poisson's ratio of the sample (was considered equal to 0.2) and α is an angle between the surface and the edge of the tip (for the Berkovich diamond tip α is equal to 19.7°) (Minster et al., 2010; Shimizu et al., 1999; Knauss et al., 2008).

Since the sample cannot be loaded instantly, the values of the indentation creep compliance during the first few seconds (approximately 5 seconds after the start of the holding period) should be considered as a rough estimation. Also, the indentation curves with the drift rate higher than 0.05 nm/s were excluded from the results in order to minimize an error of the creep measurement during the holding period.

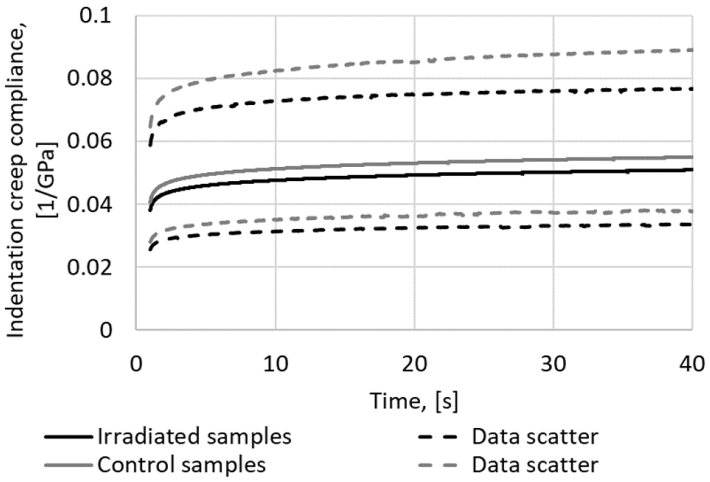

Figure 4.10: Indentation creep compliance.

Since there was no difference in the indentation results of the loaded and the not loaded samples, these results were combined and averaged and the creep compliance mean curves and the data scatter limits for the irradiated (175 tests in total) and the control samples (270 tests in total) are shown if Figure 4.10. It can be seen that there is no essential difference in the indentation creep compliance of the irradiated and the control samples and the data scatters are also very similar.

The indentation elastic modulus was determined from the obtained load–displacement curves using the Oliver and Pharr theory (Oliver and Pharr, 1992) and shown in Figure 4.11. The difference between the obtained elastic modulus of the irradiated and the control samples is minor and lies within the limits of the standard deviation (see Figure 4.11).

4.4.3 XRD

The diffraction patterns of the samples with the depiction of the characteristic peaks are shown in Figure 4.12. The instrumental background and the amorphous halo are subtracted from the diffraction patterns for easier comparison. The changes in the diffraction patterns are minor and no carbonation is observed, therefore, it can be concluded that there is no significant effect of gamma-ray irradiation on the sample mineral composition.

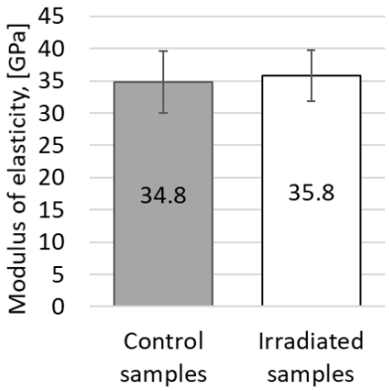

Figure 4.11: C-S-H modulus of elasticity.

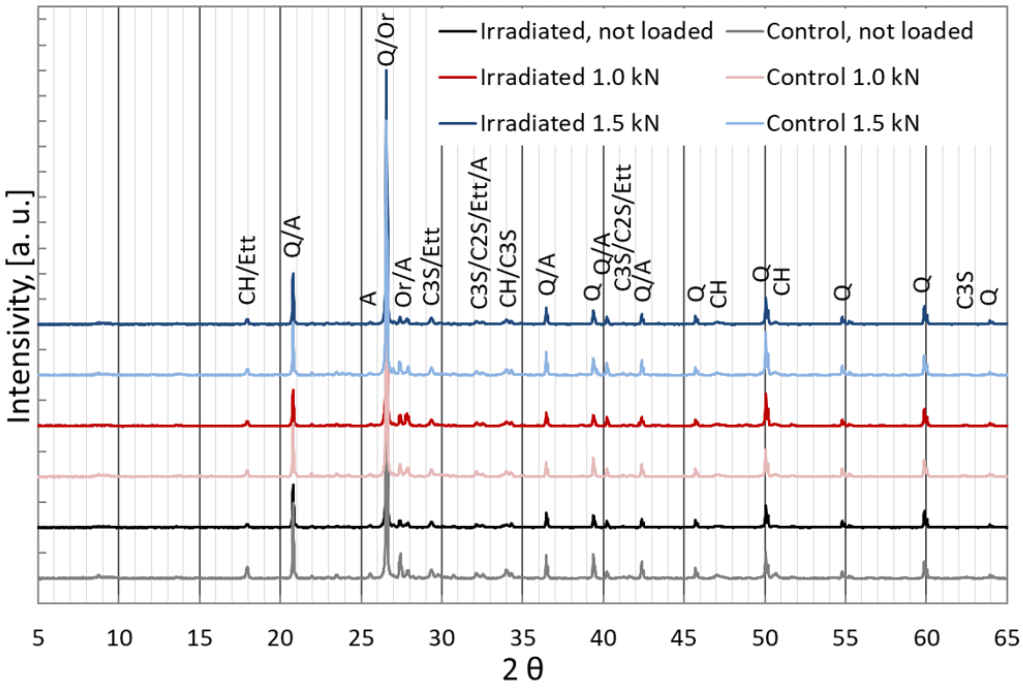

Figure 4.12: Sample and aggregate diffraction patterns. (C3S: alite; C2S: belite CH: portlandite; Ett: Ettringite; Q: quartz; A: albite; Or: Orthoclase).

4.4.4 MIP

The total porosity obtained using the MIP for the not loaded and the loaded control and irradiated samples, where the 1.0 kN loaded and 1.5 kN loaded samples have a similar trend, is shown in Figure 4.13, where it can be seen that the porosity of

the irradiated samples is higher in comparison with the control samples for both the loaded and the not loaded samples. The reason of this can be in the pore vapor pressure buildup due to the radiation-induced water radiolysis which results in gas formation and drying or/and drying due to the gamma heating, but according to the laboratory measurements the temperature of the irradiated samples can be higher by a maximum of 2 °C and can be easily dissipated. These statements have to be confirmed experimentally. The increase in porosity may be a reason of the slight increase of the creep of the irradiated samples since the macroscale deformation is a consequence of porosity (Bažant and Jirásek, 2018).

The histogram of the pore size distribution is shown in Figure 4.14 where it can be

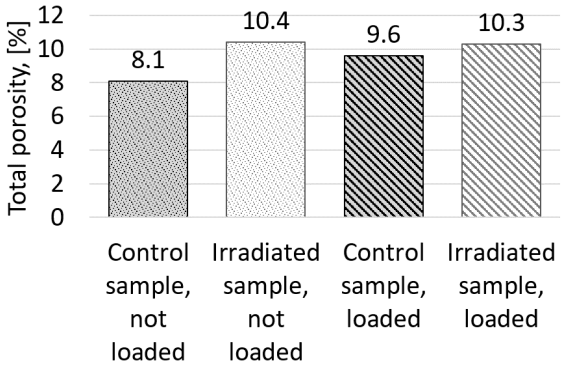

Figure 4.13: Total porosity.

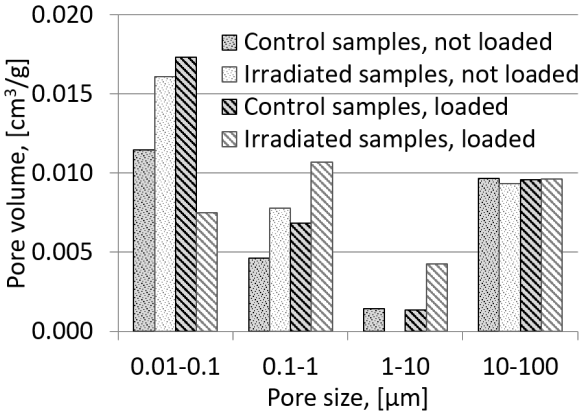

Figure 4.14: Histogram of pore size distribution.

seen that the amount of pores of the irradiated not loaded samples is increased with no significant change in the pore size distribution in comparison with the not loaded control samples, while the peak of the irradiated loaded samples is shifted from 0.01-0.1 µm to 0.1-1 µm in comparison with the loaded control samples. Probably, the sustained load suppresses the development of the new pores and so only the already existing pores increase in size.

4.4.5 Compressive strength test

Since there was no trend in the strength difference of the not loaded and the loaded samples, as the load was too low to cause any damage to the samples, the results were combined and the strength of the irradiated and the control samples with the depiction of the mean strength value is shown in Figure 4.15. It can be seen that the gamma ray cases significant strength reduction (20 % in average) which is consistent with the increase in porosity. The average strength reduction is higher than that presented by Soo and Milian (2001) and Vodák et al. (2005) (15 % and 10 %, respectively).

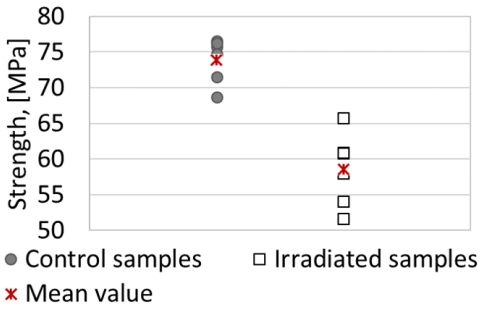

Figure 4.15: Compressive strength.

The relative compressive strength in dependence to the absorbed irradiation dose is shown in Figure 4.16, where the trend is obvious despite the scatter of the data of the samples with different total absorbed dose.

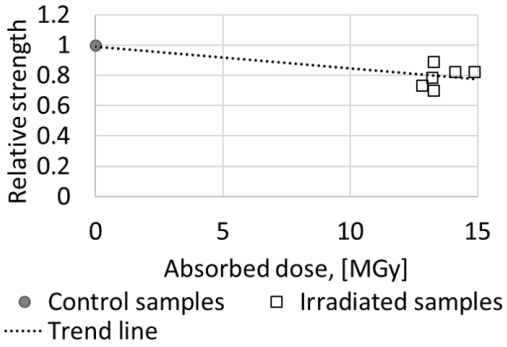

Figure 4.16: Compressive strength in dependence with absorbed irradiation dose.

4.5 Conclusions

From the described experimental investigation of effect of gamma-ray irradiation on cement mortar creep and based on the obtained results, the following conclusions can be drawn:

- No significant effect of gamma-ray irradiation on the cement mortar shrinkage is observed, the shrinkage of the irradiated and the control samples corresponds to the predictions given by the existing models.
- The slight increase in the creep compliance due to the gamma-ray irradiation which is caused by the increase of porosity lies in the interval predicted by the existing prediction models.
- The creep compliance and the indentation elastic modulus of C-S-H gel, which was investigated using nanoindentation technique, is not affected by gamma-ray irradiation.
- No significant effect of gamma-ray irradiation on the cement mortar mineral composition is observed according to XRD analysis.
- The mechanism of the radiation-induced porosity increase is still unclear and requires further investigation.

- The increase in porosity results in significant cement mortar compressive strength reduction (20 % in average).

Chapter 5

Experimental investigation of effect of early-age gamma-ray irradiation on cement mortar

This chapter focuses on the experimental investigation of the effect of gamma-ray irradiation on cement mortar properties when irradiation starts at the early age. Four samples were subjected to different drying and irradiation conditions for 188 and 356 days starting from the age of eight hours. The post irradiation examination includes nanoindentation, SEM, EDX, XRD analysis, MIP and compressive strength testing for samples that were irradiated during 188 days and XRD and three-point bending and compressive strength testing for 356-day irradiated samples. Based on the obtained results, it was concluded that the drying condition effect is much more significant than the gamma-ray irradiation, however after 356 days of irradiation the compressive strength degradation was observed.

5.1 Motivation

In order to build the platform for the alternative design possibilities in the field of radioactive waste disposal, the effect of early-age gamma-ray irradiation on concrete has to be investigated. The limited amount of research in this field is available (Ochbelagh et al., 2010, 2011; Burnham et al., 2016, 2017; Craeye et al., 2015; Mobasher

Table 5.1: Composition of mortar.

Component	Weight
Cement (CEM I 42.5R), [g]	2625
Water, [g]	1000
Siliceous aggregates with fraction of 0-4 mm, [g]	4200

et al., 2015) and it is difficult to find any trend in the effect of gamma-ray irradiation on the early-age cement-based materials, because the effect of gamma-ray irradiation can be dependent on different factors, such as laboratory condition, presence/absence of insulation, sample size and geometry, water-to-cement ratio and mixture composition, type and size of used aggregates, gamma dose rate and total absorbed dose etc. Therefore, based on the reported information, a new experimental program focusing on the investigation of the effect of gamma-ray irradiation on the cement mortar starting from the early age was designed, conducted and is described below in detail.

5.2 Experiment

The mortar which consists of CEM I 42.5R cement paste with the water-cement ratio of 0.38 and siliceous aggregates with the fraction of 0-4 mm was used to produce small-scale 10x10x80 mm samples with the initial weight of about 19 g, similarly as in Chapter 4 but without superplasticizer. The mortar and the cement composition are given in Table 5.1 and Table 4.2, respectively.

The experiment considered two sets of samples in order to assess the effect of drying on the hydration process, therefore, the insulated (sealed) and not insulated (unsealed) samples were prepared. The insulation was provided by a polyethylene foil. An identical set of reference samples was placed in the same laboratory conditions but away from gamma radiation. Thus, the following experimental series (four samples of each type) were investigated: Irradiated Insulated sample (IrIn), Not irradiated Insulated sample (NrIn), Irradiated Not insulated sample (IrNi) and Not irradiated Not insulated sample (NrNi).

^{60}Co Irradiation Facility UGU-420 of The Joint Institute for Power and Nuclear Research - Sosny of the National Academy of Sciences of Belarus, Minsk was used to perform irradiation. The basic characteristics of the facility are given in Chapter 4.

All samples were cured in a sealed condition till the beginning of irradiation. The sample irradiation started at the sample age of eight hours counting from mixing water with cement. The following measurements were conducted during the irradiation period: length, height, width and weight of the samples. Each dimension was measured using high accuracy digital calipers in three different points of a sample and then averaged. The weight of the samples was measured using a high precision laboratory scale with the error of ± 0.02 g. The insulation of sealed samples was removed before measuring and replaced with a new one after measuring. The environmental temperature and the relative humidity were also recorded. The measurements were carried out once a day during the first week of experimental investigation, three times a week during the next three weeks, once a week during the next two months and once in two weeks during the rest of the experimental investigation. The average temperature was 15.9 °C and the average relative humidity was 48.7 %. The temperature of samples during the gamma-ray irradiation is approximately 2 °C higher due to the gamma-heating according to laboratory measurements. The radiation dose rate was equal to 3.72 kGy/h and 4.02 kGy/h for IrIn and InNi samples. The used dose rate is much higher than the maximum expected dose rate that affects the container for radioactive waste disposal (23 Gy/h), however, according to the current research (Maruyama et al., 2017) the effect of dose rate was not observed, and only the total absorbed dose is important. One sample of each series were taken for post-irradiation examination after 188 days of irradiation with the respective corresponding total absorbed radiation dose of 8.3 MGy and 9.3 MGy. The absorbed dose corresponds to the 300 years of radioactive waste storage (9.0 MGy), (Poyet, 2007; Craeye et al., 2015). The experiment was terminated after 356 days of irradiation with the average irradiation period of about 12 hours per day (the standard operation time of the irradiation facility). The total absorbed dose at the end of experiment is equal to 13.78 MGy and 15.41 MGy for IrIn and IrNi samples.

5.3 Post-irradiation examination

After the irradiation, the samples which were irradiated for 188 days were cut into 5 sections (2x 0.5 cm, 2x 1 cm, 1x 5 cm) by a precise cut-off machine Brillant 210 with a diamond blade. The 0.5-cm sample section from the sample end was not used in further analyses. The adjacent 0.5-cm section was used for the nanoindentation and SEM investigation. The 1-cm sample sections were used for XRD analysis and MIP test. The 5-cm section was used for mechanical testing.

The surface of the 0.5-cm sample sections, which were used for nanoindentation and SEM investigation, was polished with silica carbide paper to achieve a smooth surface. The nanoindentation of the polished sample sections was carried out with a Hysitron Tribolab Ti-700 with the Berkovich diamond tip. Six grids of 8 x 8 indents with the spacing of 6 µm were predetermined on the surface of each sample while avoiding aggregates. Thus, the investigated phases were: the low density calcium silicate hydrate (LD C-S-H), the high density calcium silicate hydrate (HD C-S-H), Portlandite (CH) and unreacted clinker. The nanoindentation was performed using the displacement control test with the trapezoidal loading diagram. The sample surface was loaded by the diamond tip linearly during three seconds till the maximum displacement of 300 nm was reached with a following 20 seconds holding period and 3 seconds of unloading. The indentation elastic modulus was determined from the obtained load–displacement curves using the Oliver and Pharr theory (Oliver and Pharr, 1992). The nanoindentation was performed in the laboratory with the average environmental temperature of 24 °C and the average relative humidity of 45 %. After the nanoindentation, the polished sample sections were dried in a vacuum for three hours with a vacuum pump. The microstructure investigation of these sample sections was carried out by a Phenom XL Desktop SEM which focused on elemental analysis using EDX and on visual assessment of mortar microstructure changes.

The 1-cm sample sections, which were used for XRD analysis were prepared according to the procedure which was described in Chapter 4. The Rietveld analysis based on the obtained X-ray diffraction profiles was performed using the MAUD software. The minerals Crystallographic Information was taken from the crystallography open database (COD). The investigated cement phases were: Alite (C3S),

Belite (C2S), C3A-cubic, C3A-orthorhombic, Ferrite (C4AF), Gypsum, Anhydrite, Periclase, Ettringite (Ett), Hemicarboaluminate, Hydroganet (Hg), Monocarbonate calcium aluminate (Mc), Monosulfate calcium aluminate (Ms), Portlandite (CH), Aragonite, Calcite and Vaterite. The aggregate phases were: Albite, Orthoclase, Oligoclase, Chlorite and Quartz. The background was subtracted in the evaluation software. The amorphous phase was not evaluated in this study. The XRD analysis of the aggregates was performed separately in the similar way.

The 1-cm sample sections which were used for porosity evaluation were prepared in the way described in Chapter 4.

The compressive strength tests on the 5-cm sample sections were performed on a standard laboratory compressive test machine. The measured strengths were then compared to each other.

Three-point bending test was performed on the samples irradiated for 356 days. After that, 4-cm sections of each sample were used for compressive strength test and the rest were cut into sections in order to carry out nanoindentation, XRD, SEM and MIP investigation. At the moment only XRD and strength results are available.

5.4 Results

5.4.1 Weight loss and shrinkage

The sample relative weight loss and the shrinkage are shown in Figure 5.1 and Figure 5.2, respectively. The relatively high weight loss of the insulated samples (IrIn and NrIn) is related to the water vapor evaporation due to insulation removal, which was necessary in order to perform the measurements. The irradiated samples (IrIn and IrNi) have higher weight loss in comparison with the corresponding not irradiated samples (NrIn and NrNi). The increase of weight is related to the increase in environmental relative humidity.

The shrinkage of the not irradiated samples shows expected trends (NrIn and NrNi). However, the shrinkage of the irradiated not insulated samples (IrNi) is higher in comparison to the irradiated insulated samples (IrIn) at the beginning of the experiment and becomes lower at the end of irradiation. This can be related to the

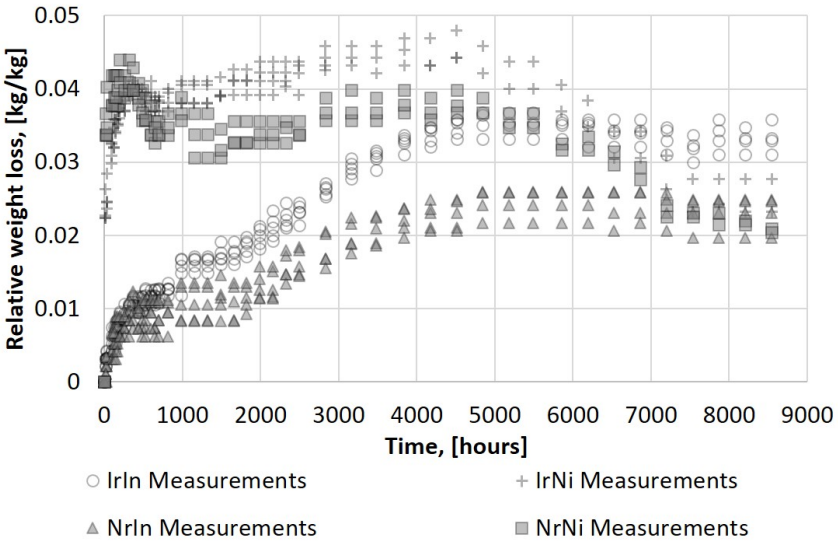

Figure 5.1: Relative weight loss of samples.

possibility of not insulated sample to absorb water from the environment. From the other hand, the data scatter is broad, therefore it is difficult to draw any conclusions.

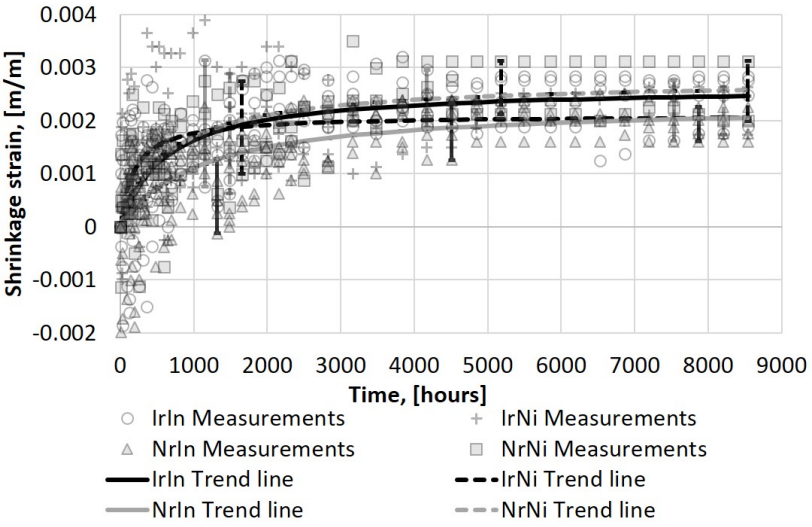

Figure 5.2: Shrinkage strain of samples.

5.4.2 Nanoindentation

The summary of the nanoindentation results is shown in Table 5.2. The individual mechanical phases were assigned using the statistical deconvolution according to the characteristic peaks in the histograms of the elastic modulus and the hardness. Three phases with the elastic modulus lower than 50 GPa and the hardness lower than 1.5 GPa were identified by the statistical deconvolution as: LD C-S-H, HD C-S-H and CH. The values of the elastic modulus higher than 50 GPa and hardness higher than 1.5 GPa correspond to the unreacted clinker and form the fourth phase (Constantinides and Ulm, 2007). The mechanical phases of each indent were also checked against SEM images. Figure 5.3 a) shows a SEM image of cement mortar microstructure, where the aggregates and the location of the grid of indents are depicted, while Figure 5.3 b) shows a higher magnification SEM image of cement paste with the visible indents from nanoindentation with depiction of individual phases. The individual phases assigned according to the statistical deconvolution correspond to the visual SEM image observation. The statistical deconvolution helps to assign a certain mechanical phase to the indents with a not clear individual phase according to the SEM image, see C-S-H affected by clinker in Figure 5.3 b).

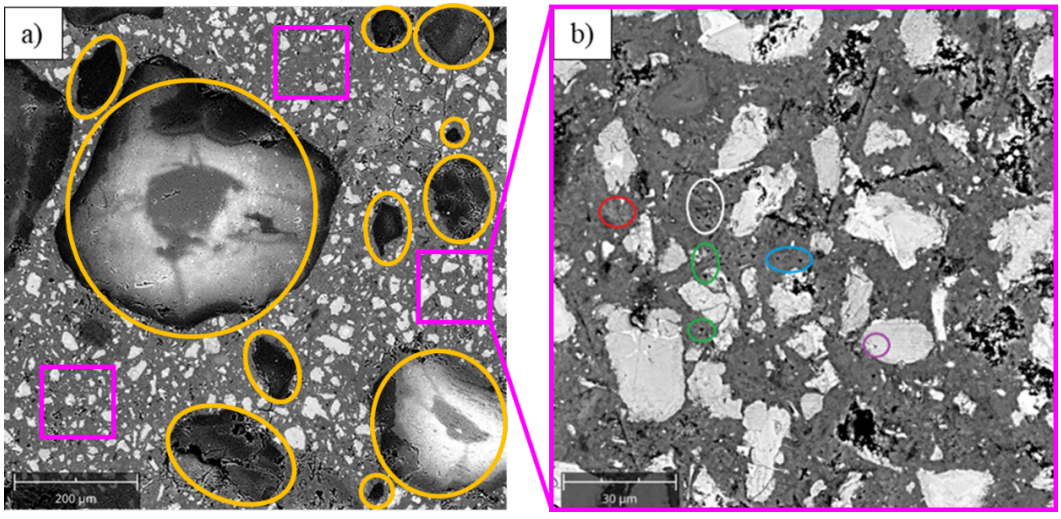

Figure 5.3: SEM-BSE images of: a) cement mortar microstructure with the depicted aggregates (orange) and location of grid of indents (pink), b) cement paste with visible indents with depiction of individual phases: LD C-S-H (white), HD C-S-H (blue), CH (red), clinker (purple), C-S-H affected by clinker (green).

Table 5.2: Summary of indentation results: elastic modulus, hardness and volume fraction of individual phases.

Sample	Parameter	LD C-S-H	HD C-S-H	CH	Small dimension clinker
IrIn	Elastic modulus, E_{NI}, [GPa]	24.6±1.9	30.6±3.2	40.8±3.6	66.2±11.4
	Hardness, H_{NI}, [GPa]	0.65±0.06	0.93±0.18	1.21±0.12	3.84±1.41
	Volume fraction, [%]	1.3	62.6	25.2	10.9
NrIn	Elastic modulus, E_{NI}, [GPa]	20.2±1.6	27.8±2.6	38.1±4.9	65.2±11.3
	Hardness, H_{NI}, [GPa]	0.61±0.22	0.86±0.25	1.21±0.10	3.40±1.06
	Volume fraction, [%]	22.7	51.4	18.2	7.7
IrNi	Elastic modulus, E_{NI}, [GPa]	25.5±2.9	34.7±2.9	44.9±2.6	59.1±9.9
	Hardness, H_{NI}, [GPa]	0.71±0.16	0.88±0.13	1.21±0.14	3.81±1.32
	Volume fraction, [%]	54.0	26.1	8.9	11.0
NrNi	Elastic modulus, E_{NI}, [GPa]	24.1±3.5	33.7±1.9	42.1±3.7	61.0±8.4
	Hardness, H_{NI}, [GPa]	0.70±0.20	0.85±0.10	1.20±0.14	3.95±1.46
	Volume fraction, [%]	56.9	14.0	14.4	14.7

It should be noted that the nanoindentation was displacement-controlled which caused stall of the machine upon reaching its loading capacity when the tip hit clinker of higher dimensions. Therefore, this phase had to be removed from the analysis. The phase removal then caused underestimation of the volume fraction of the anhydrous clinker.

The values of the elasticity modulus of LD C-S-H, HD C-S-H and CH which were obtained from nanoindentation load-displacement curves are in accordance with previous research (Constantinides and Ulm, 2007; Němeček et al., 2013) for all samples. The elastic modulus and hardness show minor variation within each individual phase, see Table 5.2.

The normalized proportion of LD C-S-H and HD C-S-H to the total amount of C-S-H in each sample is shown in Figure 5.4 where can be seen that the volume fraction of HD C-S-H of insulated samples (IrIn and NrIn) is higher in comparison with not insulated samples (IrNi and NrNi) and the volume fraction of HD C-S-H of

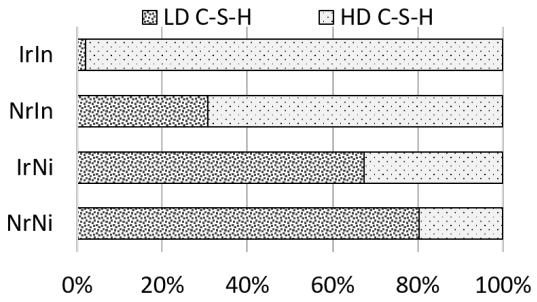

Figure 5.4: Normalized proportion of LD C-S-H and HD C-S-H to total amount of C-S-H.

irradiated samples (IrIn and IrNi) is also higher in comparison with not irradiated (NrIn and NrNi).

The XRD analysis and the SEM image analysis show that the Portlandite volume fraction presented in Table 5.2 is not reliable. More statistical data are needed to obtain convincing results regarding the volume fraction of Portlandite due to its highly non-uniform distribution (Constantinides and Ulm, 2007).

5.4.3 SEM and EDX

The SEM investigation of the samples did not show any significant difference. The Ca/Si ratios of all samples were obtained from EDX analysis at 20 different points of C-S-H and then averaged. The obtained Ca/Si ratios are summarized in Table 5.3. The relations of obtained Ca/Si ratios are consistent with the proportion of LD C-S-H and HD C-S-H volume fractions.

Table 5.3: Ca/Si ratios.

Sample	Min. Ca/Si	Max. Ca/Si	Average Ca/Si
IrIn	1.44	2.18	1.71
NrIn	1.03	2.08	1.49
IrNi	0.96	1.99	1.36
NrNi	0.94	1.99	1.31

5.4.4 XRD

The diffraction patterns of samples irradiated during 188 and 356 days and aggregates with description of the characteristic peaks are shown in Figure 5.5. The instrumental background and the amorphous halo are subtracted from the diffraction patterns for easier comparison. The changes in diffraction patterns are minor and mostly correspond to the presence/absence of insulation, for example, the lower intensity of CH peak in not insulated samples (see peak on 18°) and a higher higher intensity of anhydrous clinker peak (see peak on 29°). No radiation-induced carbonation, which was observed in previous research (Vodák et al., 2011; Maruyama et al., 2018) or any other significant phase transformation was not detected even after 356 days of irradiation.

The results of the Rietveld analysis of the 188-day irradiated samples are summarized in Table 5.4. However, the amorphous phase was not taken into account in the analysis as it was not measured.

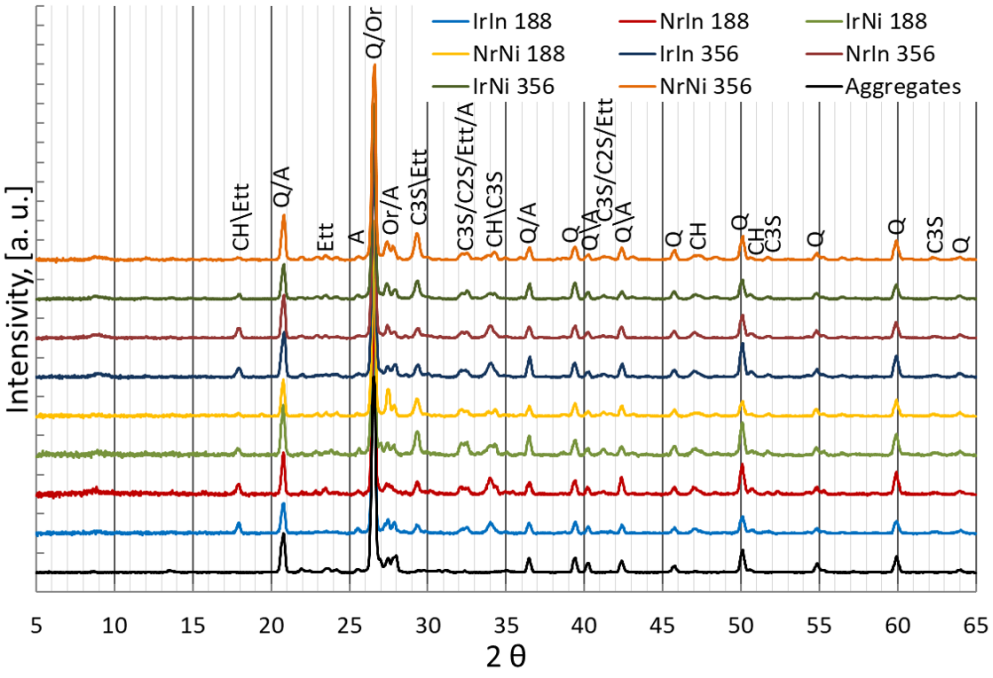

Figure 5.5: Sample and aggregate diffraction patterns. (C3S: Alite; C2S: Belite CH: Portlandite; Ett: Ettringite; Q: Quartz; A: Albite; Or: Orthoclase).

Table 5.4: Phase compositions obtained by XRD/Rietveld analysis of samples.

Phase	IrIn, [%]	NrIn, [%]	IrNi, [%]	NrNni, [%]
C3S	4.1	5.2	7.3	7.9
C2S	1.1	1.1	1.5	1.0
C3A	0.0	0.0	0.0	0.9
C4AF	0.0	1.8	1.3	1.1
Gypsum	0.0	0.0	2.9	1.8
Ett	1.5	3.4	2.2	1.1
CH	4.5	5.7	3.5	1.5
Hg	1.3	0.2	1.2	1.0
Albite	35.4	33.8	30.4	32.7
Orthoclase	12.0	0.6	4.7	11.1
Quartz	40.1	48.2	45.0	39.9

Figure 5.6 shows the proportion of anhydrous clinker and CH in the crystalline part of the cement paste which was obtained from the Rietveld analysis with the first crude assumption of an equal amount of aggregates. The irradiated insulated sample (IrIn) has the lowest amount of anhydrous clinker (the sum of C3S, C2S, C3A and C4AF) and the highest amount of CH, which indicates the highest degree of hydration, while the not irradiated not insulated sample (NrNi) has the highest amount of anhydrous clinker and the lowest amount of CH, this, consequently, denotes the lowest degree of hydration. The obtained relations are consistent with proportion of LD C-S-H and HD C-S-H, see Figure 5.4.

5.4.5 MIP

Figure 5.7 depicts the histogram of the pore size distribution which was obtained using MIP. The average pore sizes of the IrIn, NrIn, IrNi and NrNi samples are 0.070 µm, 0.066 µm, 0.140 µm and 0.110 µm, respectively. The pronounced effect of presence/absence of insulation is observed in the MIP investigation. The presence of the insulation shifts the highest peaks of the porosity distribution to a smaller

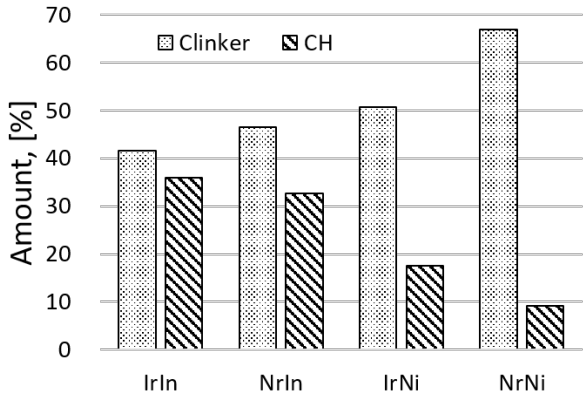

Figure 5.6: Proportion of anhydrous clinker and CH in crystalline part of the cement paste.

size (from 0.1-1 µm to 0.01-0.1 µm), see Figure 5.7, and reduces the average pore diameter significantly. The small amount of pores with the size of 0.001-0.1 µm in the IrIn sample is a reason for the inessential increasing of the average pore size in comparison with the NrIn sample while its total porosity is slightly lower. The IrNi sample has the highest amount of pores smaller than 1 µm, see Figure 5.7, and the highest average pore size in comparison with the other samples which is in accordance with fast weight loss, see Figure 5.1.

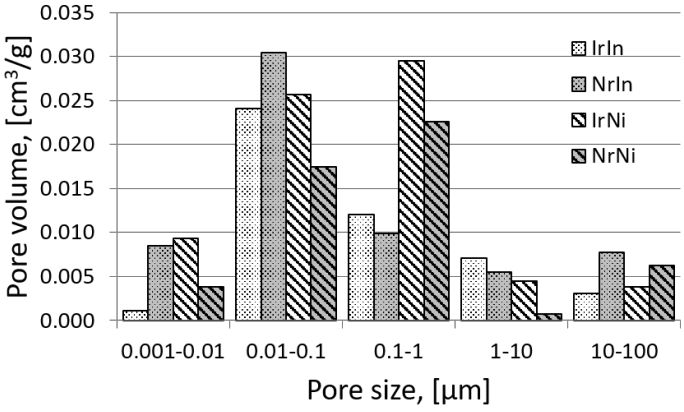

Figure 5.7: Pore size distribution.

5.4.6 Three-point bending and compressive strength

The compressive strength of 188-day irradiated samples is 70.4 MPa, 63.4 MPa, 36.0 MPa and 35.9 MPa for the IrIn, NrIn, IrNi and NrNi samples, respectively. The gamma-ray irradiation has a little effect on the strength of the samples. The strength variation is primarily related to the presence/absence of insulation.

However, some effect of irradiation can be seen on the compressive and the tensile strength of 356-day irradiated samples, see Figure 5.8. The compressive and the tensile strength of the irradiated samples (IrIn and IrNi) are lower than those of the not irradiated samples (NrIn, NrNi) and the irradiation effect on the not insulated samples (IrNi) is more pronounced.

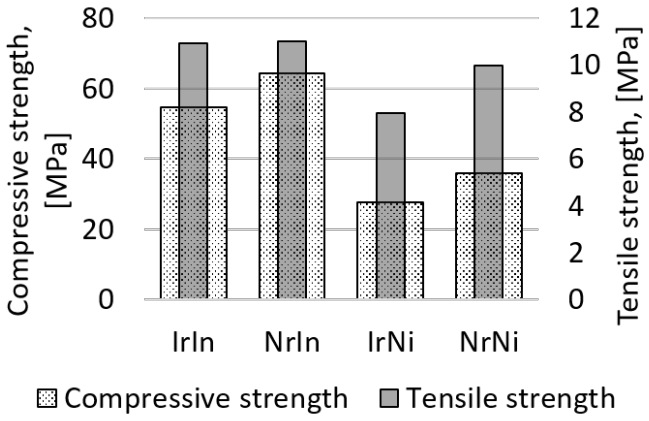

Figure 5.8: Compressive and tensile strength of 356-day irradiated and control samples.

5.5 Discussion

A significant part of the observed changes in the properties of cement mortar is associated with the presence/absence of insulation, however, some trends related to gamma-ray irradiation can also be observed. The main implications of the results regarding the irradiated samples are itemized below in order to provide an appropriate discussion.

The samples irradiated for 188 days have:

- higher weight loss,
- higher volume fraction of HD C-S-H and lower volume fraction of LD C-S-H,
- higher Ca/Si ratio (for not insulated samples the difference is insignificant),
- lower amount of anhydrous clinker and higher amount of CH (consequently higher degree of hydration)

in comparison with the corresponding not irradiated samples. While the samples irradiated for 356 days have:

- lower strength (for not insulated effect is more pronounced).

Moreover, the irradiated insulated sample (IrIn) has higher shrinkage and lower porosity, while irradiated not insulated sample (IrNi) has lower shrinkage and higher porosity in comparison with corresponding not irradiated sample.

The higher weight loss of irradiated samples may be a result of combined effect of water vapor evaporation due to the curing at 2 °C higher temperature and the gas release due to the water radiolysis.

According to Jennings et al. (2007), the difference in elastic modulus of LD C-S-H and HD C-S-H indicates the difference in packing fraction of C-S-H and, consequently, HD C-S-H has not only a higher packing fraction in comparison with LD C-S-H, but also higher density and lower porosity. Also, according to the Jennings et al. (2007), the drying or curing of cement paste at elevated temperatures results in denser C-S-H, but this may lead to higher capillary porosity (the case of irradiated not insulated sample IrNi). Moreover, the C-S-H density increases with the increase of Ca/Si ratio (Suda et al., 2015). Also, according to Muller et al. (2013) the "bulk" density of the C-S-H increases with the increase in the hydration rate.

Therefore, all observed effects related to gamma ray irradiation lead to the C-S-H densification, which corresponds to the current research and coincides with the assumption in Mobasher et al. (2015) and Ochbelagh et al. (2011), however, the mechanism of densification is not clear. The reason of it may be primarily in gamma-heating during the hydration, since higher temperature accelerates the hydration reaction at early age (Escalante-Garcia and Sharp, 1998; Matsushita et al., 2007)

and the "bulk" density of C-S-H increases with the hydration rate. Based on the estimation relying on the surface measured temperate, the estimated maximum of 2 °C difference seems to be too small to ensure such a significant difference in LD C-S-H and HD C-S-H proportion, see Figure 5.4, especially for irradiated insulated sample. For example, according to Jennings et al. (2005) the difference is much smaller even with the temperature difference of 40 °C during the first 28 days of cement hydration. The radiation water decomposition due to radiolysis and consequent gas release, which was observed in Maruyama et al. (2017) and Kontani et al. (2011), may be another reason of C-S-H densification and it results in radiation-induced drying. Also, an enhancement of solution-precipitation process mentioned in Maruyama et al. (2017) may cause C-S-H densification. Most probably, the combined effect of the elevated temperature, radiation-induced drying and the enhancement of solution-precipitation process caused the densification of C-S-H. The above mentioned statements have to be confirmed experimentally.

It has to be noted that porosity of irradiated not insulated sample (IrNi) increases due to the combination of natural drying and radiation-induced drying, while the porosity of irradiated insulated sample (IrIn) slightly decreases. Therefore, the effect of radiation-induced drying by itself (after 188 days of irradiation) is to small to cause porosity reduction.

However, the strength of the irradiated samples after 356 days of irradiation reduces for the insulated and not insulated samples (IrIn and IrNi) in comparison to the not irradiated samples (NrIn and NrNi), this is most probably related to the porosity increase (has to be confirmed by the MIP). Therefore, the effect of radiation-induced drying become significant with increase of irradiation time and dose.

5.6 Conclusions

A complex set of experimental data (weight loss, shrinkage, nanoindentation, SEM, EDX, XRD, MIP and strength) regarding the effect of gamma-ray irradiation starting from the early-age was obtained and described in detail. Based on the obtained results, the following conclusion could be drawn:

- Firstly, the gamma-ray irradiation did not affect the mortar mineral composition significantly. The observed change in the mineral composition could be related primarily to the presence/absence of the insulating film and partially the gamma-heating with the estimated temperature increase of 2 °C.

- Secondly, densification of C-S-H of 188-day irradiated samples could be identified thru the increase of the indentation modulus of elasticity for gamma-ray irradiated samples, both insulated and not insulated, in comparison to the not irradiated samples.

- Thirdly, the densification of C-S-H of the 188-day gamma-ray irradiated not insulated samples was in accordance with the measured increase in porosity, i.e. combined effect of natural and radiation induced drying. However, for the 188-day gamma-irradiated insulated samples, a small decrease in porosity was observed which implies that a certain dose of gamma-ray radiation may have a positive effect on mortar microstructure at early ages.

- Fourthly, gamma-ray irradiation during 356 days affects the strength of insulated and not insulated samples due to the radiation-induced and natural drying.

- Fifthly, it was observed that presence or absence of insulation had a much larger effect than gamma radiation on the measured properties of mortar. This effect was probably also pronounced by exposure of mortar to environmental conditions and to gamma radiation since the age of only 8 hours.

Therefore, regarding the radioactive waste storage applications, it can be recommended to provide high humidity and normal ambient temperature during casting and curing for reduction of the potentially negative effects of gamma radiation, such as the irradiation-induced drying.

Chapter 6

Conclusions

This chapter summarizes the main contributions of the doctoral thesis as well as specific suggestions for the future work in the field of experimental and numerical investigation of the effect of irradiation on concrete.

6.1 Contributions of doctoral thesis

Based on the partial conclusions, which are presented at the and of each chapter, the following contributions of the doctoral thesis can be formulated:

Chapter 2: *General state of the art*

The main contribution of this chapter is a brief and comprehensive review of literature, including the books and papers published only in Russian, i.e. Denisov et al. (2012), Dubrovskii et al. (2010), Altynbaev et al. (2016) and Bykov et al. (1981). All basic mechanisms on different levels (ranging from nuclei interactions to the change in material properties) and the main dependencies are described, therefore, this information can be used for further development of RIVE and radiation-induced damage numerical models.

Chapter 3: *Numerical analysis of VVER-440/213 concrete biological shield*

The main contribution of this chapter is the numerical approach to CBS structural analysis, which combines the newest theoretical and experimental knowledge and measurements. The presented study is the first structural assessment of the effects of irradiation on a typical VVER CBS. The numerical approach

and developed MATLAB code can be used for numerical analyses of various NPP CBSs.

Chapter 4: *Experimental investigation of effect of gamma-ray irradiation on cement mortar creep*

The main contribution of this chapter is that gamma-ray irradiation slightly affects cement mortar creep, therefore, the creep of gamma-irradiated concrete structures as well as the first estimation of creep of neutron-irradiated structures can be predicted by the existing models.

Chapter 5: *Experimental investigation of effect of early-age gamma-ray irradiation on cement mortar*

The main contribution of this chapter is that the curing conditions (presence/absence of insulation) have a more significant effect than the long-term gamma-ray irradiation (up to 356 days and total dose of 15.41 MGy).

6.2 Future work

The following topics for the future work are suggested:

- Development of a comprehensive model of RIVE of aggregates.
- Application of new methods for mesostructure investigation, such as X-Ray Tomography, Neutron Tomography, Neutron Radiography (an example of quantification of the amount of uptaken water using image processing of Neutron Radiography images is shown in section A.3).
- Mesoscale RBSM numerical investigation of the effect of RIVE on concrete with subsequent homogenization for structural analyses (an example of RBSM application is shown in section A.1).
- Additional experimental investigation, such as related to barite and serpentinite RIVE and direct measurements of temperature fields during the entire NPP operation cycle, in order to eliminate the uncertainties related to material properties and environmental condition in Chapter 3.

- Experimental investigation of the effect of gamma-ray irradiation on basic creep.
- Experimental investigation of the effect of short-term gamma-ray irradiation of early-age samples with subsequent modeling using the existing hydration and microstructure models (an example of hydration and microstructure models application is shown in section A.2).

Bibliography

ACI Committee 209 (2008). *Guide for modeling and calculating shrinkage and creep in hardened concrete. Technical report 209.2R-08*. American Concrete Institute, Farmington Hills, Michigan.

Altynbaev, A., Poliakova, P., Iakobson, M., Chernobaeva, A., Erak, D., Zhurko, D., and Zverev, I. (2016). Prolongation of NPP service life. In *III Annual Scientific and Practical Conference "AtomStroyStandard 2016"*. (accessed January 4, 2019)(in Russian). `http://atomsro.ru/wp-content/uploads/file/OPORTAL/AtomStroyStandart_2016/Poliakova_2016_AS.pdf`.

Bažant, Z. and Gettu, R. (1992). Rate effects and load relaxation in static fracture of concrete. *ACI Materials Journal*, 89(5):456–468.

Bažant, Z. and Jirásek, M. (2018). *Creep and Hygrothermal Effects in Concrete Structures (Vol. 225)*. Springer, Netherlands.

Bouniol, P. and Aspart, A. (1998). Disappearance of oxygen in concrete under irradiation: the role of peroxides in radiolysis. *Cement and Concrete Research*, 28(11):1669–1681.

Bouniol, P. and Bjergbakke, E. (2008). A comprehensive model to describe radiolytic processes in cement medium. *Journal of Nuclear Materials*, 372(1):1–15.

Burnham, S., Faure, Q., Tuttle, J., and Jevremovic, T. (2017). Novel approach to improved concrete strength for enhanced safety and durability of the nuclear power

plant operation. In *Proceedings TopSave 2017. Safety in reactor operations*, page A0021. Vienna, Austria.

Burnham, S., Huang, L., and Jevremovic, T. (2016). Examining the effect of gamma radiation exposure in early stage of concrete curing on its strength and long-term durability. In *24th International Conference on Nuclear Engineering*, page V005T15A068. American Society of Mechanical Engineers, Charlotte.

Bykov, V., Denisov, A., Dubrovskii, V., Korenevskii, V., Krivokoneva, G., and Muzalevskii, L. (1981). Effect of irradiation temperature on the radiation expansion of quartz. *Soviet Atomic Energy*, 51(3):593–595.

Comité Euro-International du Béton (1991). *CEB-FIP model code 1990: Design code.* Thomas Telford, London.

Constantinides, G. and Ulm, F. (2007). The nanogranular nature of C-S-H. *Journal of the Mechanics and Physics of Solids*, 55(1):64–90.

Craeye, B., De Schutter, G., Van Humbeeck, H., and Van Cotthemc, A. (2009). Early age behaviour of concrete supercontainers for radioactive waste disposal. *Nuclear Engineering and Design*, 239(1):23–35.

Craeye, B., De Schutter, G., Vuye, C., and Gerardy, I. (2015). Cement-waste interactions: Hardening self-compacting mortar exposed to gamma radiation. *Progress in Nuclear Energy*, 83:212–219.

Craeye, B., De Schutter, G., Wacquier, W., Van Humbeeckc, H., Van Cotthemd, A., and Areias, L. (2011). Closure of the concrete supercontainer in hot cell under thermal load. *Nuclear Engineering and Design*, 241(5):1352–1359.

Denisov, A., Dubrovskii, V., and Solovyov, V. (2012). *Radiation resistance of mineral and polymer construction materials.* ZAO Publishing House “MEI” (In Russian).

Dubrovskii, V., Lavdanskii, P., and Engovatov, I. (2010). *Construction of nuclear power plants.* Publishing Association of Civil Engineering Universities (In Russian).

El-Khameesy, S., Eissa, M., El-Fiki, S., El Shazly, R., Ghali, S., and Saeed, A. (2015). The attenuation capability of selected steel alloys for nuclear reactor applications. *Advances In Physics*, 11(3):3139–3145.

Escalante-Garcia, J. and Sharp, J. (1998). Effect of temperature on the hydration of the main clinker phases in Portland cements: Part I, neat cements. *Cement and Concrete Research*, 28(9):1245–1257.

Esselman, T. and Bruck, P. (2013). *Expected Condition of Concrete at age 80 of Reactor Operation. Technical Report A13276-R-001.* Lucius Pitkins, Inc.

Fédération internationale du béton (2013). *fib model code for concrete structures 2010.* Ernst and Sohn, Berlin.

Field, K., Remec, I., and Le Pape, Y. (2015). Radiation effects on concrete for nuclear powerplants, Part I: Quantification of radiation exposure and radiation effects. *Nuclear Engineering and Design*, 282:126–143.

Gardner, N. and Lockman, M. (2001). Design provisions for drying shrinkage and creep of normal strength. *Materials journal*, 98(2):159–167.

Gedik, Y., Nakamura, H., Yamamoto, Y., and Kunieda, M. (2011). Evaluation of three-dimensional effects in short deep beams using a rigid-body-spring-model. *Cement and Concrete Composites*, 33(9):978–991.

Giorla, A., Le Pape, Y., and Dunant, C. (2017). Computing creep-damage interactions in irradiated concrete. *Journal of Nanomechanics and Micromechanics*, 7(2):04017001.

Gray, B. (1971). The effect of reactor radiation on cement and concrete. In *Proceedings of an Information Exchange Meeting on 'Results of Concrete Irradiation Programmes', volume EUR 4751 f-e.* Commission des Communautés Européennes, Brussels, Belgium.

Hilsdorf, H., Kropp, J., and Koch, H. (1978). The effects of nuclear radiation on the mechanical properties of concrete. *Special Publication, ACI*, 55:223–254.

Jennings, H., Thomas, J., Gevrenov, J., Constantinides, G., and Ulm, F. (2005). Nanostructure of CSH gel in cement paste as a function of curing conditions and relative humidity. In *Creep, shrinkage and durability of concrete and concrete structures, proceedings of Concreep, 7*, pages 19–37.

Jennings, H., Thomas, J., Gevrenov, J., Constantinides, G., and Ulm, F. (2007). A multi-technique investigation of the nanoporosity of cement paste. *Cement and Concrete Research*, 37(3):329–336.

Kang, M., Bilheux, H., Voisin, S., Cheng, C., Perfect, E., Horita, J., and Warren, J. (2013). Water calibration measurements for neutron radiography: Application to water content quantification in porous media. *Nuclear Instruments and Methods in Physics Research Section A: Accelerators, Spectrometers, Detectors and Associated Equipment*, 708:24–31.

Kassab, M., El-Kameesy, S., and Eissa, M. (2015). A study of neutron and gamma-ray interaction properties with cobalt-free highly chromium maraging steel. *Journal of Modern Physics*, 6(11):1526–1532.

Khmurovska, Y. and Štemberk, P. (2018). FEM and RBSM numerical analysis of concrete wall under long-term exposure to neutron irradiation. In *Proceedings of the 12th International PhD Symposium in Civil Engineering*. Prague, Czech Republic.

Kinchin, G. and Pease, R. (1955). The displacement of atoms in solids by radiation. *Reports on Progress in Physics*, 18(1):1–55.

Kis, Z., Sciarretta, F., and Szentmiklósi, L. (2017). Water uptake experiments of historic construction materials from venice by neutron imaging and PGAI methods. *Materials and Structures*, 50(2):159.

Kis, Z., Szentmiklósi, L., and Belgya, T. (2015). NIPS–NORMA station—a combined facility for neutron-based nondestructive element analysis and imaging at the Budapest Neutron Centre. *Nuclear Instruments and Methods in Physics Research Section A: Accelerators, Spectrometers, Detectors and Associated Equipment*, 779:116–123.

Knauss, W., Emri, I., and Lu, H. (2008). Mechanics of polymers: viscoelasticity. In *Handbook of Experimental Solid Mechanics*, pages 49–96. Springer, Berlin.

Kommendant, G., Polivka, M., and Pirtz, D. (1976). *Study of concrete properties for prestressed concrete reactor vessels. Final Report No. UCSESM 76-3*. Department of Civil Engineering, University of California, Berkeley.

Kontani, O., Ichikawa, Y., and Ishizawa, A. (2011). Irradiation effects on concrete durability of nuclear power plants. In *Proceedings of ICAPP 2011*, page 11361. Nice, France.

Kontani, O., Ichikawa, Y., Ishizawa, A., Takizawa, M., and Sato, O. (2010). Irradiation effects on concrete structures. In *Proceedings of International Symposium on the Ageing Management and Maintenance of Nuclear Power Plants*. Mitsubishi Research Institute.

Kontani, O., Sawada, S., Maruyama, I., Takizawa, M., and Sato, O. (2013). Evaluation of irradiation effects on concrete structure: Gamma-ray irradiation tests on cement paste. In *ASME 2013 Power Conference*, page V002T07A002. American Society of Mechanical Engineers.

Košťál, M., Cvachovec, F., Jánský, B., Rypar, V., Juříček, V., Harutyunyan, D., Schulc, M., Milčák, J., Novák, E., and Zaritsky, S. (2016). Neutron deep penetration through reactor pressure vessel and biological concrete shield of VVER-1000 Mock-Up in LR-0 reactor. *Annals of Nuclear Energy*, 94:672–683.

Kubissa, W. and Jaskulski, R. (2013). Measuring and time variability of the sorptivity of concrete. *Procedia Engineering*, 57:634–641.

Lamarsh, J. and Baratta, A. (2001). *Introduction to nuclear engineering (Vol. 3)*. Prentice Hall. Upper Saddle River, NJ, USA.

Le Caër, S. (2011). Water radiolysis: influence of oxide surfaces on H_2 production under ionizing radiation. *Water*, 3(1):235–253.

Le Pape, Y. (2015). Structural effects of radiation-induced volumetric expansion on unreinforced concrete biological shields. *Nuclear Engineering and Design*, 295:534–548.

Le Pape, Y., Alsaid, M., and Giorla, A. (2018). Rock-forming minerals radiation-induced volumetric expansion – revisiting literature data. *Journal of Advanced Concrete Technology*, 16(5):191–209.

Le Pape, Y., Giorla, A., and Sanahuja, J. (2016). Combined effects of temperature and irradiation on concrete damage. *Journal of Advanced Concrete Technology*, 14(3):70–86.

Lee, J., Xi, Y., Willam, K., and Jung, Y. (2009). A multiscale model for modulus of elasticity of concrete at high temperatures. *Cement and Concrete Research*, 39(9):754–762.

Lowinska-Kluge, A. and Piszora, P. (2008). Effect of gamma irradiation on cement composites observed with XRD and SEM methods in the range of radiation dose 0-1409 MGy. *Acta Physica Polonica-Series A*, 114(2):399.

Maekawa, K., Chaube, R., and Kishi, T. (1999). *Modelling of concrete performance: Hydration, microstructure formation, and mass transport*. E & FN Spon, London.

Maekawa, K., Ishida, T., and Kishi, T. (2003). Multi-scale modeling of concrete performance. *Journal of Advanced Concrete Technology*, 1(2):91–126.

Maekawa, K., Ishida, T., and Kishi, T. (2014). *Multi-scale modeling of structural concrete*. Crc Press.

Maruyama, I., Ishikawa, S., Yasukouchi, J., Sawada, S., Kurihara, R., Takizawa, M., and Kontani, O. (2018). Impact of gamma-ray irradiation on hardened white Portland cement pastes exposed to atmosphere. *Cement and Concrete Research*, 108:59–71.

Maruyama, I., Kontani, O., Takizawa, M., Sawada, S., Ishikawa, S., Yasukouchi, J., Sato, O., Etoh, J., and Igari, T. (2017). Development of soundness assessment

procedure for concrete members affected by neutron and gamma-ray irradiation. *Journal of Advanced Concrete Technology*, 15(9):440–523.

Matsushita, T., Hoshino, S., Maruyama, I., Noguchi, T., and Yamada, K. (2007). Effect of curing temperature and water to cement ratio on hydration of cement compounds. In *Proceedings of 12th international congress chemistry of cement*. Montreal.

Mazars, J., Hamon, F., and Grange, S. (2015). A new 3D damage model for concrete under monotonic, cyclic and dynamic loadings. *Materials and Structures*, 48(11):3779–3793.

Mazars, J. and Pijaudier-Cabot, G. (1989). Continuum damage theory—application to concrete. *Journal of Engineering Mechanics*, 115(2):345–365.

Mazzotti, C. and Savoia, M. (2003). Nonlinear creep damage model for concrete under uniaxial compression. *Journal of engineering mechanics*, 129(9):1065–1075.

McDowall, D. (1971). The effect of gamma irradiation on the creep properties of concrete. In *Proceedings of an Information Exchange Meeting on 'Results of Concrete Irradiation Programmes', volume EUR 4751 f-e*. Commission des Communautés Européennes, Brussels, Belgium.

Minster, J., Blahova, O., Lukes, J., and Nemecek, J. (2010). Time-dependent mechanical characteristics measured through the use of a microindentation technique. *Mechanics of Time-Dependent Materials*, 14(3):243–251.

Mobasher, N., Bernal, S., Kinoshita, H., Sharrad, C., and Provis, J. (2015). Gamma irradiation resistance of an early age slag-based cement matrix for nuclear waste encapsulation. *Journal of Materials Research*, 30(9):1563–1571.

Muller, A., Scrivener, K., Gajewicz, A., and McDonald, P. (2013). Densification of C-S-H measured by 1H NMR relaxometry. *Cement and Concrete Research*, 117(1):403–412.

Nechnech, W., Meftah, F., and Reynouard, J. (2002). An elasto-plastic damage model for plain concrete subjected to high temperature. *Engineering structures*, 24(5):587–611.

Nielsen, C., Pearce, C., and Bicanic, N. (2004). Improved phenomenological modelling of transient thermal strains for concrete at high temperatures. *Computers and Concrete*, 1(2):189–209.

Němeček, J., Králík, V., and Vondřejc, J. (2013). Micromechanical analysis of heterogeneous structural materials. *Cement and Concrete Composites*, 36:85–92.

Ochbelagh, R., Azimkhani, S., and Mosavinejad, G. (2011). Effect of gamma and lead as an additive material on the resistance and strength of concrete. *Nuclear Engineering and Design*, 241(6):2359–2363.

Ochbelagh, R., Mosavinejad, G., Molaei, M., and Khodadoost, M. (2010). Effect of low-dose gamma-radiation on concrete during solidification. *International Journal of Physical Sciences*, 5(10):1496–1500.

Oliver, W. and Pharr, M. (1992). An improved technique for determining hardness and elastic modulus using load and displacement sensing indentation experiments. *Journal of Materials Research*, 7(6):1564–1583.

Phan, L. (1996). *Fire performance of high-strength concrete: A report of the state-of-the art, Building and Fire Research Laboratory*. National Institute of Standards and Technology, NISTIR 5934.

Poyet, S. (2007). *Design of the ONDRAF/NIRAS supercontainer concept for vitrified HLW disposal in Belgium: study of the thermo-hydrological behaviour of the concrete buffer*. Rapport CEA, RT DPC/SCCME/07-741-7.

Robinson, B., Moradi, A., Schulin, R., Lehmann, E., and Kaestner, A. (2006). Neutron radiography for the analysis of plant–soil interactions. In *Encyclopedia of Analytical Chemistry: Applications, Theory and Instrumentation*.

Rosseel, T., Maruyama, I., Le Pape, Y., Kontani, O., Giorla, A., Remec, I., Wall, J., Sircar, M., Andrade, C., and Ordonez, M. (2016). Review of the current state of

knowledge on the effects of radiation on concrete. *Journal of Advanced Concrete Technology*, 14(7):368–383.

Rusch, H. (1960). Researches toward a general flexural theory for structural concrete. *Journal of the American Concrete Institute*, 57(1):1–28.

Schneider, M., Froggatt, A., Hazemann, J., Katsuta, T., Ramana, M., Fairlie, I., and Maltini, F. (2016). *The world nuclear industry status report 2016*. A Mycle Schneider Consulting Project.

Schneider, M., Froggatt, A., Hazemann, J., Katsuta, T., Ramana, M., Rodriguez, J., Rüdinger, A., and Stienne, A. (2017). *The world nuclear industry status report 2017*. A Mycle Schneider Consulting Project.

Shimizu, S., Yanagimoto, T., and Sakai, M. (1999). Pyramidal indentation load–depth curve of viscoelastic materials. *Journal of materials research*, 14(10):4075–4086.

Snyder, W. and Neufeld, J. (1957). *Protection Against Neutron Radiation Up to 30 Million Electron Volts. Handbook, 63*. National Bureau of Standards.

Soo, P. and Milian, L. (2001). The effect of gamma radiation on the strength of Portland cement mortars. *Journal of Materials Science Letters*, 20(14):1345–1348.

Suda, Y., Saeki, T., and Saito, T. (2015). Relation between chemical composition and physical properties of C-S-H generated from cementitious materials. *Cement and Concrete Research*, 13(5):275–290.

Szentmiklósi, L., Belgya, T., Révay, Z., and Kis, Z. (2010). Upgrade of the prompt gamma activation analysis and the neutron-induced prompt gamma spectroscopy facilities at the Budapest research reactor. *Journal of Radioanalytical and Nuclear Chemistry*, 286(2):501–505.

Szentmiklósi, L., Kis, Z., Belgya, T., and Berlizov, A. (2013). On the design and installation of a compton–suppressed HPGe spectrometer at the budapest neutron-induced prompt gamma spectroscopy (NIPS) facility. *Journal of Radioanalytical and Nuclear Chemistry*, 298(3):1605–1611.

Toth, S., Legradi, G., and Aszódi, A. (2006). CFD analysis of coolant flow in VVER-440 fuel assemblies with the code ANSYS CFX 10.0. In *Volume 4: Computational Fluid Dynamics, Neutronics Methods and Coupled Codes; Student Paper Competition. 14th International Conference on Nuclear Engineering*. American Society of Mechanical Engineers. Miami, Florida.

US NRC (2016). *Standard Review Plan for Review of Subsequent License Renewal Applications for Nuclear Power Plants. NUREG-2192.* US Nuclear Regulatory Commission.

Vaitová, M., Štemberk, P., Petřík, M., Žďárek, J., and Chválac, O. (2018). Structural aspect of corium spill on VVER-1000 reactor pit floor slab. *Progress in Nuclear Energy*, 107:148–154.

Vodák, F., Trtík, K., Sopko, V., Kapičková, O., and Demo, P. (2005). Effect of γ-irradiation on strength of concrete for nuclear-safety structures. *Cement and Concrete Research*, 35(7):1447–1451.

Vodák, F., Vydra, V., Trtík, K., and Kapičková, O. (2011). Effect of gamma irradiation on properties of hardened cement paste. *Materials and structures*, 44(1):101–107.

William, K., Xi, Y., Lee, K., and Kim, B. (2009). *Thermal response of reinforced concrete structures in nuclear power plants.* A report submitted at College of Engineering and Applied Science.

William, K., Xi, Y., and Naus, D. (2013). *A review of the effects of radiation on microstructure and properties of concretes used in Nuclear Power Plants. Technical Report NUREG/CR-7171, ORNL/TM-2013/263.* U. S. Nuclear Regulatory Commission.

Yamamoto, Y., Nakamura, H., Kuroda, I., and Furuya, N. (2014). Simulation of crack propagation in RC shear wall using a 3D rigid-body-spring model with random geometry. *European Journal of Enviromental and Civil Enginiring*, 18:780–792.

Zhang, P., Wittmann, F., Zhao, T., Lehmann, E., and Vontobel, P. (2011). Neutron radiography, a powerful method to determine time-dependent moisture distributions in concrete. *Nuclear Engineering and Design*, 241(12):4758–4766.

Zubov, V. and Ivanov, A. (1966). Expansion of quartz caused by irradiation with fast neutrons. *Soviet physics, crystallography*, 11:372–374.

Appendix A

Application of MATLAB codes

A.1 RBSM modeling

A.1.1 Nonlinear RBSM analysis

In order to obtain clearer understanding of the effect of the RIVE of aggregates on concrete structure, a modified nonlinear Rigid Body Spring Model (RBSM) analyzes were performed in Matlab, to investigate the possible crack pattern. In presented model, each rigid particle, which was represented by a Voronoi cell, had three translational and three rotational degrees of freedom defined at the nucleus of the Voronoi cell (Figure A.1). The boundary surface of two adjacent Voronoi cells was divided into triangles defined by the center of gravity and two adjacent vertices of that surface as seen in Figure A.1. A set of a normal and two shear springs were defined at the center of gravity of each triangle which enabled the model to account for the effects of bending and torsion moment without the need to use any rotational spring, (Yamamoto et al., 2014).

In the analysis, the modified displacement-controlled Newton-Raphson method is employed for the convergence algorithm. In the convergence process, displacements that cancel the unbalanced force of elements are added to the elements. The displacements are calculated using the stiffness matrix. Convergence of the model is satisfied when the ratio of Σ(Unbalanced force of element in the model)^2 to Σ(Applied force to element)^2 becomes less than 10^{-6}.

The constitutive models for tension, compression and shear that are used in 3D

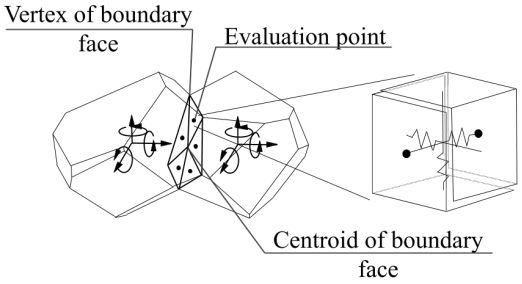

Figure A.1: Modified RBSM, (Yamamoto et al., 2014).

RBSM are shown in Figure A.2. The tensile model for the normal springs is shown in Figure A.2 a). The tensile behavior of concrete is modeled as linear elastic up to tensile strength and a bilinear softening branch according to a 1/4 model is assumed after cracking. In the model, σ_t, g_f and h represent maximum tensile stress, tensile fracture energy, and distance between nuclei, respectively.

Figure A.2 b) shows a stress–strain relation for compression of normal springs that was modeled as an S-shape curve combining two quadratic functions given by Yamamoto et al. (2014) and Gedik et al. (2011). The compression model considers neither softening behavior nor failure of the normal springs. However, compressive failure behavior can be simulated with a confinement effect by means of a combination of a normal spring and a shear spring.

The shear stress–strain relation represents the combination of two tangential springs. The combined shear strain is defined by Yamamoto et al. (2014) and Gedik et al. (2011). Stress–strain relationship for shear is given in Figure A.2 c). In the model, τ_f and γ_f represent shear strength and strain corresponding to the strength, respectively. The stress elastically increases up to the shear strength with the slope of shear modulus (G) and softening behavior is also assumed. It is assumed that the shear softening coefficient K depends upon the stress of the normal spring throw the coefficient β, see Figure A.2 d). The Mohr–Coulomb criterion is assumed as the failure criteria for the shear spring (Figure A.2 e)), where c and φ are cohesion and the angle of internal friction, respectively. Shear strength is assumed to be constant when normal stress is greater than σ_b, which denotes the compression limit value (Figure A.2 e)). Moreover, it is assumed that shear stress decreases with an increase

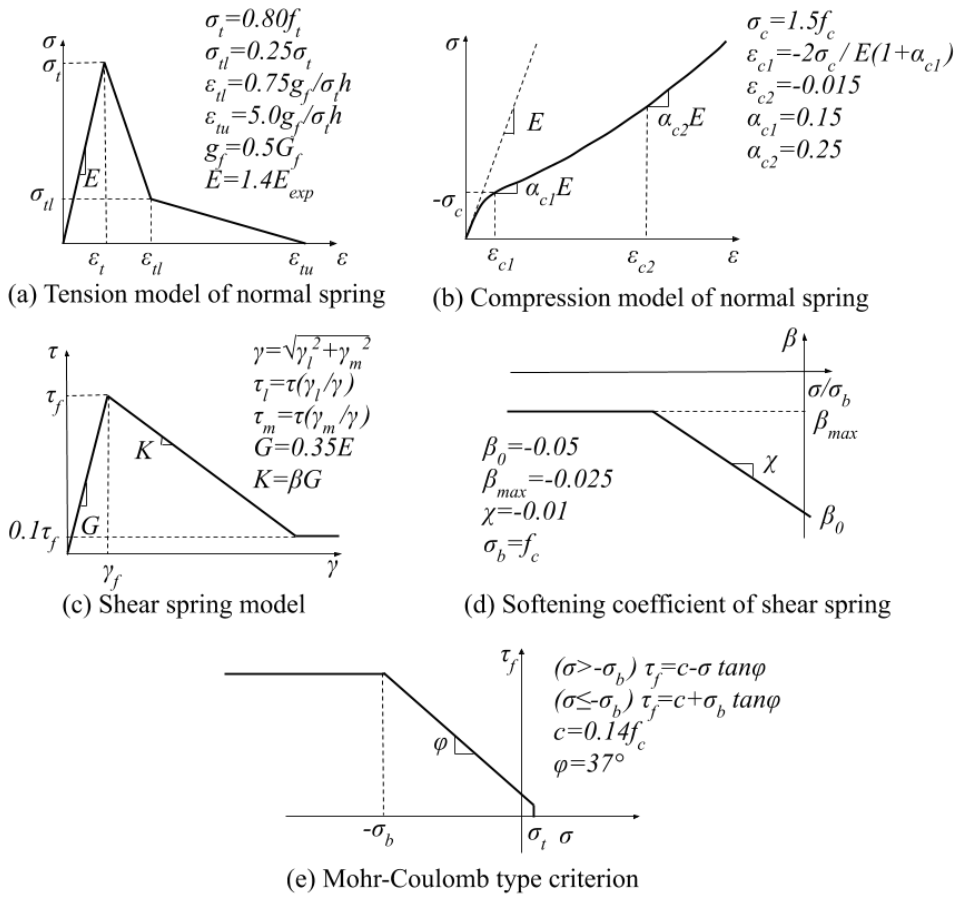

Figure A.2: Constitutive model for concrete, (Yamamoto et al., 2014; Gedik et al., 2011).

in crack width at the cracked surface, in which tensile softening occurs in a normal spring by taken into consideration the shear deterioration coefficient β_{cr} which is described in Yamamoto et al. (2014) and Gedik et al. (2011).

It should be noted that all the given parameters are reliable and validated for models with the average mesh size of 10-30 mm, (Gedik et al., 2011).

A.1.2 Case study

A flat concrete wall with the dimensions of 12 x 12 x 1.8 m was modelled as an extreme case, in order to facilitate visualization of damage caused by the neutron flux. The wall was subjected to neutron irradiation with the distribution of the neutron flux as

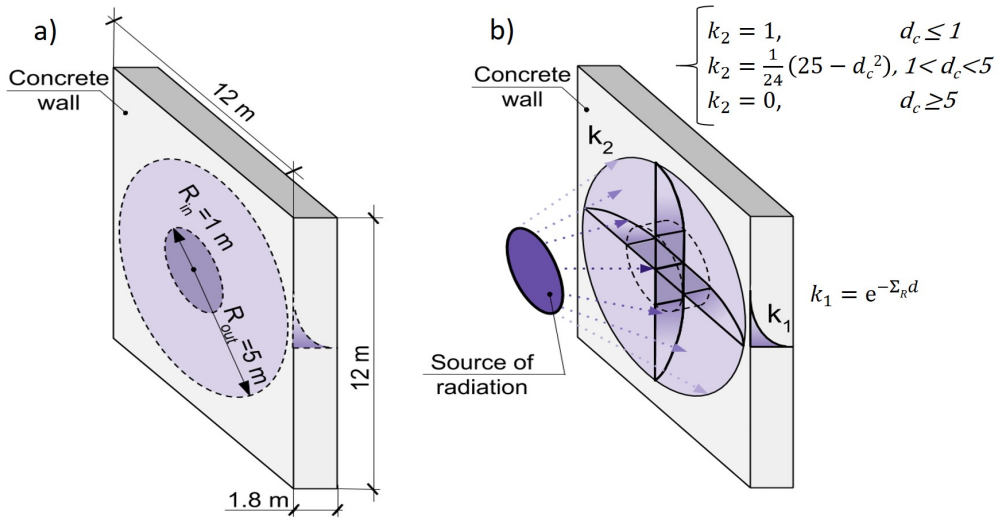

Figure A.3: Concrete wall: a) structure geometry; b) neutron flux distribution.

shown in Figure A.3 and was defined as follows

$$f(d, d_c) = k_1 \cdot k_2 \cdot f_{surf}, \tag{A.1}$$

where $f(d, d_c)$ is the neutron flux at a given depth under the concrete surface and given distance from the center of the wall, f_{surf} is the flux on the surface of the concrete wall defined in Chapter 3, k_1 and k_2 are flux reduction factors due to attenuation and source geometry defined in Figure A.3, d is the depth under the wall surface in cm and d_c is the distance from the center in m.

The reinforced concrete wall was assumed to be made of concrete with the initial compressive strength of 50 MPa, the initial tensile strength of 5 MPa, the initial modulus of elasticity of 35 GPa and Poison's ratio of 0.2. The changes of the concrete properties due to the neutron flux over time were taken into account according to Figure 3.5, Figure 3.6 and Figure 3.7 and Equation 3.2, Equation 3.3 and Equation 3.4. The RIVE is defined by Figure 3.8 and Equation 3.8 with consideration of 60 years of operation. Other loads (self-weigh, temperature etc.) were neglected as well as effect of creep.

Since the RBSM computation time is much higher compared to FEM, the strip of concrete wall is considered in order to reduce the analysis duration. The RBSM analyzed strip is shown in Figure A.4.

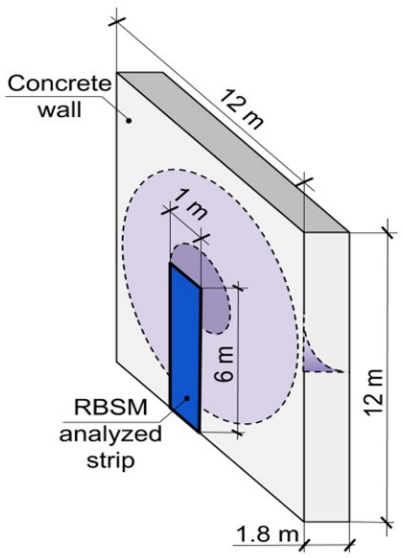

Figure A.4: RBSM analyzed strip.

A.1.3 Results

The results showed that the prolonged exposure of concrete to neutron irradiation affected significantly the structural performance of the concrete wall. The cracks pattern of the concrete wall strip calculated using RBSM is shown in Figure A.5. In this case the concrete wall is completely damaged. The trend of crack propagation can be used in the future estimation of structural elements behavior under the long-term exposure to neutron irradiation.

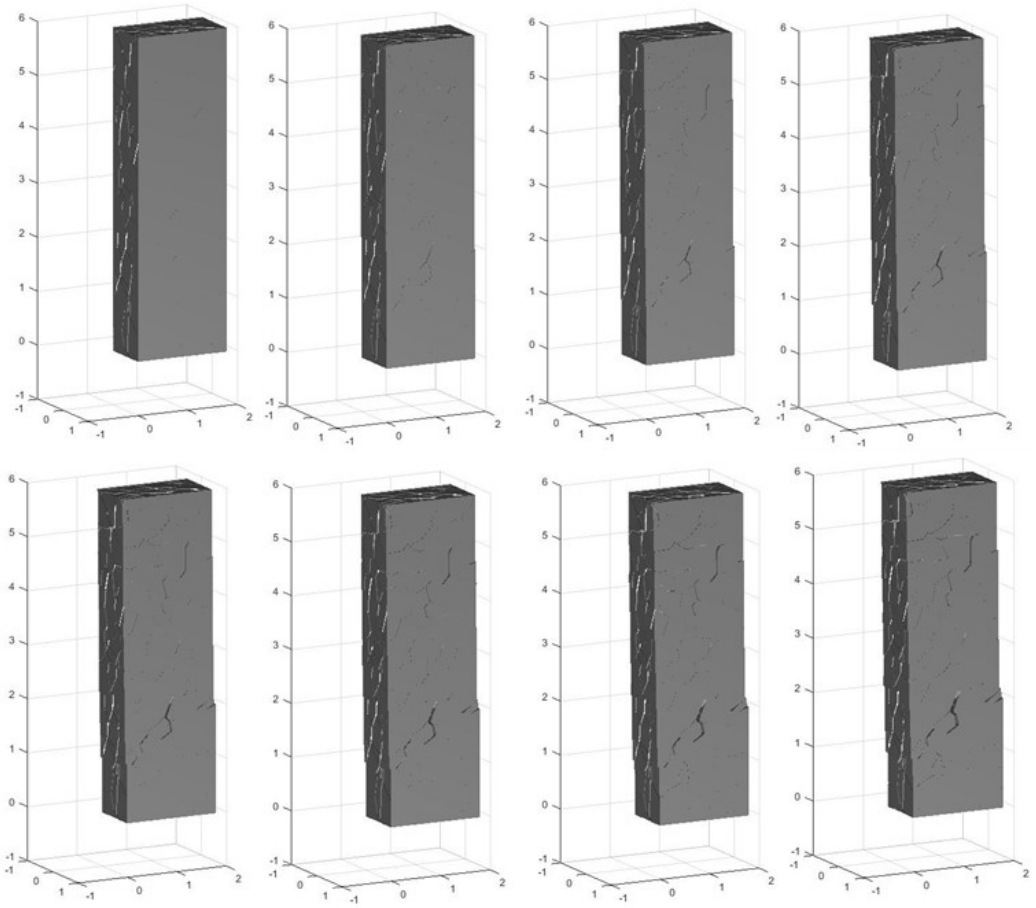

Figure A.5: Cracks propagation.

A.2 Hydration and microstructure model

A.2.1 Experiment

The cement paste which consists of CEM I 42.5R EXTRACEM and water with water-to-cement ratio of 0.38 was used to produce small-scale 10x10x80 mm samples. The cement clinker composition is shown in Table A.1. The samples together with the plexiglass moulds were subjected to gamma-ray irradiation for the maximum of 8 hours and 40 minutes starting at the sample age of one hour and twenty minutes counting from mixing water with cement. It should be noted that a plexiglass is not suitable for experiments with the long-term exposure of gamma-ray irradiation due to the radiation-induced plexiglass degradation. The shape of the moulds can be changed in gamma-irradiation environment, however, the short-term exposure of gamma-rays does not affect plexiglass moulds significantly.

Table A.1: Clinker composition of CEM I 42.5R EXTRACEM according to the manufacturer

C3S, [%]	C2S, [%]	C3A, [%]	C4AF, [%]
63.99	14.30	9.11	8.26

C3S: Alite; C2S: Belite; C3A: Celite; C4AF: Felite.

^{60}Co Irradiation Facility UGU-420 of The Joint Institute for Power and Nuclear Research - Sosny of the National Academy of Sciences of Belarus, Minsk was used to perform irradiation. The basic characteristics of the facility are given in Chapter 4.

Five sets (four samples of each type) were considered in this experimental investigation. Samples Ir-2, Ir-4, Ir-6 and Ir-8 were irradiated for 2 hours and 10 minutes, 4 hours and 20 minutes, 6 hours and 30 minutes and 8 hours and 40 minutes, respectively, not irradiated samples (Ni) were stored in the same laboratory condition but away from gamma-irradiation. Gamma-irradiation dose rate varied from 4.7 kGy/h to 4.9 kGy/h depending on the sample position in the irradiation chamber. The total absorbed dose together with the other mentioned experimental conditions are summarized in Table A.2. Similarly as in the previous experiments the temperature of

Table A.2: Experimental conditions. Irradiation.

Sample	Age at irradiation start, [hours]	Time of irradiation, [hours]	Total absorbed dose, [kGy]	Age at stop of hydration, [hours]	Average Temperature, [°C]	Average relative humidity, [%]
Ni	-	-	-	15.00		
Ir-2	1.33	2.17	10.5	15.00		
Ir-4	1.33	4.33	21.0	15.00	20.7	72.8
Ir-6	1.33	6.50	30.5	15.00		
Ir-8	1.33	8.67	42.4	15.00		

samples during the gamma-ray irradiation is approximately 2 °C higher due to the gamma-heating according to laboratory measurements.

All the samples were immersed in acetone for 24 hours at the sample age of 15 hours in order to stop the hydration process. After that all the samples were dried in oven at 50 °C till equilibrium and were packed in polyethylene foil and were stored in box with silica gel until the post-irradiation examination in order to avoid possible moisture ingress. Environmental temperature and relative humidity were recorded starting from the mixing till packing with the interval of 1 minute. The average environmental temperature and relative humidity (excluding oven drying) are shown in Table A.2.

A.2.2 Numerical simulation

In order to understated whether the hydration reaction was fully stopped after the samples immersion in acetone, the MATLAB code of hydration and microstructure models which are described in Maekawa et al. (1999), Maekawa et al. (2003) and Maekawa et al. (2014) was developed. The data presented in Table A.1 and Table A.2 were used in the analysis and the preliminary results are described below.

The degree of hydration was calculated according the following formula

$$\alpha_{hyd} = \sum p_i \cdot (\overline{Q}_i / \overline{Q}_{i,\infty}), \tag{A.2}$$

where p_i is the mass ratio of the chemical component i of cement (C2S, C3S, C3A, C4AF, gypsum, etc.), $\overline{Q}_i$ is the accumulated heat generation of the chemical component i, $\overline{Q}_{i,\infty}$ is the maximum theoretical specific heat of the component i and α_{hyd} is the averaged degree of hydration.

The calculated degree of hydration of the individual clinker components and their average with the depicted irradiation time and time when the samples were immersed in acetone are shown in Figure A.6.

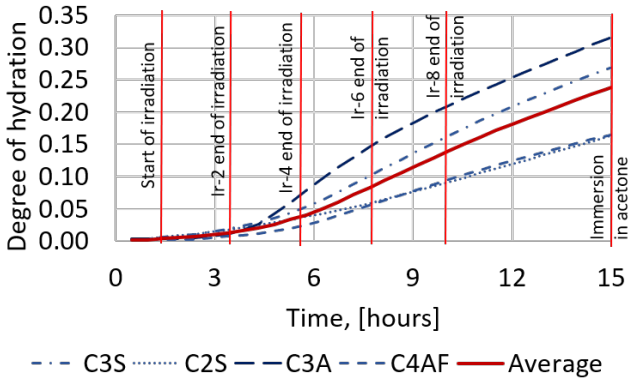

Figure A.6: Calculated degree of hydration.

The volume fraction of anhydrous clinker was calculated as follows

$$V_{cl} = (1 - \alpha_{hyd}) \cdot W_p / \rho_p, \tag{A.3}$$

where W_p is the weight of powder materials per unit paste volume, ρ_p is the density of powder materials and V_{cl} is the volume fraction of anhydrous clinker.

The volume fractions of anhydrous clinker, which were obtained using thee different techniques (nanoindentation, SEM observation and observation made by optical microscope (OPT)) and the average values are shown in Figure A.7 a) while the decrease of the amount of anhydrous clinker due to the hydration reaction over time is shown in Figure A.7 b).

The capillary porosity was calculated using the following equation

$$\phi_c = 1 - V_s - V_{cl}, \tag{A.4}$$

where V_s is the volume of hydrated products.

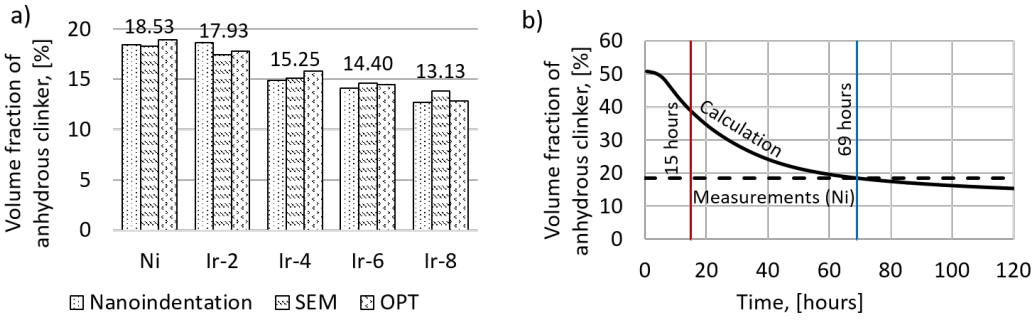

Figure A.7: Amount of anhydrous clinker: a) measured, b) calculated.

The pore size distribution was calculated as follows

$$\phi(r) = \phi_l + \phi_g \cdot V_g + \phi_c \cdot V_c, \tag{A.5}$$

where ϕ_l, ϕ_g and ϕ_c is the interlayer porosity, the gel porosity and the capillary porosity, respectively, $V_i = 1 - \exp(-B_i r)$ is the normalized pore volume, B_i is the porosity distribution parameter and r is the pore radius.

The total porosity obtained using MIP, which is considered as predominantly capillary porosity, is shown in Figure A.8 a) and the calculated capillary porosity over time is shown in Figure A.8 b), while the measured and calculated pore distribution are shown in Figure A.9.

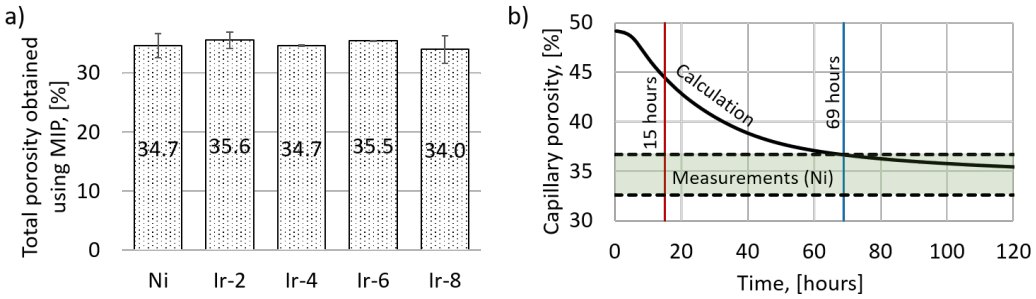

Figure A.8: Capillary porosity: a) measured, b) calculated

As can be seen in Figure A.7, Figure A.8 and Figure A.9, the hydration reaction was not fully stopped at the sample age of 15 hours, but was slowed down significantly

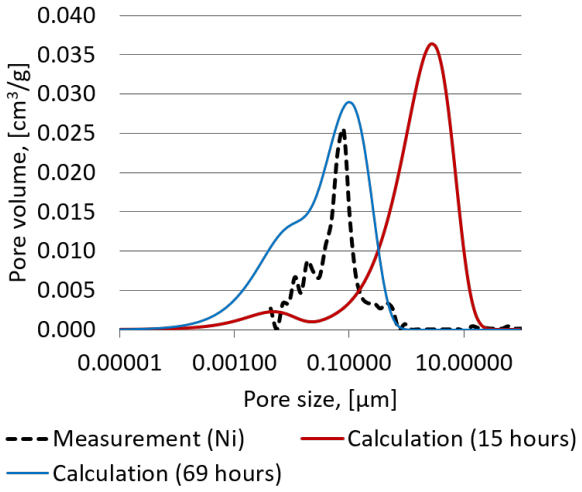

Figure A.9: Pore size distribution.

and the equivalent sample age is approximately equal to 69 hours according to the preliminary results of the numerical simulation.

A.3 Image processing

A.3.1 Neutron radiography

The 2-cm section of a cement sample of each set (samples preparation was explained in section A.2) were used to perform water absorption test accompanied by dynamic neutron radiography imaging.

The dynamic neutron radiography data acquisition was carried out at the NIPS-NORMA station (Kis et al., 2015; Szentmiklósi et al., 2010, 2013) at the Nuclear Analysis and Radiography Department of MTA EK, Hungary. Due to the relatively small neutron beam diameter at the NIPS-NORMA station, only two samples can be investigated simultaneously. In the first test Ni and Ir-8 samples were investigated, after that, in the second test, Ir-4 and Ir-6 samples were investigated and then the Ir-2 sample was investigated separately at the same station under similar conditions.

The upper 15-mm part of the lateral faces of cement samples were wrapped in 0.3 mm thick self-adhesive aluminium tape, while the top and bottom surfaces as well as the lowest 5-mm part of the lateral faces were left without aluminium tape in order to ensure unidirectional water flow and prevent water evaporation from the sample surface. The cement samples were mounted vertically in a designed aluminium container, see Figure A.10, so that the distance from the samples to the screen was equal to 63 mm in order to reduce the blurring effect from the beam divergence and almost completely avoid the forward scattered neutrons impinging in the field of view. The collimation ratio, L/D, which characterizes the divergence of the beam was equal to 233 and the spatial resolution at the sample position was about 340 µm. The first neutron radiography image was done in the dry state. After that the container was filled with MilliQ water with 18.2 MΩ/cm resistance, so that lower 2 mm of the samples were immersed in water. A series of radiographic images with the time step in the range from 8 s to 1 min were taken in order to follow the water front movement and propagation in the cement samples.

Each sample was weighted before and after water uptake test in order to estimate the amount of absorbed water. The amount of absorbed water is characterized by the water content which was defined as the weight of uptaken water per the volume of

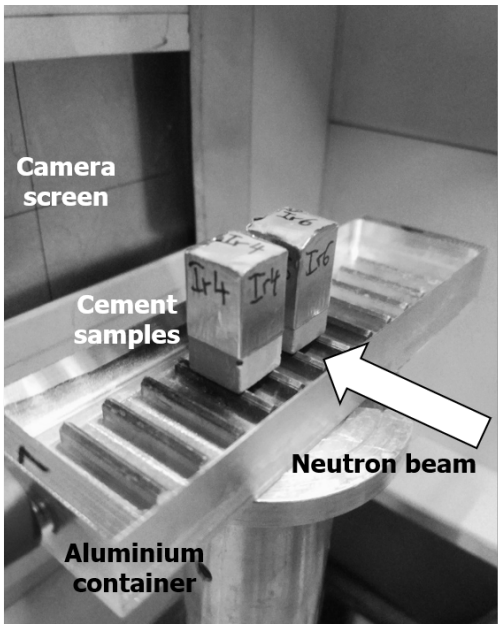

Figure A.10: Neutron radiography experimental setup.

Table A.3: Experimental conditions. Neutron radiography.

Sample	Dry weight, [g]	Imbibition time, [hours]	Wet weight, [g]	Water content, [g/cm^3]	Average Temperature, [°C]	Average relative humidity, [%]
Ni	3.39	12.00	3.97	0.29		
Ir-2	3.36	49.00	3.98	0.31		
Ir-4	3.33	22.67	3.88	0.28	21.0	30.0
Ir-6	3.28	22.67	3.89	0.30		
Ir-8	3.40	12.00	4.01	0.30		

the sample. The weight of the samples together with the imbibition time calculated from the measurements, water content, the average environmental temperature and the average relative humidity in the laboratory during the test are summarized in Table A.3.

The raw neutron radiography images were normalized to the open beam and the

dark current as follows

$$I'(i,j) = NORM \cdot \frac{I_{Raw}(i,j) - I_{DarkCurrent}(i,j)}{I_{OpenBeam}(i,j) - I_{DarkCurrent}(i,j)}, \tag{A.6}$$

where i and j define the spatial pixel position, I_{Raw} is the intensity of raw images, $I_{OpenBeam}$ is the intensity of open beam image, $I_{DarkCurrent}$ is the intensity of dark current image, $NORM$ is a factor to bring the resulting value into the valid range of the image-processing tools (Robinson et al., 2006; Kang et al., 2013) and I' is the intensity of normalized images (transmitted intensity). Representative normalized neutron radiography images are shown in Figure A.11.

A.3.2 Water thickness calibration

According to the Beer–Lambert attenuation law, the neutron beam attenuates depending on the chemical composition of the samples and their geometry and can be approximated for the dry and wet samples as follows

$$I_{dry}(i,j) = I_0(i,j)\exp(-\Sigma_{dry} \cdot d_{dry}(i,j)), \tag{A.7}$$

$$\begin{aligned} I_{wet}(i,j) = I_0(i,j)\exp(-\Sigma_{wet} \cdot d_{wet}(i,j)) = \\ = I_0(i,j)\exp(-\Sigma_{dry} \cdot d_{dry}(i,j) - \Sigma_{water} \cdot d_{water}(i,j)), \end{aligned} \tag{A.8}$$

where I_0 is the intensity of the beam leaving the collimator and penetrating into the sample (incident beam), I_{dry} and I_{wet} are the intensity of the beam transmitted through the dry and wet samples, respectively, calculated from the raw intensity data collected during neutron radiography measurements according to the normalization procedure described in Equation A.6, Σ_{dry}, Σ_{wet} and Σ_{water} are the effective linear attenuation coefficients of dry samples, wet samples and water, respectively, d_{dry}, d_{wet}, d_{water} is the thickness of the dry material in the sample, wet material in the sample and water thickness, respectively (Zhang et al., 2011; Kis et al., 2017).

Dividing Equation A.8 by Equation A.7 results in the following

$$\begin{aligned} \frac{I_{wet}(i,j)}{I_{dry}(i,j)} = \frac{I_0(i,j)\exp(-\Sigma_{dry} \cdot d_{dry}(i,j) - \Sigma_{water} \cdot d_{water}(i,j))}{I_0(i,j)\exp(-\Sigma_{dry} \cdot d_{dry}(i,j))} = \\ = \exp(-\Sigma_{water} \cdot d_{water}(i,j)), \end{aligned} \tag{A.9}$$

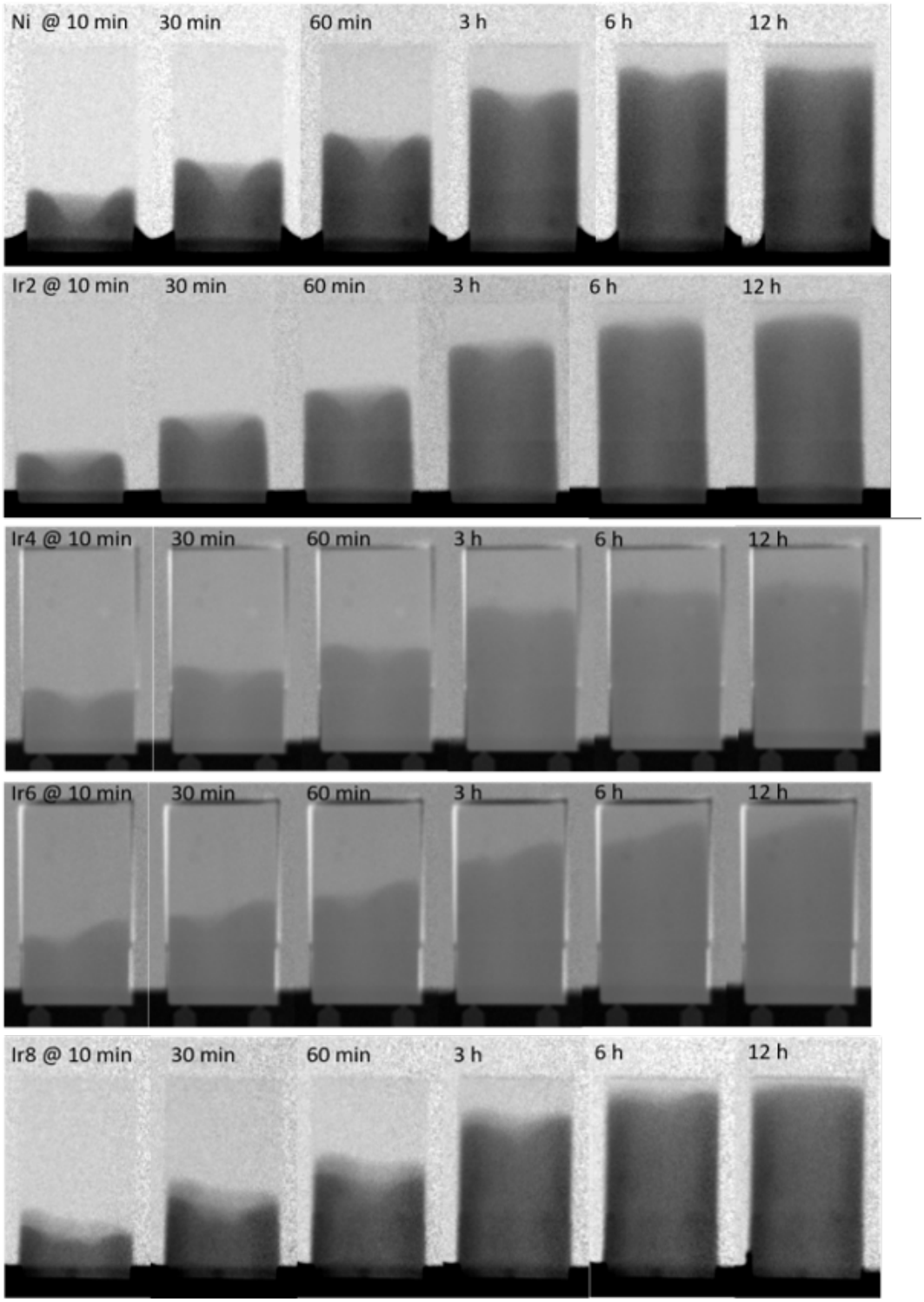

Figure A.11: Normalized neutron transmission images.

$$d_{water}(i,j) = \frac{-\ln(I_{wet}(i,j)/I_{dry}(i,j))}{\Sigma_{water}}, \tag{A.10}$$

$$\rho_{water}(i,j)) = \frac{d_{water}(i,j)}{d_{concrete}}, \tag{A.11}$$

where $d_{concrete}$ is the known thickness of the sample which equals to 1 cm and ρ_{water} is the water content in g per cm^3 of concrete. Therefore, the effective linear attenuation coefficient of water, Σ_{water}, has to be defined in order to quantify the water content in each pixel.

The calibration experiment on a phantom sample was performed within presented experimental investigation which allowed to determine empirically the linear attenuation coefficient of water for the specific neutron radiography facility setup.

A wedge-shaped water calibration phantom sample was designed and fabricated from thin aluminium sheets. The thickness of water in phantom sample varies from 0 cm in the lower part to 0.4 cm in the upper part of phantom sample and represents the possible capillary porosity range (from 0 to 40 %) of a 1-cm thick sample. Three small Gd markers were glued at given positions of the outer plane of the phantom sample. The distance between the tops of the markers is always 1.168 cm. The phantom sample was positioned at the same distance to the scintillator screen as the samples under radiographic imaging to avoid the biasing effect of the different scattering paths. The obtained normalized neutron radiography image is shown in Figure A.12 where the lighter color represents higher water thickness.

The dependence of the logarithmic part of the Equation A.10 ($-\ln(I_{wet}/I_{dry})$) and the water thickness d_{water} is close to linear, see Figure A.13, therefore it was expressed by the fitted linear function as follows

$$d_{water}(i,j) = \frac{-\ln(I_{wet}(i,j)/I_{dry}(i,j))}{\Sigma_{water}} = -0.23836\ln(I_{wet}(i,j)/I_{dry}(i,j)), \tag{A.12}$$

$$\Sigma_{water} = \frac{1}{0.23836} = 4.1953,\ [1/\text{cm}] \tag{A.13}$$

It should be noted that the fitted function is valid only for the particular thermal neutron beam at NIPS-NORMA facility of the Budapest research reactor with the sample-to-screen distance of 63.4 mm.

A.3.3 Water content quantification

In order to quantify the water content in the cement samples, the image processing code was written in MATLAB. Firstly, the noise was removed from the normalized images using the median 5 by 5 pixels filter. The color of the lower part of the sample which was immersed in the water during the experiment was set equal to the threshold value. The threshold was found by enumeration of values with subsequent visual check. Then, the water content of each pixel of the sample at each time step was calculated using the Equation A.10, Equation A.11 and the fitted parameter from Equation A.13. The total water content in the sample at each time step was found by averaging of ρ_{water} for all the pixels that belongs to the sample. The calculated water content evolution over time for all samples is shown in Figure A.14 in the solid lines together with the measured values defined by the square markers of corresponding color. As can be seen in Figure A.14 the calculation systematically underestimates slightly the water content in the samples. It can be related to the relatively high amount of adsorbed and chemically bound water even in the oven-dried cement samples. However, the trends of the calculated water content correlate with the measured water content, therefore, the underestimation of absolute value is considered to be unimportant for this study.

The samples Ni and Ir-8 were chosen for the further numerical investigation and comparison because they represent two limit cases (not irradiated and more than 8

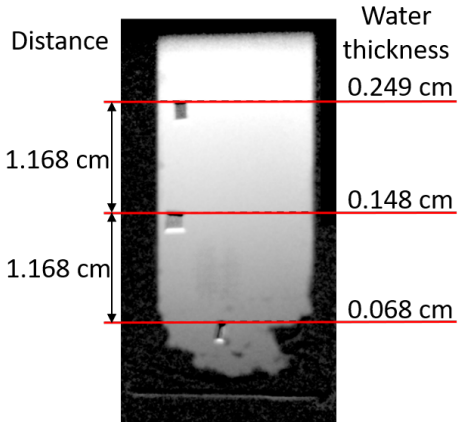

Figure A.12: Normalized neutron attenuation image of phantom sample.

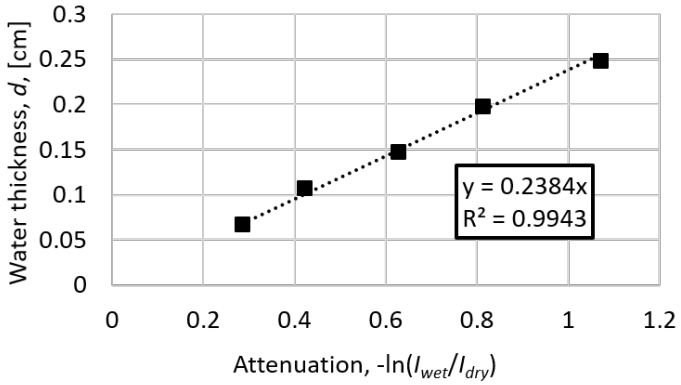

Figure A.13: Fitted calibration function.

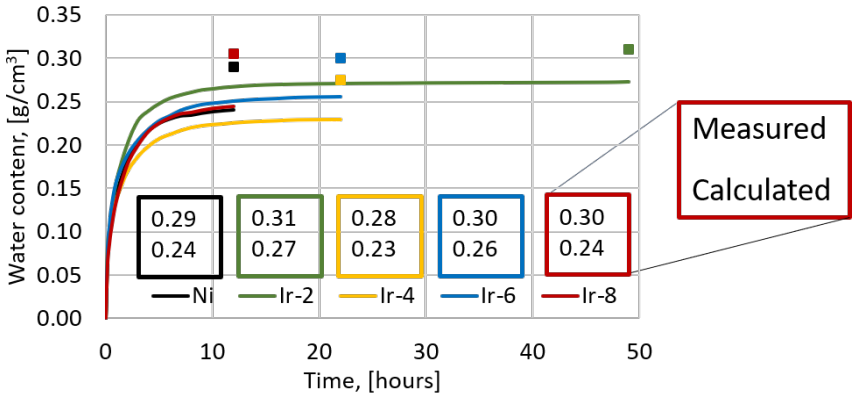

Figure A.14: Calculated and measured content of absorbed water in cement samples.

hours irradiated) of this study and the water absorption test of these samples was performed simultaneously under the identical same experimental conditions, so the gamma-ray irradiation is the only influencing factor.

The water distribution over the sample height was calculated as the average water content of each pixel row of the center part of the sample, the so-called region of interest (ROI), where the water flow is predominantly unidirectional, at different time intervals and is shown in Figure A.15. The water distribution over the sample width was calculated as the average water content of each pixel column of ROI at different time intervals and is shown in Figure A.16. 3D graph of water content change over time and height is shown in Figure A.17 a), while 3D graph of water

content change over time and width is shown in Figure A.17 b).

In Figure A.15 and Figure A.17 a), it can be seen that water ingresses in the Ir-8 sample slightly faster and deeper, however, the maximum water content is somewhat lower, these can be an indirect evidence of lower porosity of the Ir-8 sample and

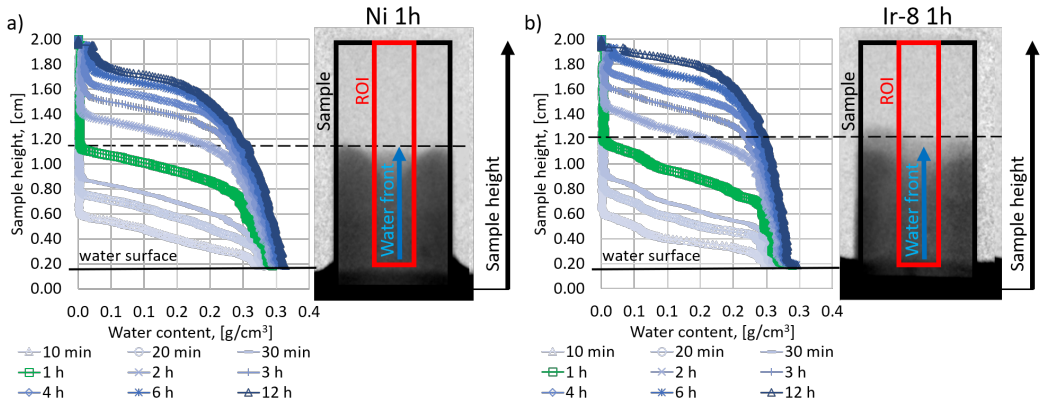

Figure A.15: Water distribution curves over sample height: a) Ni sample, b) Ir-8 sample.

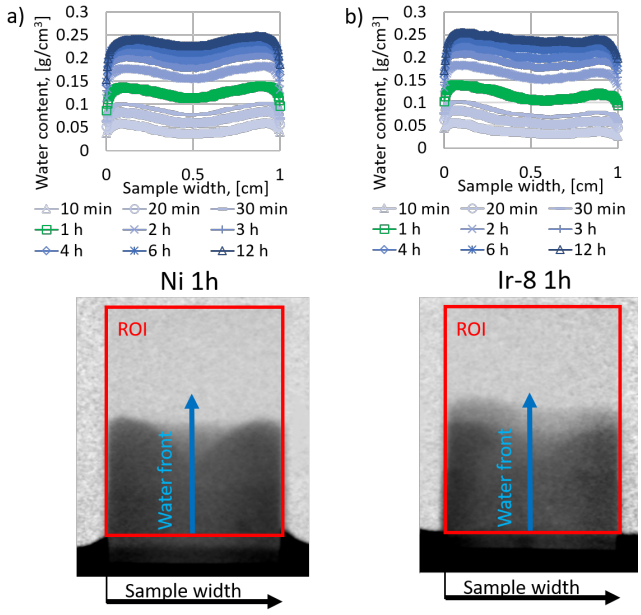

Figure A.16: Water distribution profiles over sample width: a) Ni sample, b) Ir-8 sample.

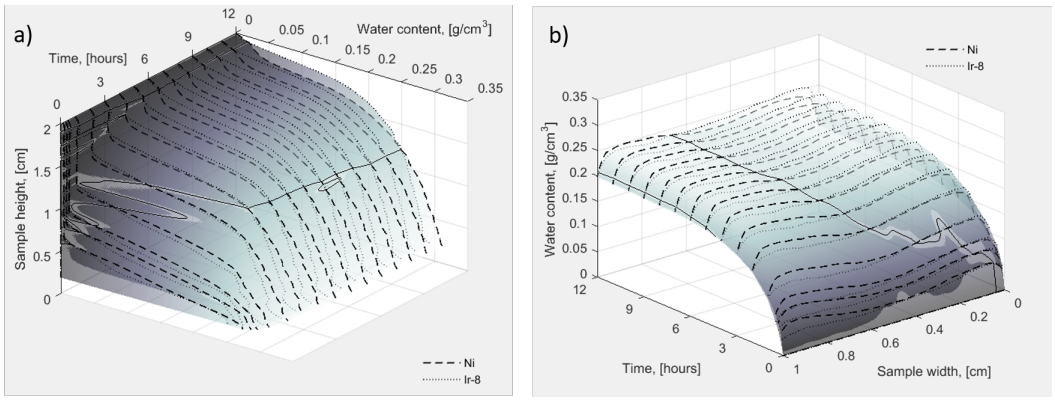

Figure A.17: Water distribution profiles over time: a) and height, b) and width.

consequently of higher pore pressure due to the reduction of pore diameter. It is an interesting observation that the total amount of absorbed water is similar for the Ni sample and the Ir-8 sample (see Figure A.14). The calculated water distribution curves over the width of samples visually correspond to the shape of the water front and no significant difference was found between the Ni sample and the Ir-8 sample, see Figure A.16 and Figure A.17 b).

A.3.4 Cement paste properties determination

The sorptivity coefficient, the penetration coefficient and the water capacity can be derived from the above calculated water distribution.

The sorptivity is defined as the rate of the volume of absorbed water normalized by the area change in the square root of time. The early-stage sorpitivity is determined by

$$\frac{W(t)}{F} = S \cdot t^{0.5} + S_0, \tag{A.14}$$

where W is the volume of absorbed water in time t, F is the sample surface area exposed to water, S is the early-stage sorptivity coefficient and S_0 is an early-stage sorptivity coefficient correction term (Kubissa and Jaskulski, 2013).

The above described dependence was observed during the first four hours of the water absorption test when the water flow was mostly unidirectional. With the longer duration of the test, the water flow is considered to be multi-directional and the

secondary sorptivity coefficient can be find as follows

$$\frac{W(t)}{F} = S_2 \cdot t^{0.5} + C \cdot t + S_0', \tag{A.15}$$

where S_2 is the secondary sorptivity coefficient, C is a parameter which describes the growing effect of multi-directional water flow and S_0' is the same as S_0 in Equation A.14. It should be noted that the effect of S_0' becomes negligible when the longer period of test is taken into consideration, therefore, in this case, S_0' was set to 0 in Equation A.15 (Kubissa and Jaskulski, 2013).

The sorptivity coefficients which were fitted to the experimental data are shown in Figure A.18.

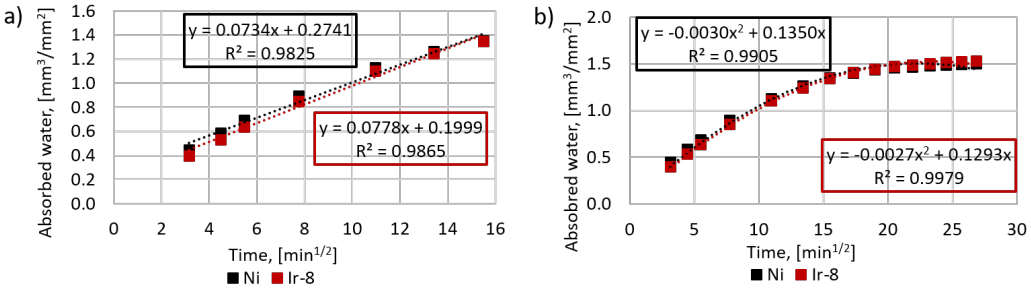

Figure A.18: Sorptivity coefficient determination: a) early-stage sorptivity, b) secondary sorptivity.

The penetration coefficient is very difficult to derive experimentally, however, the neutron radiography technique allows to determine it in a relatively simple way. The penetration coefficient is defined as follows

$$d(t) = B \cdot t^{0.5} + B_0, \tag{A.16}$$

where $d(t)$ is the depth of water penetration in time t, B is the penetration coefficient and B_0 is an early-stage penetration coefficient correction term (Zhang et al., 2011).

Similarly as in the case of sorptivity, the above described relation is satisfied during the first four hours of the water absorption test. The penetration coefficients which were fitted to the experimental data are shown in Figure A.19.

Finally, the water capacity can be calculated as follows

$$\psi = S/B, \tag{A.17}$$

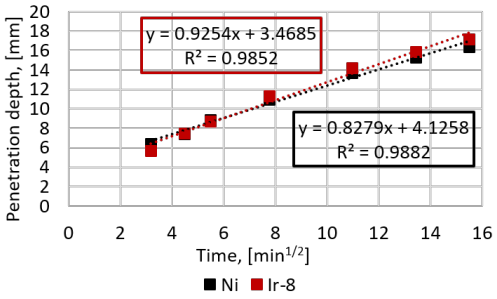

Figure A.19: Penetration coefficient determination.

Table A.4: Fitted parameters.

Sample	S, [mm/min$^{0.5}$]	S_0, [mm]	S_2, [mm/min$^{0.5}$]	S_0', [mm]	C, [mm/min]	B, [mm/min$^{0.5}$]	B_0, [mm]	ψ
Ni	0.073	0.274	0.135	0.000	-0.003	0.828	3.468	0.089
Ir-8	0.078	0.200	0.129	0.000	-0.003	0.925	4.126	0.084

where ψ is the water capacity.

All the fitted parameters for the samples Ni and Ir-8 are summarized in Table A.4. From the quantified parameters it can be seen that the 8 hours 40 minutes of irradiation affect slightly the investigated cement paste properties. The research in this area will be continued.